

PHASE-PURE AND MULTIPHASE CERAMIC WASTE FORMS –  
MICROSTRUCTURE EVOLUTION AND CESIUM IMMOBILIZATION

BY

PRIYATHAM TUMURUGOTI

A THESIS

SUBMITTED TO THE FACULTY OF

ALFRED UNIVERSITY

IN PARTIAL FULFILLMENT OF THE REQUIREMENTS  
FOR THE DEGREE OF

DOCTOR OF PHILOSOPHY

IN

MATERIALS SCIENCE AND ENGINEERING

ALFRED, NEW YORK

FEBRUARY, 2017

PHASE-PURE AND MULTIPHASE CERAMIC WASTE FORMS –  
MICROSTRUCTURE EVOLUTION AND CESIUM IMMOBILIZATION

BY

PRIYATHAM TUMURUGOTI

B.S. INDIAN INSTITUTE OF TECHNOLOGY MADRAS, INDIA (2009)

M.S. MISSOURI UNIVERSITY OF SCIENCE AND TECHNOLOGY,  
ROLLA, MO (2012)

SIGNATURE OF AUTHOR \_\_\_\_\_

APPROVED BY \_\_\_\_\_  
S K SUNDARAM, ADVISOR

\_\_\_\_\_  
SCOTT T. MISTURE, ADVISORY COMMITTEE

\_\_\_\_\_  
DAVID R. LIPKE, ADVISORY COMMITTEE

\_\_\_\_\_  
STEVEN C. TIDROW, ADVISORY COMMITTEE

\_\_\_\_\_  
CHAIR, ORAL THESIS DEFENSE

ACCEPTED BY \_\_\_\_\_  
ALASTAIR N. CORMACK, DEAN  
KAZUO INAMORI SCHOOL OF ENGINEERING

ACCEPTED BY \_\_\_\_\_  
NANCY J. EVANGELISTA, ASSOCIATE PROVOST  
FOR GRADUATE AND PROFESSIONAL PROGRAMS  
ALFRED UNIVERSITY

Alfred University theses are copyright protected and may be used for education or personal research only. Reproduction or distribution in part or whole is prohibited without written permission from the author.

Signature page may be viewed at Scholes Library, New York State College of Ceramics, Alfred University, Alfred, New York.

## ACKNOWLEDGMENTS

My journey for the last four years would have been impossible without the amazing support and encouragement from several individuals. First and foremost, my most sincere thanks to my advisor, Dr. S K Sundaram, for giving me opportunity to work in the field of my interest and NEUP, Department of Energy, US for the financial assistance. Dr. Sundaram's continuous support and assistance in designing and carrying out this work, data collection and analysis has been immense. His help and encouragement in terms of pursuing research opportunities at national labs, participation in international conferences and use of facilities outside Alfred University has been invaluable for my research, professional development and building network for my future endeavors.

I have been very lucky to have Dr. Scott T Misture on my thesis committee. The meetings I had with him on several occasions to discuss my research and his guidance in my understanding and implementation of structural analysis work has been instrumental for this thesis. His insights and reviews for my publications were very helpful. I would also like to acknowledge and thank my other committee members, Dr. David R. Lipke and Dr. Steven C. Tidrow, for their advising and suggestions during the committee meetings. They have always been available for individual meetings if and whenever needed. Their reviewing and support in publishing this thesis is sincerely appreciated.

I would also like to thank Gerry Wynick for his patience and help during my SEM sessions and Swavek Zdzieszynski for data collection during XRD experiments. They have been very supportive and helped me carry out my experiments in very short notices. I would also like to acknowledge all the staff personnel at Alfred University who have helped me directly or indirectly during my program.

During the course of my PhD, I had the unique opportunities to work at national laboratories that contributed significantly to this thesis. Dr. Jake Amoroso at Savannah River National Laboratory (SRNL) has been of great help personally and professionally during my summer research there. The collaborations with SRNL team, Dr. Jake Amoroso and Dr. James Marra, and with Dr. Danny Edwards at Pacific Northwest National Laboratory (PNNL) had a significant contribution to the content of this work. I

would like to acknowledge all these people for their time and support during and even after my visits. I would also like to acknowledge the staff at Cornell Center for Materials Research (CCMR) for training/helping me during FIB and TEM sessions, and staff at Oak-Ridge National Laboratory (ORNL) responsible for neutron diffraction experiments.

I would like to specifically thank my present and past group members Ruhil, Braeden, Dan and Sean for the discussions/inputs, and help during my lab work. I have made many new friends and connections during my stay at Alfred; Diksha, Anvita, Ruhil, Braeden, Sahar, Dimple, Hrishikesh, Keyur, Vignesh and many others. All of them have been very supportive and made my time very memorable. Specifically, I would like to express my gratitude to Dinakar, Neha, Sravan, Vineeth, Vikram, Harish who have always been there for me during my breaks and kept me in good spirits throughout.

Finally, I would like to thank my family for providing a strong foundation and support throughout my life. Reaching this stage wouldn't have been possible without my parents who have been extremely encouraging during every step of my academic career. I would like to thank my brothers who have been enormously supportive and understanding throughout my graduate studies.

# TABLE OF CONTENTS

Acknowledgments .....	iv
Table of Contents .....	vi
List of Tables .....	ix
List of Figures .....	x
Abstract .....	xiv
<b>I. INTRODUCTION .....</b>	<b>1</b>
A. Nuclear Waste Disposal.....	1
A.1. Glass-Based Waste Forms .....	2
A.2. Crystalline waste forms.....	4
A.3. Synroc .....	4
B. Structural and Phase Chemistry of Hollandite .....	8
C. Scope of this Study .....	13
D. Thesis Outline.....	14
<b>II. MATERIALS AND METHODS.....</b>	<b>15</b>
A. Materials .....	15
A.1. Multiphase Compositions .....	15
A.2. Phase-Pure Hollandite Compositions.....	16
B. Sample Preparation.....	16
B.1. Melt-Processing .....	16
B.2. Spark-Plasma Sintering (SPS) .....	16
B.3. Sol-gel Synthesis.....	17
B.4. Solid-state sintering.....	20
<b>III. MICROSTRUCTURAL CHARACTERIZATION OF MULTIPHASE CERAMIC WASTE FORMS .....</b>	<b>21</b>
A. Characterization Methods.....	21
B. Results and Discussions.....	22
B.1. Phase Analysis and Elemental Distribution .....	22
B.2. TEM Observation of Hollandite Lattice .....	26
B.3. Conclusion .....	28
<b>IV. CRYSTALLIZATION BEHAVIOR DURING MELT-PROCESSING OF MULTIPHASE CERAMIC WASTE FORMS.....</b>	<b>29</b>
A. Methodology.....	29

A.1. Viscosity measurements.....	29
A.2. Crystallization experiments.....	30
A.3. Phase analysis .....	31
A.4. In-situ High Temperature XRD studies .....	32
B. Results and Discussions.....	32
B.1. Viscosity measurements.....	32
B.2. DSC measurements and quenching experiments.....	33
B.3. Phase analysis and microstructural characterization.....	35
B.4. High-Temperature X-Ray Diffraction.....	46
C. Conclusion .....	49
<b>V. PHASE EVOLUTION STUDIES OF <math>Ba_{1.0}Cs_{0.3}M_{2.3}Ti_{5.7}O_{16}</math> (<math>M = Al, Cr, Fe</math>) HOLLANDITES.....</b>	<b>50</b>
A. Experimental.....	50
B. Phase Analysis.....	50
C. Visual Examination and Microstructure.....	51
D. Hollandite Phase Evolution .....	52
E. Conclusion .....	55
<b>VI. STRUCTURAL CHARACTERISTICS OF PHASE-PURE <math>Ba_{1.15-x}Cs_{2x}Cr_{2.3}Ti_{5.7}O_{16}</math> HOLLANDITES FOR Cs IMMOBILIZATION.....</b>	<b>56</b>
A. Characterization.....	56
B. Results and Discussion .....	59
B.1. Solubility of Cs .....	59
B.2. Rietveld Analysis .....	61
B.3. Structure of $Ba_{1.15-x}Cs_{2x}Cr_{2.3}Ti_{5.7}O_{16}$ .....	65
C. Conclusion .....	73
<b>VII. PERFORMANCE TESTING OF PHASE-PURE HOLLANDITES.....</b>	<b>74</b>
A. Chemical Durability .....	74
A.1. Experimental .....	74
A.2. Results and Discussions .....	76
B. Irradiation Resistance .....	80
B.1. Experimental .....	81
B.2. Results and Discussions .....	82
<b>VIII. CONCLUSION.....</b>	<b>85</b>
A. Processing of Multiphase Waste Forms .....	85
B. Structural Chemistry of $Ba_{1.15-x}Cs_{2x}Cr_{2.3}Ti_{5.7}O_{16}$ Hollandites .....	86
C. Performance Testing.....	87

<b>IX. FUTURE WORK .....</b>	<b>88</b>
<b>X. REFERENCES .....</b>	<b>89</b>
<b>XI. APPENDIX .....</b>	<b>97</b>
A. Structural Parameters of Phase-pure Hollandites $\text{Ba}_{1.15-x}\text{Cs}_{2x}\text{Cr}_{2.3}\text{Ti}_{5.7}\text{O}_{16}$ .....	97
A.1. Structure file for $\text{Ba}_{1.15}\text{Cr}_{2.3}\text{Ti}_{5.7}\text{O}_{16}$ .....	97
A.2. Structure file for $\text{Ba}_{1.0}\text{Cs}_{0.3}\text{Cr}_{2.3}\text{Ti}_{5.7}\text{O}_{16}$ .....	99
A.3. Structure file for $\text{Ba}_{0.9}\text{Cs}_{0.5}\text{Cr}_{2.3}\text{Ti}_{5.7}\text{O}_{16}$ .....	100

## LIST OF TABLES

	<b>Page</b>
Table II-1. Target Composition of Multiphase Waste Form CAF-MP .....	15
Table II-2. Values of $x$ for Single-Phase Region of $Ba_xM^{3+}_2Ti^{4+}_{8-2x}O_{16}$ .....	16
Table II-3. Precursor Materials Used for Sol-gel Synthesis .....	18
Table IV-1. Temperature Parameters Used for Quenching Experiments .....	35
Table VI-1. Refined Lattice Parameters for the Composition $Ba_{1.15}Cr_{2.3}Ti_{5.7}O_{16}$ .....	63
Table VI-2. Selected Bond Lengths Obtained for the Structure of $Ba_{1.15}Cr_{2.3}Ti_{5.7}O_{16}$ - Different Bond Lengths Listed Below can be Visualized from Figure VI-2..	63
Table VI-3. Comparison of Target vs. Refined Compositions of $Ba_{1.15-x}Cs_{2x}Cr_{2.3}Ti_{5.7}O_{16}$ Hollandites ( $x = 0, 0.15$ and $0.25$ ) when only Ba was used as Tunnel Cation	64
Table VI-4. XRF Measured Compositions of $Ba_{1.15-x}Cs_{2x}Cr_{2.3}Ti_{5.7}O_{16}$ Hollandites ( $x = 0,$ $0.15$ and $0.25$ ) - As Compared, Measured Values are Close to the Target Values .....	64
Table VI-5. Unit Cell Dimensions and Fit Parameters from Rietveld Refinement of $Ba_{1.15-x}Cs_{2x}Cr_{2.3}Ti_{5.7}O_{16}$ - ' $d$ ' is Average of the Diagonals $d_1$ and $d_2$ of the Tunnel Cross-Section and ' $R_{wp}$ ' is the Weighted Rietveld Parameter .....	66
Table VI-6. Occupancies of the $M_1$ and $M_2$ sites Showing the Redistribution of Cr and Ti ions - Occupancies of Ba and Cs ions are Constrained to the Highlighted Values .....	68
Table VI-7. Refined ADPs of Tunnel Cations of $Ba_{1.15-x}Cs_{2x}Cr_{2.3}Ti_{5.7}O_{16}$ Compositions, $\beta_{12}=\beta_{23}=0$ (by I2/m symmetry) .....	70
Table VII-1. Compositions of Hollandite Series $Ba_{1.15-x}Cs_{2x}Cr_{2.3}Ti_{5.7}O_{16}$ Measured by ICP .....	77

## LIST OF FIGURES

	<b>Page</b>
Figure I-1. Unit cells of representative members of major phases of SYNROC family (a) Hollandite – $Ba_2Al_2Ti_6O_{16}$ (b) Perovskite – $CaTiO_3$ (c) Pyrochlore – $Nd_2Ti_2O_7$ and (d) Zirconolite – $CaZrTi_2O_7$ .....	5
Figure I-2. Schematic of a tetragonal (I4/m) hollandite unit cell viewed down the <i>c</i> -axis.	9
Figure I-3. (a) Tetragonal hollandite with atomic displacements due to octahedral twisting, indicated by dotted arrows, transforming to (b) monoclinic symmetry. Oxygen octahedra on opposite tunnel walls are identical in monoclinic symmetry ( $B1O_6$ and $B2O_6$ ). .....	10
Figure I-4. Schematic view of a monoclinic hollandite superstructure, with a tunnel occupancy of 0.625, along [001] direction. Four different super cells, each made of eight unit cells are shown. Ordering of cations and vacancies across in each of the supercells can be observed. Black solid circles indicate occupied sites and open circles indicate vacancies. The inset shows an individual unit cell showing the disorder in tunnel sites ( $x, y, z$ ): $(0, 0, 0) \rightarrow (0, \pm\delta y, 0)$ .....	12
Figure II-1. Schematic of the graphite die setup in SPS. <sup>67</sup> .....	17
Figure II-2. (a) DTA and (b) TGA curves corresponding to different compositions of the series $Ba_{1.15-x}Cs_{2x}Cr_{2.3}Ti_{5.7}O_{16}$ .....	19
Figure III-1. XRD patterns and corresponding BSE images of CAF-MP-SPS and CAF-MP-Melt (H = Hollandite, P = Perovskite Z = Pyrochlore/Zirconolite, and T = $TiO_2$ ). .....	23
Figure III-2. Phase maps obtained from EBSD. ....	24
Figure III-3. WDS maps of selected elements of CAF-MP-Melt.....	25
Figure III-4. WDS maps of selected elements of CAF-MP-SPS.....	26

Figure III-5. (a) FIB-milled CAF-MP-Melt sample used for TEM observation, (b) Hollandite lattice as viewed from [011] zone axis, and (c) the corresponding SAED pattern. ....	27
Figure IV-1. Temperature-time profile used for DSC experiments. ‘ $\alpha$ ’ is the constant heating/cooling rate used. ....	30
Figure IV-2. Heat cycle used for quenching experiments. ....	31
Figure IV-3. Viscosity as a function of temperature for CAF-MP. The accuracy of individual viscosity values is +/- 20% based on historical data for a reference material measured on the same instrument. The lines through the data are linear fits to aid the eye. ....	33
Figure IV-4. DSC curves showing exothermic peaks between 1280°C and 1330°C. The sharp peak on the dotted line (5 K/min) around 1287°C is an external fluctuation. ....	34
Figure IV-5. (a) Quantitative XRD analysis of CAF-MP quenched from 1500°C and held for 4h. Best fit for Rietveld pattern refinement was obtained with hollandite (H), TiO <sub>2</sub> (T) and tazheranite (C) (b) Corresponding back-scattered image. .	37
Figure IV-6. WDS maps of selected elements of CAF-MP at 1500°C annealed for 4 h. Different phases are labelled on the BSE graphic - hollandite (H) and TiO <sub>2</sub> (T). The brightest background phase is Ca-Zr-Ti-O. ....	38
Figure IV-7. (a) Quantitative XRD analysis of CAF-MP quenched from 1325°C held for varying times. Best fit for Rietveld pattern refinement was obtained with hollandite (H), TiO <sub>2</sub> (T), tazheranite (C) and zirconolite (Z) (b) Corresponding back-scattered images. ....	40
Figure IV-8. WDS maps of selected elements of CAF-MP at 1325°C annealed for 24h. Different phases are labelled on the BSE graphic. (Multiple sweeps were performed across the selected area to collect data for the maps. A shift in the scanned area occurred between different sweeps, as observed through a few of the elemental maps. No shift was observed during individual sweeps). ....	41
Figure IV-9. Quantitative phase distribution as a function of annealing time at 1325°C. Ca-Zr-Ti-O represents both tazheranite and zirconolite phases from Rietveld refinement. ....	42
Figure IV-10. (a) Quantitative XRD analysis of CAF-MP quenched from 1285°C held for varying times. Best fit for Rietveld pattern refinement was obtained with	

hollandite (H), TiO <sub>2</sub> (T), tazheranite (C) and zirconolite (Z) (b) Corresponding back-scattered images. ....	43
Figure IV-11. WDS maps of selected elements of CAF-MP at 1285°C annealed for 24 h. Multiple sweeps were run across the selected area to collect data for the maps. (Here also, a shift in the scanned area occurred between different sweeps, as observed through a few of the elemental maps). ....	44
Figure IV-12. Quantitative phase distribution as a function of annealing time at 1285°C. Ca-Zr-Ti-O represents both tazheranite and zirconolite phases from Rietveld refinement. ....	45
Figure IV-13. In-situ XRD patterns collected at different temperatures during heating from 25°C to 1500°C. Different phases in the starting material are B-BaCO <sub>3</sub> , Z-ZrO <sub>2</sub> , T-TiO <sub>2</sub> (anatase), Cs-Cs <sub>2</sub> CO <sub>3</sub> , C-CeO <sub>2</sub> , Cr-Cr <sub>2</sub> O <sub>3</sub> . ....	48
Figure IV-14. In-situ XRD patterns collected during cooling from 1500°C to room temperature (RT).....	48
Figure V-1. XRD patterns of different single-phase hollandites. ....	51
Figure V-2. As-melt samples of Fe-SP and Cr-SP. ....	52
Figure V-3. HTXRD plots for (a) Al-SP (b) Fe-SP and (c) Cr-SP.....	54
Figure V-4. Phase evolution in Cr-SP.....	54
Figure VI-1. Hollandite unit cell with I2/m symmetry with all crystallographic sites labeled. M1 and M2 are the only two distinct crystallographic sites for octahedral cations (Cr and Ti).....	58
Figure VI-2. Illustrations of oxygen environments surrounding each cation site.....	58
Figure VI-3. Powder XRD patterns of Ba <sub>1.15-x</sub> Cs <sub>2x</sub> Cr <sub>2.3</sub> Ti <sub>5.7</sub> O <sub>16</sub> . Red arrows indicate secondary phase(s), BaCrO <sub>4</sub> /Cs <sub>2</sub> CrO <sub>4</sub> and dotted-vertical lines are hollandite reflections.....	60
Figure VI-4. BSE images of the polished surfaces of hollandites (a) $x = 0$ (b) $x = 0.15$ and (c) $x = 0.25$ . ....	61
Figure VI-5. Rietveld refinement of powder XRD pattern for the composition Ba <sub>1.0</sub> Cs <sub>0.3</sub> Cr <sub>2.3</sub> Ti <sub>5.7</sub> O <sub>16</sub> . ....	62

Figure VI-6. Rietveld refinement of NPD data for the composition $\text{Ba}_{1.0}\text{Cs}_{0.3}\text{Cr}_{2.3}\text{Ti}_{5.7}\text{O}_{16}$ . .....	65
Figure VI-7. Unit-cell (black dotted-line) along different crystallographic directions, showing the elongated bonds (black double-arrows) and corresponding (M1/M2) $\text{O}_6$ octahedra. (a) View along tunnel direction ( $b$ -axis) shows M1-O1 and M2-O2 bonds at corner-shared oxygen sites, (b) and (c) shows M1-O1 and M2-O2 bonds respectively that lie normal to the $b$ -axis.....	68
Figure VI-8. Variation of Cr-O and Ti-O bond lengths on the $M_1$ (dotted line) and $M_2$ (solid line) sites. Error bars are smaller than the data markers. ....	69
Figure VI-9. (a) Thermal ellipsoids of different sites in $\text{Ba}_{1.15}\text{Cr}_{2.3}\text{Ti}_{5.7}\text{O}_{16}$ unit cell. (b) View of the same along [001] illustrating the oblong ellipsoids of tunnel sites that represent the large $\beta_{22}$ displacement parameter. ....	70
Figure VI-10. SAED pattern along [101] zone axis for the composition $x = 0$ . ....	72
Figure VI-11. Powder XRD patterns showing the satellite reflections at low $2\theta$ as indicated. ....	72
Figure VII-1. SEM-BSE micrograph of $\text{Ba}_{1.0}\text{Cs}_{0.3}\text{Cr}_{2.3}\text{Ti}_{5.7}\text{O}_{16}$ showing bright phases rich in Cs. Similar Cs-rich areas were found in other Cs-containing compositions. ....	77
Figure VII-2. Leach rates of Cs and Cr from different hollandites $\text{Ba}_{1.15-x}\text{Cs}_{2x}\text{Cr}_{2.3}\text{Ti}_{5.7}\text{O}_{16}$ measured by ICP. The concentrations (mg/L) presented are normalized by the weight percentages of respective elements in the composition. ....	78
Figure VII-3. XRD patterns of hollandite samples after PCT testing. All crystalline peaks observed indicate that the hollandite (H) structure is preserved after 7 days of PCT leach testing without addition of secondary crystalline phases. ....	79
Figure VII-4. GIXRD patterns showing the radiation-induced surface transformations on $\text{Ba}_{1.15-x}\text{Cs}_{2x}\text{Cr}_{2.3}\text{Ti}_{5.7}\text{O}_{16}$ hollandites (a) $x = 0$ (b) $x = 0.15$ and (c) $x = 0.4$ . Different $2\theta$ peaks are labeled on pristine surface plots and the new phases appeared upon radiation are labeled in corresponding patterns: H – hollandite, T – $\text{TiO}_2$ , B – $\text{BaTi}_2\text{O}_5$ and C – $\text{Cs}_2\text{CrO}_4$ . ....	84

## ABSTRACT

Efforts of this thesis are directed towards developing ceramic waste forms as a potential replacement for the conventional glass waste forms for the safe immobilization and disposal of nuclear wastes from the legacy weapons programs as well as commercial power production. The body of this work consists of two equal parts with first focused on multiphase waste form containing hollandite as major phase and the later, on single-phase hollandites for Cs incorporation.

### **Part I: Multiphase waste forms:**

Hollandite-rich multiphase waste form compositions processed by melt-solidification and spark plasma sintering (SPS) were characterized, compared, and validated for nuclear waste incorporation. Phase identification by X-ray diffraction (XRD) and electron back-scattered diffraction (EBSD) confirm hollandite as the major phase present in these samples along with perovskite, pyrochlore and zirconolite. Distribution of select elements observed by wavelength dispersive spectroscopy (WDS) maps indicate that Cs forms a secondary phase during SPS processing, which is considered undesirable. On the other hand Cs partitioned into hollandite phase in melt-processed samples. Further analysis of hollandite structure in melt-processed composition, by selected area electron diffraction (SAED), reveals ordered arrangement of tunnel ions (Ba/Cs) and vacancies, suggesting efficient Cs incorporation into the lattice.

Following the microstructural analysis, the crystallization behavior of the multiphase composition during melt-processing was studied. The phase assemblage and evolution of hollandite, zirconolite, pyrochlore, and perovskite type structures during melt processing were studied using thermal analysis, in-situ XRD, and scanning electron microscopy (SEM). Samples prepared by melting followed by annealing and quenching were analyzed to determine and measure the progression of the phase assemblage. Samples were melted at 1500°C and heat-treated at crystallization temperatures of 1285°C and 1325°C corresponding to exothermic events identified from differential

scanning calorimetry (DSC) measurements. Results indicate that the selected multiphase composition partially melts at 1500°C with hollandite coexisting as crystalline phase. Perovskite and zirconolite phases crystallized from the residual melt at temperatures below 1350°C. Depending on their respective thermal histories, different quenched samples were found to have different phase assemblages including phases such as perovskite, zirconolite and TiO<sub>2</sub>.

## **Part II: Single phase waste forms**

Hollandites with compositions Ba<sub>1.15-x</sub>Cs<sub>2x</sub>Cr<sub>2.3</sub>Ti<sub>5.7</sub>O<sub>16</sub> have been identified as promising lattices to host Cs. Series of compositions with  $0 \leq x \leq 1.15$  were prepared by sol-gel synthesis, characterized, and analyzed for Cs retention properties. Phase-pure hollandites adopting monoclinic symmetry (I2/m) were observed to form in the compositional range  $0 \leq x \leq 0.4$ . Structural models for the compositions:  $x = 0, 0.15,$  and  $0.25,$  were developed from Rietveld analysis of powder XRD and neutron diffraction data. Refined anisotropic displacement parameters ( $\beta_{ij}$ ) for Ba and Cs ions in the hollandite tunnels indicate local disorder of Ba/Cs along the tunnel direction. In addition, weak super lattice reflections have also been observed in XRD patterns. Our data suggests the presence of supercell structures with ordered tunnel cations for the phase-pure hollandites studied.

Finally, the performance of phase-pure hollandites have been evaluated qualitatively by chemical durability testing and ion-irradiation experiments. Elemental analysis of the leachants after 7-day leach tests show that Cs and Cr were extracted from the lattice together. No direct correlation between structural parameters or Cs content was observed. The simulated light-ion (He<sup>2+</sup>) and heavy-ion (Kr<sup>3+</sup>) irradiation experiments reveal that all the hollandite compositions studied undergo amorphization during  $\alpha$ -decay events, and the extent of it increases with the Cs content.

In summary, the present work validates melt-processing as an effective method to prepare multiphase waste forms with the desired phase assemblage. Ba<sub>1.15-x</sub>Cs<sub>2x</sub>Cr<sub>2.3</sub>Ti<sub>5.7</sub>O<sub>16</sub> hollandite has been identified as an effective ceramic host for Cs immobilization and appropriate structural models for hollandites with different Cs levels have been developed. The structural information may be used to study or simulate the lattice-environment interaction.

# INTRODUCTION

## A. Nuclear Waste Disposal

Nuclear energy accounts for about 11% of the world's total electricity production.<sup>1</sup> With the increasing energy demands and the depleting natural energy resources, nuclear power has been emerging as an economic and clean energy source. Unfortunately, presently, the use of energy from nuclear power plants results in radioactive waste that needs to be treated appropriately to contain the radioactivity. Long-term safe disposal of the radioactive waste generated from commercial nuclear power plants and weapon programs is one of the industry's largest present day challenges. Currently in the U.S., a once-through nuclear fuel cycle is in practice where, the fuel is typically used until its energy output becomes economically impractical at which point the used nuclear fuel (UNF) is transferred to an interim cooling and storage facility prior to eventual disposal in a geological repository. Some countries, like France, employ a closed fuel cycle, where reprocessing of UNF is performed prior to disposal by Purex (Plutonium and Uranium Refining by Extraction) process to extract unreacted 'U' and 'Pu' for reuse. Both the UNF and the reprocessed fuel contain significant amounts of radioactive elements and other non-radioactive elements. Based on the composition and the corresponding heat-generating capacity, the nuclear waste can be categorized into low-level waste (LLW), intermediate-level waste (ILW), or high-level waste (HLW). A majority of the nuclear waste radioactivity comes from HLW which is primarily generated from the aqueous reprocessing of UNF. HLW is comprised of a wide range of radioactive elements including minor actinides (e.g., Np, Am, Cm), fission products (<sup>135</sup>Cs, <sup>129</sup>I, <sup>99</sup>Tc) and many other non-radioactive elements. The overall radiochemical content of HLW changes over time because of the decay of short-lived isotopes into long-lived isotopes. In addition, fission products such as <sup>135</sup>Cs and <sup>99</sup>Tc are highly mobile in water or other geological media. Hence, it is important to design and implement safe, efficient and constant upgradation of immobilization technologies to minimize the leachabilities of these waste elements. It is a common practice to separate these minor actinides and long-lived fission products from HLW prior to the immobilization of the remaining wastes.<sup>2</sup> Different methods such as transmutation into short-lived or non-

radioactive elements and immobilization in highly durable matrices are being investigated for the safe disposal of these highly radioactive and mobile elements. It has been suggested that  $^{135}\text{Cs}$  must be immobilized in a stable matrix since transmutation is not effective without separating the isotope from the waste.<sup>3</sup> Minor actinides could be converted to stable isotopes by transmutation, however, immobilization of all elements in HLW in glassy or ceramic matrices is being envisaged.

The ideal requirements<sup>4</sup> for waste forms include high chemical durability, high radiation resistance, long-term thermodynamic stability, mechanical integrity, appropriate thermal conductivity, homogeneous distribution of radionuclides, low-temperature processing to reduce the volatility of elements like Cs, and long-term compatibility with geological environment. However, no single material possesses all the desired characteristics for immobilizing HLW elements. Currently the practice is to vitrify HLW temporarily into glass waste forms, solidify in suitable canisters, and then transfer the canisters to a suitable geological repository for long-term safe disposal.<sup>5</sup> The choice and design of host material(s) in the permanent repository has been a key challenge and studies are in progress to develop predictive models to understand waste form material and repository environment interactions.

### **A.1. Glass-Based Waste Forms**

Glasses have been the most popular choice because of their ability to accommodate a wide range of radionuclides into their structural network. In addition, other advantages include the inherent resistance to chemical attack and high irradiation resistance<sup>6</sup> due to the short range order of the glass structure that minimizes the creation of point defects and volume change during radiation events.<sup>5</sup> Vitrification of radioactive wastes to form glasses is also considered as a simple production method and has been attractive owing to the extensive experience and advancements in industrial glass melting technology.

#### **A.1.1. Borosilicate Glasses**

Borosilicate glasses are the commonly used glasses for HLW immobilization in the U.S. A typical structure consists of waste form elements bonded to different oxygen polyhedra units such as  $(\text{BO}_4)^{5-}$ ,  $(\text{SiO}_4)^{4-}$ ,  $(\text{BO}_3)^{3-}$ . Alkali borosilicate

glasses have been a popular choice since it can be processed at relatively lower temperature (1100 – 1200°C) and the properties of the borosilicate glass system have been widely studied and well understood.<sup>5</sup> It has been a ‘reference waste form’ for HLW because of its glass-formability, ability to accommodate wide range of elements, chemical durability, excellent mechanical strength, and resistance to irradiation. A major drawback of borosilicate glass waste forms is the low solubility of highly radioactive actinide systems e.g., UO<sub>2</sub>, PuO<sub>2</sub>, AmO<sub>2</sub> etc.<sup>7</sup> Other compounds such as molybdates, sulphates, chromates and chalcogenides were also observed to have low solubility in silicate glass systems.<sup>4</sup> Another concern with the glass waste forms is the ability to ensure the homogeneous distribution of radionuclides in its network. Any segregation might result in undesired phase separation leading to increased leachability. In addition, depending on the geologic repository conditions, devitrification under extreme conditions poses a threat to the structural stability of the glass, enhancing the rate of release of hazardous elements into the biosphere.<sup>8</sup>

The response of glass waste forms to irradiation depends on several factors. Structural changes in the glass network depend upon the type of radiation. In HLW, primary sources of radiation are  $\beta$ -decay of the fission products and  $\alpha$ -decay of the actinide elements.<sup>6</sup> Low energy radiation such as  $\beta$ - and  $\gamma$ - rays produce point defects whereas high energy radiation such as  $\alpha$  particles and  $\alpha$ -recoil result in atomic displacements leading to cascade effects.<sup>4,6</sup> Overall, glass waste forms are prone to radiation-induced consequences such as He accumulation, gas bubble formation, swelling, deterioration of mechanical properties, etc.

### **A.1.2. Other Glass-Based Waste Forms**

Phosphate glasses mainly differ from the silicate glasses in terms of bonding characteristics being similar to those of polymer structures.<sup>9</sup> Compared to silicate glasses, phosphate glasses have less thermal stability, low melt viscosities and are prone to attack in aqueous environments.<sup>5</sup> Despite these concerns, phosphate glasses have attracted interest because of their lower forming temperatures and relatively higher solubility of sulphates, chromates, molybdates and actinides. Lead-iron oxide phosphate glasses are observed to have higher chemical durability in the phosphate family and have been considered as a promising candidate for immobilization of Pu from defense HLW.<sup>4</sup>

Other glass-based waste forms of interest include rare-earth glasses,<sup>10</sup> aluminosilicate glasses,<sup>11,12</sup> and sintered glasses<sup>13</sup> etc. Majority of the novel compositions being studied are intended to increase the solubility of actinides in their structures and simultaneously enhance the chemical durability and radiation resistance.

### **A.2. Crystalline waste forms**

The recognition of potential hazards associated with the thermodynamic instability of glass waste forms initiated the research and development of alternative materials for waste form materials. The immobilization of different elements of HLW in crystalline matrices was proposed.<sup>14,15</sup> The basic idea originated from the isomorphic crystal structures of mineral rocks that can incorporate radionuclides and immobilize them for extensive time periods. These rocks that maintain their properties even through extreme geological environments act as natural analogues for designing the ceramic waste forms. Different elements in HLW have different preferential host phases. A large range of phases and numerous combinations are possible for this purpose. Some of the proposed crystalline phases are monazite, apatite, muratite, hollandite, pyrochlore, zircon etc.<sup>16,17</sup> Direct substitution of a radionuclide element on an isovalent site in the crystalline host phase, substitution on to a different valence site followed by charge compensation on neighboring site or accommodation in the open channels within the host structure are some of the ways by which immobilization can occur. Depending on the phase assemblage, higher waste loadings can be achieved. Basic thermodynamic principles governing the formation of crystalline phases, existing knowledge of the crystal chemistry, and understanding the structure of crystals at atomistic levels will help predict the long-term behavior of different phases under various environments.

### **A.3. Synroc**

Multiphase crystalline materials are easier to prepare and their compositions can be tailored for an effective and complete immobilization of HLW elements. Synroc, short notation for Synthetic Rock, was developed by Ringwood in 1978.<sup>18,19</sup> Different chemical formulations of Synroc materials have been developed over the years based on the composition of HLW for effective immobilization of the corresponding radionuclides. Synroc-C, a multiphase mixture of different titanates, has been designed to incorporate

radioactive waste from commercial nuclear power plants. Major phases in Synroc-C include hollandite, perovskite, zirconolite and pyrochlore. Hollandite acts as the main host for Cs. Zirconolite and pyrochlore are the main hosts for actinides. Perovskite incorporates Sr and rare-earth elements. Figure I-1 shows representative unit cells for the major SYNROC phases.

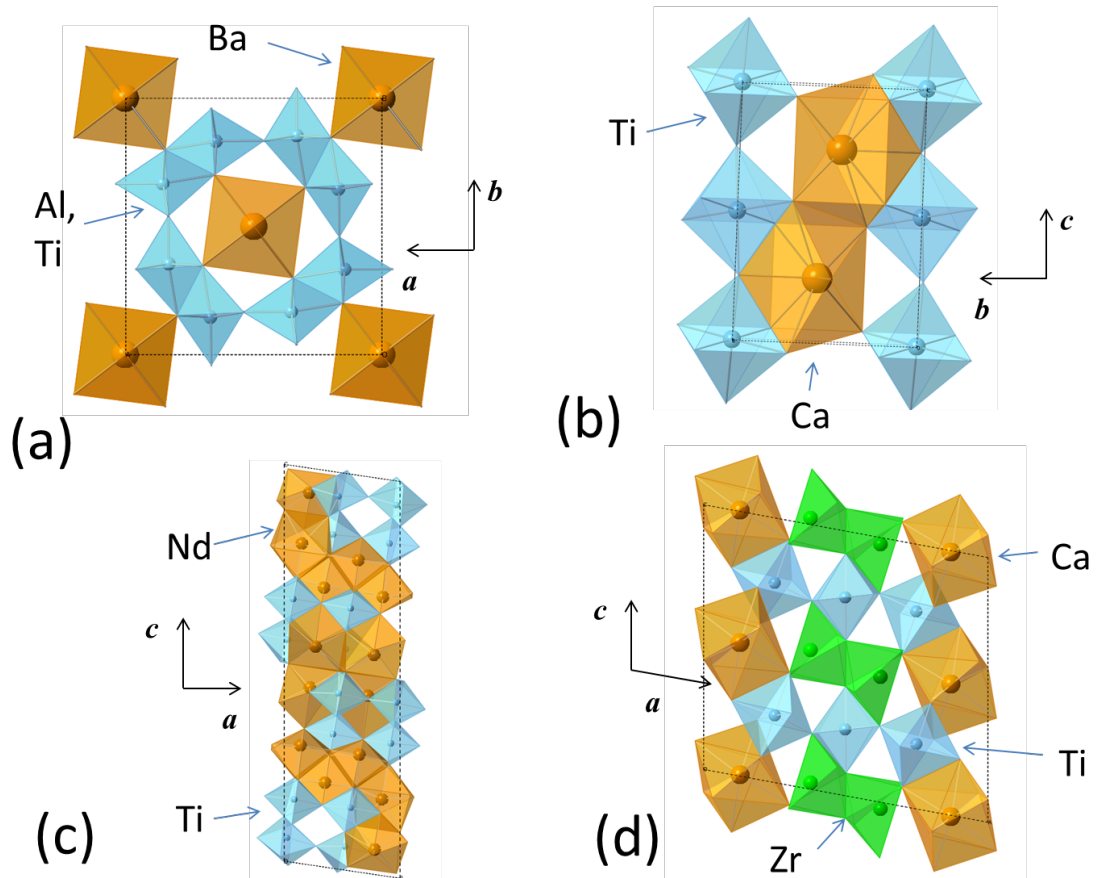


Figure I-1. Unit cells of representative members of major phases of SYNROC family (a) Hollandite –  $Ba_2Al_2Ti_6O_{16}$  (b) Perovskite –  $CaTiO_3$  (c) Pyrochlore –  $Nd_2Ti_2O_7$  and (d) Zirconolite –  $CaZrTi_2O_7$ .

$Ba_xMn_8O_{16}$  is the natural mineral hollandite, where Mn can exist in any of the valence states 2+, 3+ or 4+. A large number of structural isotopes for hollandite exist, of which hollandite in  $BaO-Al_2O_3-TiO_2$  system,  $BaAl_2Ti_6O_{16}$ , is a key component in Synroc formulations. The structure (Figure I-1a) consists of tunnels running parallel to the

crystallographic c-axis that are surrounded by walls of edge sharing and corner sharing octahedra.<sup>20-22</sup> The general formula for the hollandite group is  $A_xB_yC_{8-y}O_{16}$  ( $x \leq 2$ ). ‘A’ represents the large monovalent and divalent cations (Na, K, Cs, Rb, Ba, Sr, Pb) that occupy the tunnel sites along the c-axis. ‘B’ and ‘C’ sites represent the smaller cations occupying the centers of oxygen octahedra. ‘B’ can be divalent (Mg, Co, Ni, Cu, Zn, Mn) or trivalent (Al, Cr, Fe, Ga, Ir, Rh, Mo, Tc) and ‘C<sup>4+</sup>’ site can host Ti, Sn, Mn, Ge, Si, Ru, Mo, and Tc.<sup>19</sup> Since the structure can accommodate a wide range of elements, different compositions of hollandite are studied for effective confinement of Cs. Further structural details of hollandite are discussed in Section B.

Perovskites constitute a major portion of Synroc materials. In general, perovskites have cubic symmetry ( $Pm\bar{3}m$ ), with a general formula  $ABO_3$ . ‘A’ represents the larger cation and ‘B’ represents the smaller cation. The structural framework consists of corner-shared  $BO_6$  octahedra forming a center cavity, with 12-fold oxygen coordination for A cations (Figure I-1b).<sup>23</sup> Ionic radii ratio and charge neutrality determine the phase stability of perovskites. Wide ranges of cation combinations are possible that preserve the perovskite structure –  $A^{2+}B^{4+}O_3$ ,  $A^{3+}B^{3+}O_3$  and  $A^{1+}B^{5+}O_3$ .<sup>23</sup> In Synroc, titanate perovskites ( $CaTiO_3$ ) are predominantly formed with  $Sr^{2+}$  substituting a fraction of  $Ca^{2+}$ . All trivalent rare-earth elements are also capable of replacing  $Ca^{2+}$  and  $Ti^{4+}$  can be replaced by other trivalent ions like Al, Fe, Cr or Ga.<sup>4</sup> Other higher valence ions ( $Zr^{4+}$ ,  $U^{5+}$ ,  $Pu^{4+}$ ,  $Th^{4+}$ ) can substitute  $Ti^{4+}$  but are reported to have very low solubility in perovskites.<sup>26</sup> Perovskites have<sup>24</sup> the highest leachability compared to other phases in Synroc and has a better resistance to radiation damage.<sup>25,26</sup>

Pyrochlores ( $A_2B_2O_7$ ) are of interest for waste form applications because of their ability to incorporate actinides, especially Pu, in their structure. The structure (Figure I-1c) of pyrochlore is related to a defect fluorite and can be envisioned as built up layers of perovskite sheets.<sup>27</sup> Wide range of cations  $A^{3+}/B^{4+}$  or  $A^{2+}/B^{5+}$  can form a stable pyrochlore structure. The important factor determining the stability of pyrochlores under irradiation is the size difference between ‘A’ and ‘B’ cations. Smaller the size difference, more stable the phase would be when irradiated with ion beams.<sup>28,29</sup> This can be attributed to antisite defect formation where ‘A’ and ‘B’ cations can exchange their sites under irradiation, easily forming a disordered fluorite structure.<sup>30</sup>

Zirconolite,  $\text{CaZr}_2\text{Ti}_2\text{O}_7$ , can incorporate rare-earth elements and actinides into its structure. It can undergo isomorphic substitution by different cations resulting in different symmetries.<sup>4</sup> The structure of monoclinic zirconolite (Figure I-1d) is closely related to pyrochlore structure with five cation (Ca, Ti and Zr) sites, three of which are occupied by Ti. Two of the Ti sites are six-fold coordinated and the third site is five-fold coordinated and has 50% occupancy.<sup>31</sup> The zirconolite lattice is made up of alternating layers of Ti polyhedra and planes of Ca and Zr that lie parallel to (001) planes. The Ca and Zr atoms are aligned in alternating [110]-type rows with 8-fold and 7-fold coordinated polyhedra, respectively. There is a rotation of  $180^\circ$  around the c-axis between a pair of layers.<sup>32</sup> Zirconolite has been considered to be a major actinide host because of the structural instability concerns of pyrochlore phases under irradiation.<sup>30,33</sup> The incorporation of actinides like U, Np, Pu and other rare-earth elements were studied by various research groups.<sup>34,35</sup>  $\text{U}^{4+}$  can occupy either  $\text{Zr}^{4+}$  site or  $\text{Ca}^{2+}$  site. However, it was observed that a significant amount of pyrochlore phase was also obtained when doping zirconolite with  $\text{U}^{4+}$ . The addition of smaller cations like  $\text{Mg}^{2+}$  can facilitate the substitution of  $\text{U}^{4+}$  on the  $\text{Ca}^{2+}$  site. The stability of pyrochlore and zirconolite phases, the major actinide hosts in Synroc, under extreme conditions is important. Roberts et al.<sup>36</sup> reported the leachability of  $\text{U}^{4+}$  in zirconolite and pyrochlore ( $\text{Gd}_2\text{Ti}_2\text{O}_7$ ), which was relatively very low compared to the other waste forms reported. Both these materials are prone to self-irradiation over a period of time due to  $\alpha$ -decay. Pyrochlore radiation resistance depends strongly on composition, as pointed out earlier. For example, radiation resistance was found to increase with Zr content in the pyrochlore  $\text{Gd}_2(\text{Zr}_x\text{Ti}_{1-x})\text{O}_7$ .<sup>37</sup> In case of zirconolites, various authors have reported severe damage in Pu doped systems.<sup>38-40</sup>

## B. Structural and Phase Chemistry of Hollandite

Synthetic hollandites structurally analogous to natural mineral hollandite  $\text{Ba}_x\text{Mn}_8\text{O}_{16}$ <sup>41</sup> have been developed for several potential applications, such as battery anode materials<sup>42,43</sup>, multiferroics,<sup>44,45</sup> nuclear waste hosts<sup>5,46</sup> etc. Hollandite  $\text{Ba}_x(\text{Mn}^{4+}\text{Mn}^{3+})_8\text{O}_{16}$  mineral structure was first solved by Byström and Byström<sup>41</sup> using a tetragonal structure model (I4/m). Subsequent studies by Post et al<sup>47</sup> reported a monoclinic (I2/m) distortion to the tetragonal symmetry in manganese hollandite minerals. The crystal structure is made of a continuous framework of edge-shared and corner-shared oxygen octahedral creating long, one-dimensional tunnels enclosed by four walls of edge-shared octahedral, which are connected at corners.  $\text{Mn}^{3+}$  and  $\text{Mn}^{4+}$  occupy octahedral sites while large cations, e.g.,  $\text{Ba}^{2+}$ , occupy the tunnel sites. Traces of substitutional elements  $\text{Pb}^{2+}$ ,  $\text{K}^+$ ,  $\text{Na}^+$  on tunnel sites,  $\text{Si}^{4+}$ ,  $\text{Ti}^{4+}$ ,  $\text{Al}^{3+}$ ,  $\text{Fe}^{3+}$ ,  $\text{Cr}^{3+}$  or  $\text{Ti}^{3+}$  on octahedral sites are common in hollandite minerals.<sup>41,47</sup> To maintain charge neutrality, incorporation of cations into the tunnels requires reduction of the octahedral cations, such as  $\text{Mn}^{4+}$  to  $\text{Mn}^{3+}$  or  $\text{Ti}^{4+}$  to  $\text{Ti}^{3+}$ , or substitution by cations of lower oxidation state. The evident flexibility in the crystal chemistry of the mineral hollandites has led to the development of several synthetic hollandites, where the compositional modifications offer unlimited opportunities to tune the electronic and magnetic properties, ionic conductivities etc. The hollandite family can be represented by a general formulation  $A_xB_8O_{16}$  with  $A$  representing the tunnel cations and  $B$  octahedral cations. A unit cell of  $A_xB_8O_{16}$  can have a maximum of two tunnel cations ( $x \leq 2$ ).  $A$  site typically hosts monovalent and divalent alkaline-earth metals such as  $\text{Li}^+$ ,  $\text{Na}^+$ ,  $\text{Ba}^{2+}$ ,  $\text{Cs}^+$ ,  $\text{Rb}^+$ , etc.  $B$  site accommodates a wide range of metals or transition elements with varying sizes and oxidation states such as  $\text{Al}^{3+}$ ,  $\text{Mg}^{2+}$ ,  $\text{Fe}^{2+}$ ,  $\text{Fe}^{3+}$ ,  $\text{Ti}^{3+}$ ,  $\text{Ti}^{4+}$ ,  $\text{Ni}^{2+}$ ,  $\text{Sn}^{4+}$ ,  $\text{Cr}^{3+}$ , etc. Depending on the average sizes of tunnel cations ( $\bar{r}_A$ ) and octahedral cations ( $\bar{r}_B$ ), synthetic hollandites can be of tetragonal (I4/m) symmetry, with tunnel along the crystallographic  $c$ -axis, or monoclinic (I2/m) symmetry with  $b$ -axis as tunnel direction. Figure I-2 shows a schematic of tetragonal hollandite unit cell. In an ideal tetragonal hollandite, where all  $\text{BO}_6$  octahedra are identical, there is one distinct crystallographic site for tunnel ( $A$ ) and octahedral ( $B$ ) cations and two for oxygen ions (O1 and O2). The electrostatic repulsions

between the cations in octahedral columns within each tunnel wall produce off-center shifts in the *B* cation sites. This results in the formation of distorted octahedra where the edge-shared bond lengths (O2-O2) reduce and the distance between oxygens within the same octahedra (O1-O2) increases.<sup>48</sup>

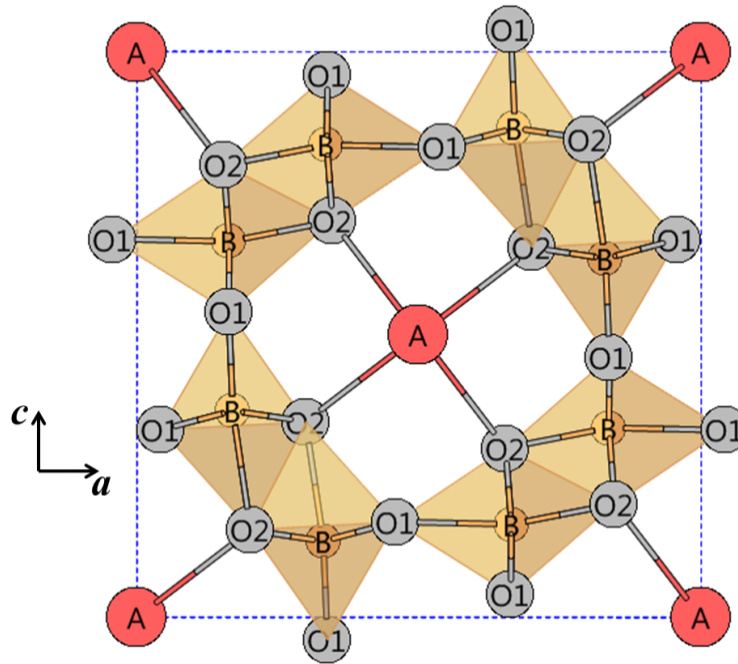


Figure I-2. Schematic of a tetragonal (*I4/m*) hollandite unit cell viewed down the *c*-axis.

The transition from tetragonal to monoclinic symmetry occurs when the ratio  $\bar{r}_B/\bar{r}_A$  is increased. The instability of tunnel cavity due to the presence of larger octahedral cations and smaller tunnel cations is compensated by the rearrangement of octahedral framework. The square cross-section of the tunnels in *I4/m* hollandites transforms to a parallelogram by small twisting of each of the tunnel walls along an axis running approximately through the center of the edge-shared bonds and parallel to the tunnel direction. Figure I-3 illustrates the corresponding atomic displacements and the transition from tetragonal to monoclinic symmetry. A monoclinic hollandite (Figure I-3b) has one tunnel site, two distinct octahedra or B cation sites (B1 and B2), and four oxygen sites (O1, O2, O3 and O4). It is commonly understood that hollandites with larger octahedral cations and

smaller tunnel cations adopt monoclinic symmetry. Post et al.<sup>47</sup> have reported that beyond the ratio,  $\bar{r}_B/\bar{r}_A = 0.48$ , hollandites are monoclinic, however, this is not applicable to all hollandite systems.<sup>49</sup> In addition to the relative sizes of cations, other factors such as tunnel occupancy, interaction between tunnel cations and immediate neighbors, order/disorder of octahedral or tunnel cations may affect the symmetry of hollandites.<sup>49</sup>

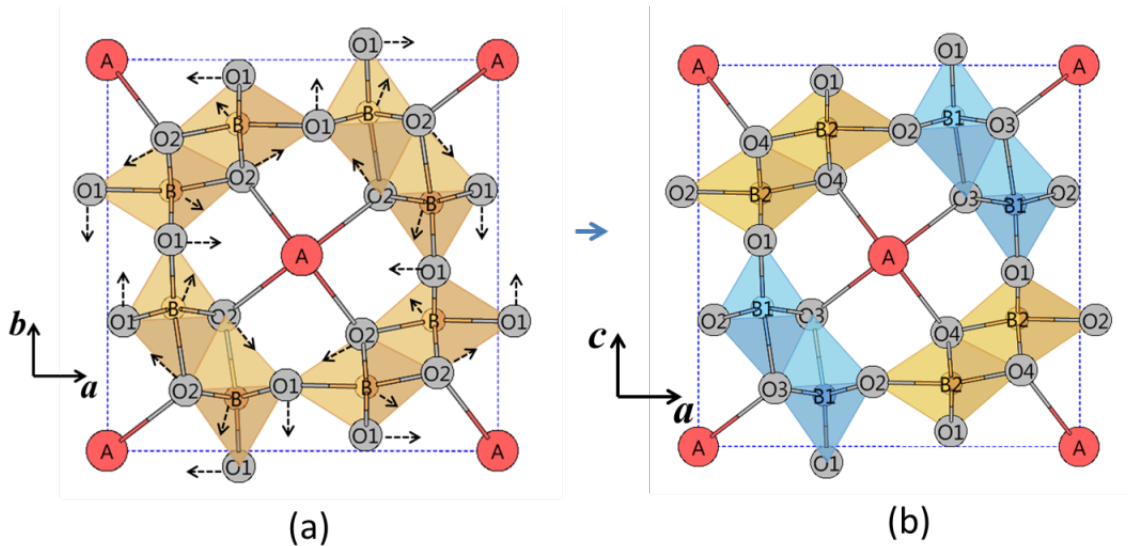


Figure I-3. (a) Tetragonal hollandite with atomic displacements due to octahedral twisting, indicated by dotted arrows, transforming to (b) monoclinic symmetry. Oxygen octahedra on opposite tunnel walls are identical in monoclinic symmetry (B1O<sub>6</sub> and B2O<sub>6</sub>).

Hollandites of the family BaO – M<sup>3+</sup><sub>2</sub>O<sub>3</sub> – TiO<sub>2</sub> are considered as potential ceramic hosts for radioactive Cs immobilization. Hollandite is one of the major phases of Synroc – a multiphase ceramic material intended to incorporate radioactive elements from nuclear waste.<sup>2,18,19</sup> In Synroc formulations, hollandite is specifically targeted to contain Cs, which is one of the challenging waste elements to confine due to its high volatility, while processing and its high mobility pose a threat to biosphere when the waste form is altered in the geologic repository.<sup>3,50</sup> The general composition of the Synroc hollandite [Ba<sub>x</sub>Cs<sub>y</sub>][M<sup>3+</sup><sub>2x+y</sub>Ti<sup>4+</sup><sub>8-2x-y</sub>O<sub>16</sub>] is also intended to be stable to the redox reactions induced by the  $\beta$ -decay of Cs:  $^{137}\text{Cs} \rightarrow ^{137}\text{Ba} + \beta(e^-)$  and  $\text{Ti}^{4+} + \beta(e^-) \rightarrow \text{Ti}^{3+}$ .

The choice of the trivalent cation is crucial since it affects the lateral dimensions of the tunnels and thus, the amount of Cs loading in the lattice. Further, depending on the ratio of the average radius of tunnel cations (Ba and Cs) and octahedral cations ( $M^{3+}$  and  $Ti^{4+}$ ), hollandite unit cell symmetry can be tetragonal (I4/m) or monoclinic (I2/m).<sup>3,49</sup> One of the characteristic features of hollandites is that, when Ba and/or Cs are used as tunnel cations, the tunnel sites are always only partially occupied due to the electrostatic repulsions between neighboring sites.<sup>51</sup> In such situations, the cations along with the vacancies might have an ordered arrangement along the individual tunnels resulting in the formation of superstructures. Several studies have demonstrated these phenomena.<sup>49,52-55</sup> It was also reported that in addition to this intratunnel arrangement, correlation might exist between different tunnels that would result in 3-dimensional superstructures.<sup>3,52</sup> Figure I-4 shows a schematic of monoclinic hollandite supercell structure with intratunnel cation ordering and correlation between tunnels along the *a*-direction. The multiplicities of these superstructures are directly related to the occupancy of the tunnels, which in turn depend on the cation combinations used in hollandite formulations. Further, in each of these superstructures, there exists a disorder in the location of the tunnel cations ( $\delta y$ ) that arises due to the dissimilar neighboring sites as illustrated in Figure I-4.

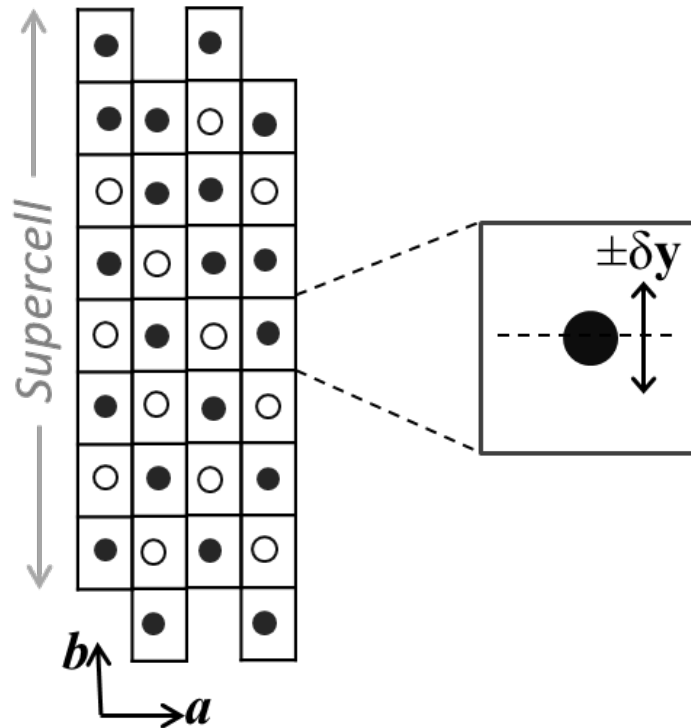


Figure I-4. Schematic view of a monoclinic hollandite superstructure, with a tunnel occupancy of 0.625, along [001] direction. Four different super cells, each made of eight unit cells are shown. Ordering of cations and vacancies across in each of the supercells can be observed. Black solid circles indicate occupied sites and open circles indicate vacancies. The inset shows an individual unit cell showing the disorder in tunnel sites ( $x, y, z$ ):  $(0, 0, 0) \rightarrow (0, \pm\delta y, 0)$ .

The effects of  $M^{3+}$  cation on the structural stability, Cs loading, and the effectiveness of Cs retention of the hollandite lattice have been the subject of many studies.<sup>3,48,50,52,56-59</sup> Recent works have shown that Cr-hollandites ( $M^{3+}=\text{Cr}^{3+}$ ), when compared to Al and Fe counterparts, have the highest Cs retention after leaching tests<sup>50</sup> and form at relatively low temperature  $\sim 900^\circ\text{C}$  with no secondary phases.<sup>59</sup> Even when the waste form is processed as a multiphase material, majority of the Cs containing hollandite phase contains Cr.<sup>60,61</sup>

### **C. Scope of this Study**

The overall objectives of this study are primarily to characterize and validate different processing methods for the preparation of multiphase waste forms and perform fundamental studies related to the materials science of crystalline ceramic waste forms. The work has been designed and structured to advance the scientific and technical background of ceramic waste forms. This thesis is divided into two parts, one on multiphase waste form and the other on single-phase waste form.

Part I on the multiphase waste form discusses waste form technology by presenting the pros and cons and validating melt-processing and SPS processes. Simulated waste form compositions prepared by either process were evaluated from the perspective of phase and elemental distribution, and their effects on chemical durability. In addition, melt-processing was further studied in detail to determine the overall phase changes that occur during the heating and cooling processes. The results provide guidelines to understand or manipulate the heating cycle thereby enhancing or suppressing the growth of selected phase(s).

Part II on the single-phase waste form focuses primarily on hollandites for Cs immobilization. The challenges associated with Cs incorporation have been discussed in Section I – 2. This part aims to identify a desirable hollandite composition for effective Cs incorporation and understand the structural effects of Cs addition. Series of experiments were performed with hollandites with varying chemistries to compare the relative ease of the hollandite phase evolution. The results suggest that the Ba-Cr-Ti-O hollandite system is effective for Cs incorporation.

Major emphasis of the thesis is on the structural features of the selected hollandite lattice and the associated effects with Cs incorporation. Detailed structural characterization has been carried out using a combination of complimentary techniques – X-ray diffraction (XRD), neutron diffraction, and electron diffraction. Appropriate structural models have been generated for the Cs-substituted single-phase hollandite compositions. The resultant structural data is valuable for further experimental and simulation studies to understand the fundamental science of hollandite interaction with a specified environment or with any type of induced irradiation.

## D. Thesis Outline

The overall results and discussions of this thesis are divided into five different sections (Section III – VII). Sections III and IV present the findings related to multiphase waste forms and the following Sections V – VII are focused on single-phase hollandites. Section II, **Materials and Methods**, presents the selection of compositional space for the processing of multiphase and phase-pure hollandites. All processing methods used in this study are described in this section. Specific characterization techniques and details are presented in appropriate sections.

In Section III, **Microstructural Characterization of Multiphase Ceramic Waste Forms**, the microstructural features of multiphase waste forms prepared by melt-processing and SPS are characterized and compared. Process induced variations in Cs elemental partitioning into the hollandite phase are explained in detail. The following Section IV, **Crystallization Behavior During Melt-Processing of Multiphase Ceramic Waste Forms**, discusses the evolution and transformation of different phases during melt-processing. The crystallization behavior of the multiphase composition determined by in-situ methods is presented.

Section V, **Phase Evolution Studies of  $\text{Ba}_{1.0}\text{Cs}_{0.3}\text{M}_{2.3}\text{Ti}_{5.7}\text{O}_{16}$  ( $M = \text{Al, Cr, Fe}$ ) Hollandites**, captures the phase evolution of hollandite - with temperature in different selected compositions. This is critical to designing the thermal cycles during melt-processing or any other sintering processes. Lowering the temperature of the hollandite phase formation, and lowers the loss of Cs due to volatilization. Section VI, **Structural Characteristics of Phase-Pure Hollandites  $\text{Ba}_{1.15-x}\text{Cs}_{2x}\text{Cr}_{2.3}\text{Ti}_{5.7}\text{O}_{16}$  for Cs Immobilization**, presents the structural characterization of Ba-Cr-Ti-O hollandite. The choice of the composition and effects of Cs addition on structural properties of  $\text{Ba}_{1.15-x}\text{Cs}_{2x}\text{Cr}_{2.3}\text{Ti}_{5.7}\text{O}_{16}$  lattice have been discussed. Section VII, **Performance of Phase-Pure Hollandites** presents a preliminary evaluation of the performance of the Cs-substituted hollandites as evaluated by chemical durability tests and irradiation tests. Chemical durability of the phase-pure hollandites was measured by standard ASTM leaching tests<sup>62</sup> to determine the retention of Cs. Heavy ion irradiation was used to study the radiation resistance.

## MATERIALS AND METHODS

### A. Materials

#### A.1. Multiphase Compositions

Savannah River National Laboratory (SRNL) developed the multiphase waste form composition<sup>59,63</sup> and provided batch materials for the experiments. The multiphase composition was based on the simulated waste stream compositions that are currently being investigated under the DOE Fuel Cycle Research and Development (FCR&D) program. Stoichiometric amounts of reagent-grade oxides and carbonates were blended together, mixed in de-ionized water with zirconia media, and dried at 90°C. The resulting material was used as feedstock for our experiments. The target composition, hereafter indicated as CAF-MP, is listed in Table II-1.

Table II-1. Target Composition of Multiphase Waste Form CAF-MP

	Target wt.% of each oxide in CAF-MP		Target wt.% of each oxide in CAF-MP
Al <sub>2</sub> O <sub>3</sub>	1.27	MoO <sub>3</sub>	0.85
BaO	12.76	Nd <sub>2</sub> O <sub>3</sub>	5.23
CaO	1.39	Pr <sub>2</sub> O <sub>3</sub>	1.45
Cr <sub>2</sub> O <sub>3</sub>	6.33	SeO <sub>2</sub>	0.08
CdO	0.11	Sm <sub>2</sub> O <sub>3</sub>	1.08
Ce <sub>2</sub> O <sub>3</sub>	3.10	SnO <sub>2</sub>	0.07
Cs <sub>2</sub> O	2.88	SrO	0.98
Eu <sub>2</sub> O <sub>3</sub>	0.17	TeO <sub>2</sub>	0.66
Fe <sub>2</sub> O <sub>3</sub>	6.65	TiO <sub>2</sub>	49.16
Gd <sub>2</sub> O <sub>3</sub>	0.16	Y <sub>2</sub> O <sub>3</sub>	0.63
La <sub>2</sub> O <sub>3</sub>	1.58	ZrO <sub>2</sub>	2.99

## A.2. Phase-Pure Hollandite Compositions

The generalized Synroc hollandite formulation  $[\text{Ba}_x\text{Cs}_y][M^{3+}_{2x+y}\text{Ti}^{4+}_{8-2x-y}\text{O}_{16}]$  has different domains of  $x$  and  $y$ , for each  $M^{3+}$ , where phase-pure hollandite can be formed. Table II-2 presents the domains of  $x$  for hollandite phase stability in case of Cs-free compositions ( $y = 0$ ). The value of  $y$  can be varied with the condition  $x + y \leq 2$  with the actual range of  $y$  for hollandite stability is dependent on the nature of  $M^{3+}$  and the corresponding value of  $x$ . The different compositions listed in Table II-2 were used for the phase evolution studies (Section V) and the composition with  $M^{3+} = \text{Cr}^{3+}$  was selected for structural characterization studies (Section VI) as discussed in the respective chapters.

Table II-2. Values of  $x$  for Single-Phase Region of  $\text{Ba}_xM^{3+}_{2x}\text{Ti}^{4+}_{8-2x}\text{O}_{16}$

$M$ cation	Domain of $x$ yielding single-phase of $\text{Ba}_xM^{3+}_{2x}\text{Ti}^{4+}_{8-2x}\text{O}_{16}$	References
$\text{Al}^{3+}$	1.16 – 1.28	64,65
$\text{Cr}^{3+}$	1.12 – 1.34	64,65
$\text{Fe}^{3+}$	1.10 – 1.30	66

## B. Sample Preparation

### B.1. Melt-Processing

Melt-processing of small batches of material were accomplished in an electrically heated tube furnace. Approximately 10g of the starting material, loosely packed in a Pt foil, was heated to 1500°C at a rate of 5 K/min, held for 30 minutes, and furnace-cooled back to room temperature. The solidified material was removed from the foil and used for characterization.

### B.2. Spark-Plasma Sintering (SPS)

Reactive SPS was carried out using a FCT HP D 25 (FCT Systeme GmbH, Rauenstein, Germany) furnace with graphite dies and punches. Figure II-1 presents the schematic description of the die setup. The unreacted starting powder (~3g) enclosed

within a thin graphite foil was placed inside a graphite die. The reactive sintering was performed under a pressure of 54 MPa by heating the die set-up to a maximum temperature of 1000°C at a heating rate of 100 K/min, holding for 3 minutes, and cooling back at a rate of 100 K/min.

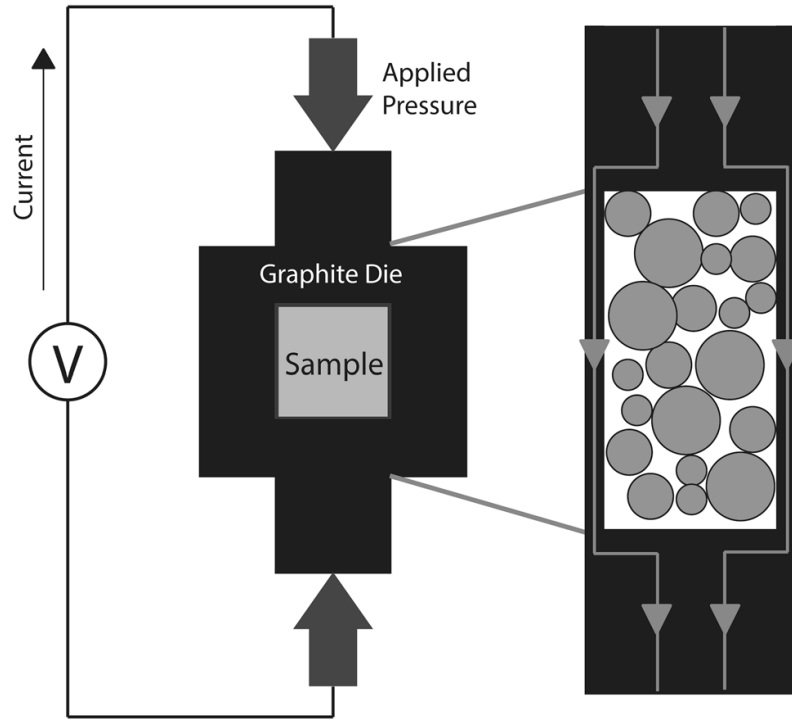


Figure II-1. Schematic of the graphite die setup in SPS.<sup>67</sup>

### B.3. Sol-gel Synthesis

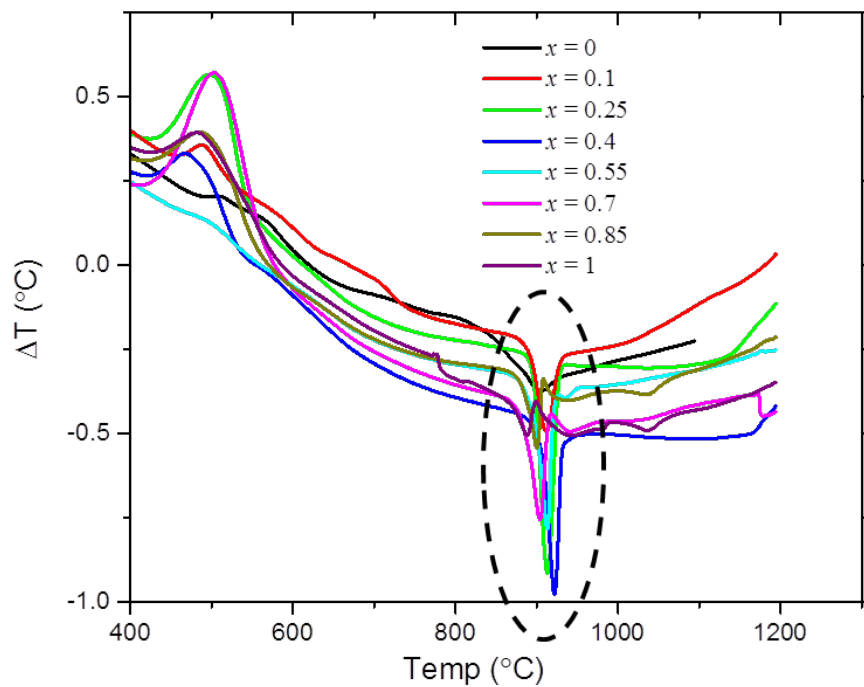
Sol-gel method was used to prepare single-phase  $\text{Ba}_{1.15-x}\text{Cs}_{2x}\text{Cr}_{2.3}\text{Ti}_{5.7}\text{O}_{16}$  hollandites. This method was chosen to prepare powders with homogeneous chemistry and minimize Cs losses during subsequent sintering. Solution-based routes such as alkoxide or sol-gel methods have been reported for synthesis of different hollandite compositions.<sup>3,58</sup> The precursor materials and the corresponding solutions used in this method are listed in Table II-3. These solutions were prepared using stoichiometric amounts of precursor solutes mixed together while stirring. Since the overall volume of the mixed precursor solution was high (~100 ml/g of required material), conventional

drying on a hot-plate would result in chemical gradients in the resultant powder. To avoid this, rotary evaporator was used to dry the precursor solution at 90°C. The resultant homogeneous dry residue was used as precursor for further solid-state processing. Initial calcination of the as-obtained dry residue was performed at 400°C for 2h to remove all volatiles.

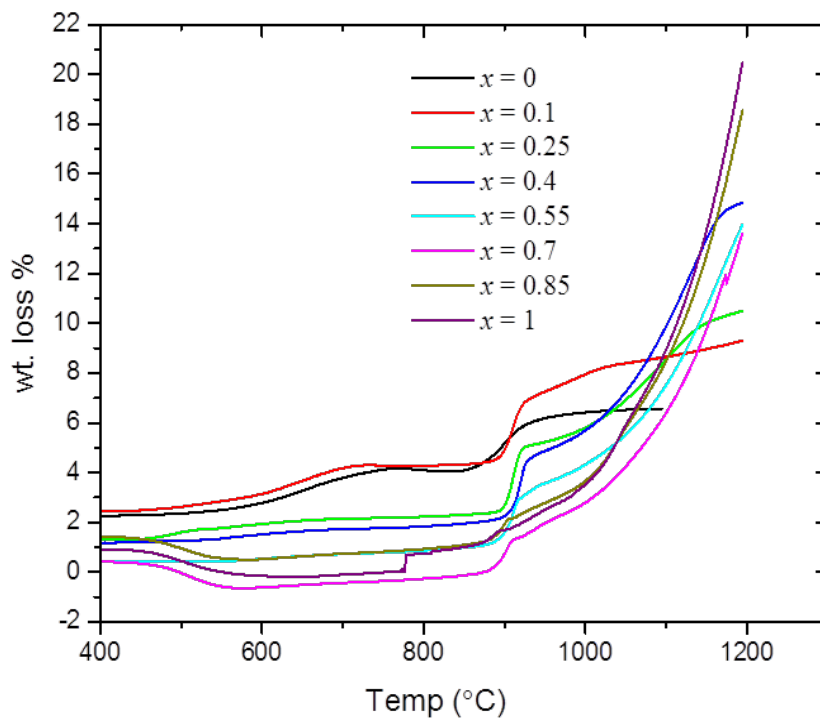
Table II-3. Precursor Materials Used for Sol-gel Synthesis

<b>Cation</b>	<b>Precursor solution</b>	
	<b>Solute</b>	<b>Solvent</b>
Ba <sup>2+</sup>	Barium acetate (Ba(O <sub>2</sub> H <sub>3</sub> C <sub>2</sub> ) <sub>2</sub> )	Acetic acid
Cs <sup>+</sup>	Cesium carbonate (Cs <sub>2</sub> CO <sub>3</sub> )	Acetic acid
Ti <sup>4+</sup>	Titanium isopropoxide (Ti(OC <sub>3</sub> H <sub>7</sub> ) <sub>4</sub> )	Acetic acid + ethanol
Cr <sup>3+</sup>	Chromium nitrate (Cr(NO <sub>3</sub> ) <sub>3</sub> .9H <sub>2</sub> O)	Isopropanol

Hollandite formation temperatures for all compositions were determined by thermal analysis studies. Differential thermal analysis (DTA) and thermogravimetric analysis (TGA) curves for the dried sol-gel precursor, measured by a Q600-DST thermal analyzer (Texas Instruments, DE, USA), are shown in Figure II-2.



(a)



(b)

Figure II-2. (a) DTA and (b) TGA curves corresponding to different compositions of the series  $\text{Ba}_{1.15-x}\text{Cs}_{2x}\text{Cr}_{2.3}\text{Ti}_{5.7}\text{O}_{16}$ .

The exothermic event close to 900°C (indicated in Figure II-2a) was identified as the hollandite formation temperature in all cases. The corresponding weight loss can be seen from the TGA plots (Figure II-2b). Hence, the calcined powders are sintered at 1050°C/3h to form hollandites. The apparent densities of the samples measured using Archimedes principle were in the range 80 - 85% of theoretical density. The phase-purity of the resultant materials is further discussed in Section VI.

#### **B.4. Solid-state sintering**

In addition to the above mentioned processes, single-phase hollandites,  $\text{Ba}_{1.15-x}\text{Cs}_{2x}\text{Cr}_{2.3}\text{Ti}_{5.7}\text{O}_{16}$ , were also prepared by conventional solid-state sintering techniques when required. In a typical process, stoichiometric amounts of the commercially available oxides/carbonates were mixed, ball-milled and dried at  $\sim 120^\circ\text{C}$  to form the precursor batch. The precursors or precursor batches were compacted into pellets and subsequently sintered at  $1100^\circ\text{C}$  for 4h. This sintering temperature for  $\text{Ba}_{1.15-x}\text{Cs}_{2x}\text{Cr}_{2.3}\text{Ti}_{5.7}\text{O}_{16}$  was chosen based on the DSC data shown in Figure II-2. The apparent density of solid-state sintered samples measured using Archimedes principle increased with Cs composition. The composition with no Cs ( $x = 0$ ) was  $\sim 70\%$  dense, while the composition with highest Cs ( $x = 0.4$ ),  $\sim 85\%$  dense.

## MICROSTRUCTURAL CHARACTERIZATION OF MULTIPHASE CERAMIC WASTE FORMS

Distinct microstructures are generated when the multiphase ceramic waste forms are processed via different routes. The microstructures dictate the radionuclide retention and the chemical durability of the waste forms. In this Chapter, the effects of processing methods, phase assemblage and elemental distribution, and the subsequent consequences on durability are presented. CAF-MP waste form materials prepared by melt-processing and spark plasma sintering following the procedures mentioned in Section I.B have been used for this investigation. The corresponding sample variants are hereafter indicated as CAF-MP-Melt and CAF-MP-SPS, respectively.

### A. Characterization Methods

Powder XRD data was collected for preliminary phase identification using a D-2 Phaser (Bruker, Massachusetts). Scanning electron microscopy (SEM) and electron back-scattered diffraction (EBSD) studies were performed using a high-resolution JEOL 7600F (JEOL Ltd., Tokyo, Japan) field-emission SEM equipped with a Nordlys detector (Oxford Instruments, UK) for EBSD, complete with the HKL Channel5 software package and a low-angle backscatter electron (LABE), was used to collect Kikuchi diffraction patterns. Further phase assemblage and elemental distribution were studied by wavelength dispersive spectroscopy (WDS). Selected elemental maps from multiphase regions, identified from back-scattered electron (BSE) images, were collected using JEOL JXA-8200, WD/ED Combined Electron Probe Microanalyzer (EPMA) (JEOL Ltd., Tokyo, Japan). Elemental scans were performed at an accelerating potential of 15kV, with a step size of 0.5 $\mu$ m in *x*- and *y*- directions, and a dwell time of 80 milliseconds at each point.

Electron-transparent samples for transmission electron microscope (TEM) analysis were prepared using DualBeam<sup>TM</sup> FEI Strata 400 focused ion beam (FIB) microscope (FEI, Hillsboro, USA) equipped with Omniprobe. Since hollandite is the

phase of interest, a region with coarse hollandite grains on the surface was selected. A fragment  $\sim 10 \mu\text{m}$  deep and a lateral cross section of  $\sim 20 \times 3 \mu\text{m}^2$  was removed, which was further ion-milled until electron-transparent area was obtained for the hollandite phase sample. Selected area electron diffraction (SAED) patterns and high-resolution lattice images were collected using F20 Tecnai (FEI, Hillsboro, USA) field emission TEM at an operating voltage of 200kV.

## **B. Results and Discussions**

### **B.1. Phase Analysis and Elemental Distribution**

As-prepared CAF-MP-Melt had a characteristic melt-solidified structure as evident from the wetting of the Pt foil. There was minimal chemical reaction with the Pt foil, as the sample could easily be removed from the foil. CAF-MP-SPS sample was relatively stronger and denser, as typical of SPS processed material. The measured bulk density was relatively high ( $4.64 \text{ g/cm}^3$ ) compared to that of CAF-MP-Melt ( $4.07 \text{ g/cm}^3$ ). Melt-processing and SPS of CAF-MP produced similar phases as seen from the powder XRD patterns, as shown in Figure III-1. Microstructures of SPS and melt-processed samples are shown in the corresponding BSE images. Initial phase identification was performed based on the collective information from the XRD patterns and point chemical analysis using SEM-Energy Dispersive Spectroscopy (SEM-EDS) results. Hollandite was the major phase followed by perovskite and pyrochlore/zirconolite. Small amount of  $\text{TiO}_2$  was also observed from the XRD patterns. CAF-MP-Melt exhibited the typical melt-solidified microstructure containing large grains of different phases and large pores trapped between growing phases, while CAF-MP-SPS exhibited less porosity and a fine-grained microstructure. The SPS microstructure is a matrix of hollandite phase with small islands of other distributed phases. To identify the phases present and determine the microstructural phase distribution, EBSD analysis was performed. Electron back-scattered patterns (EBSP) or Kikuchi bands collected from different phases matched with the phases identified from XRD.

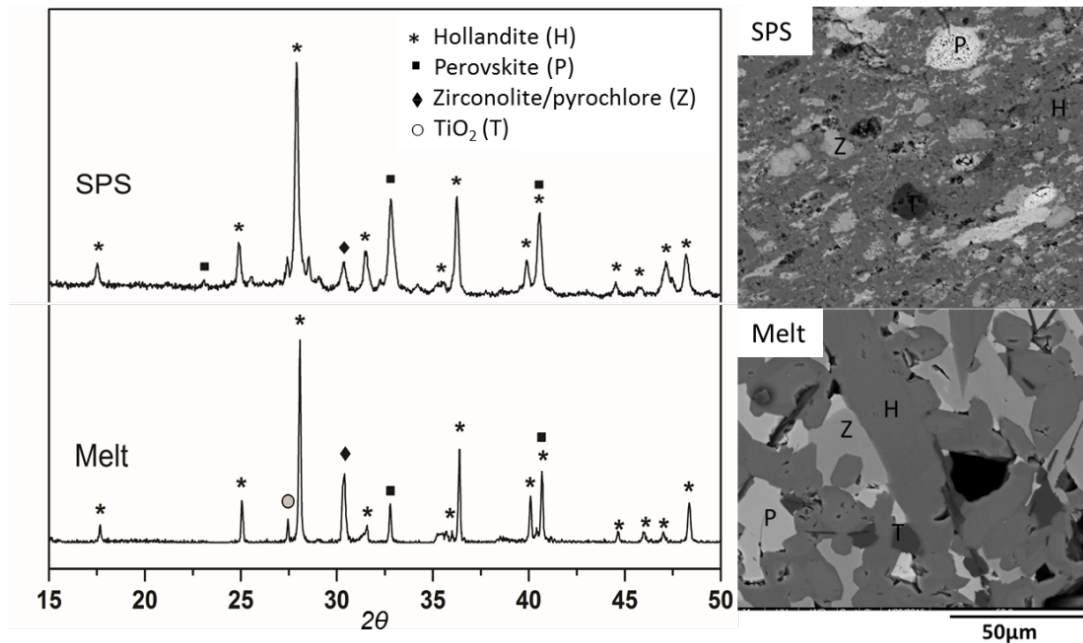


Figure III-1. XRD patterns and corresponding BSE images of CAF-MP-SPS and CAF-MP-Melt (H = Hollandite, P = Perovskite Z = Pyrochlore/Zirconolite, and T = TiO<sub>2</sub>).

Figure III-2 shows the band contrast maps and phase maps for SPS and melt-processing samples. In addition to the hollandite and perovskite phases in CAF-MP-SPS, unreacted CeO<sub>2</sub> was seen segregated, coexisting with pyrochlore or zirconolite phase. In Synroc-based formulations, Ce<sup>4+</sup> or Pu<sup>4+</sup> partitions into Nd-rich pyrochlore or zirconolite phases. This SPS microstructure can thus be interpreted as a snapshot of an ongoing transformation of CeO<sub>2</sub>. Given enough time, total Ce<sup>4+</sup> in the composition would have substituted into the pyrochlore lattice. EBSD maps together with BSE images reveal the microstructural development of SPS samples. Although the visual and microstructural examination indicated no bulk melting, there are indications of mass transport occurring within the samples during the sintering process. Phase distribution maps of CAF-MP-SPS show that the zones rich in perovskite and pyrochlore are randomly distributed in the hollandite-rich matrix and each zone in turn is polycrystalline. Detailed investigation of sintering mechanism during SPS is beyond the scope of this study.

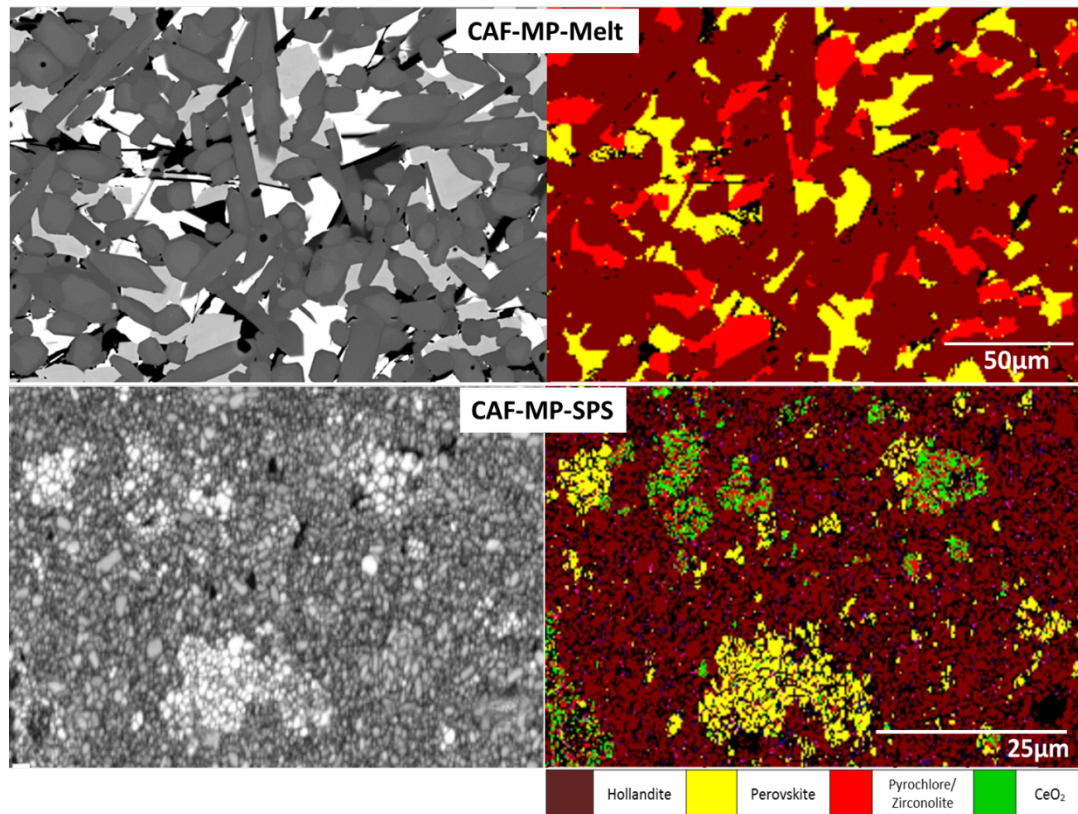


Figure III-2. Phase maps obtained from EBSD.

Figure III-3 shows the WDS maps of selected elements in CAF-MP-Melt. Hollandite, the major phase, consisted of primarily Ba, Cr, Fe, Ti and Cs. While Ba and Cs are homogeneously distributed, Cr and Fe have compositional gradients across individual grains, as seen in Figure III-3. Cr content is the highest at the core and diminishes towards the edges of the grains, whereas Fe has the exact opposite trend. The exact cause of this Cr and Fe segregation is not well understood yet. We attribute this to the competition between Fe and Cr for the oxygen within the grains. Ca is seen in both perovskite and pyrochlore phases but Zr is partitioned preferentially into pyrochlore phase.

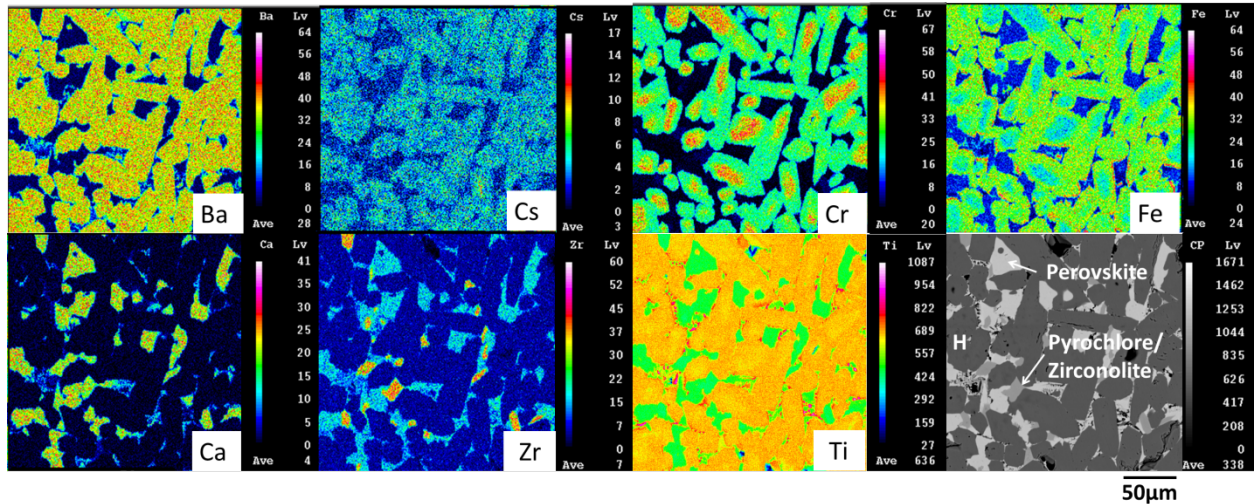


Figure III-3. WDS maps of selected elements of CAF-MP-Melt.

The elemental maps of CAF-MP-SPS sample shown in Figure III-4 do not provide the same individual phase resolution (owing to the grain size differences processed via different processes) as for the melt-processed sample but nevertheless provide key information. Ba and Cr can be used to identify the hollandite phase and are distributed throughout the sample. The Cs-rich regions observed in the WDS maps do not correlate with the Ba and Cr maps. Although the exact chemistry and crystal structure of these Cs-rich phases are not known, they are generally considered undesirable for waste form material due to their higher propensity to Cs attack by water on exposure. The maps confirm that the perovskite (Ca- and Nd-rich regions) and pyrochlore (Zr-rich) phases have appropriate targeted elements in the samples.

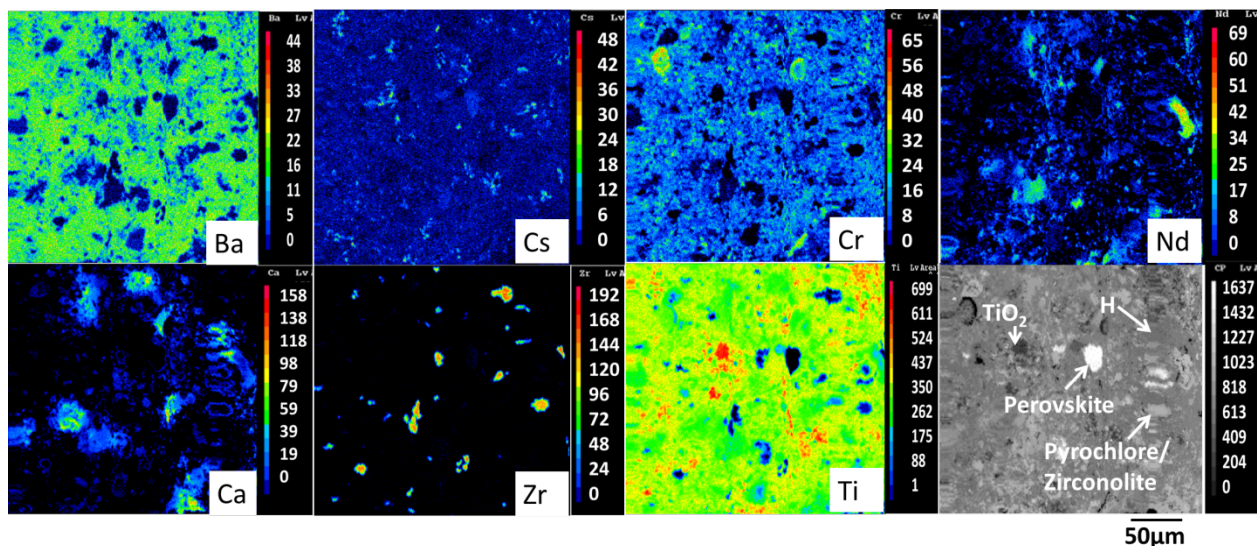


Figure III-4. WDS maps of selected elements of CAF-MP-SPS.

## B.2. TEM Observation of Hollandite Lattice

TEM observation of the FIB milled samples was performed to investigate the hollandite phase in detail. Since SPS samples were found not to have Cs incorporated into the hollandite lattice, TEM of CAF-MP-SPS was not performed in this study. SAED patterns collected from a hollandite region of CAF-MP-Melt could be indexed using monoclinic ( $I2/m$ ) unit cell structural model.<sup>49</sup> Figure III-5 shows the FIB milled fragment, hollandite lattice, and the corresponding electron diffraction pattern along the [011] zone axis. In addition to the strong Bragg reflections resulting from the octahedral framework shown in Figure III-5c, diffuse spots and streaks of low-intensity reflections can be seen. These additional satellite reflections are common in modulated structures and, in general, result from planar defects like stacking faults, twinning or compositional modulations.<sup>68,69</sup> In case of barium hollandites, the presence of these reflections are generally attributed to compositional modulations.

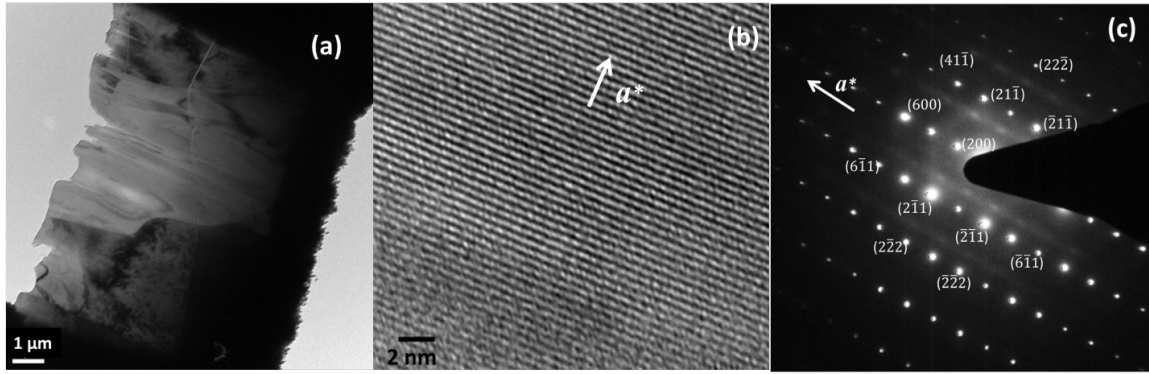


Figure III-5. (a) FIB-milled CAF-MP-Melt sample used for TEM observation, (b) Hollandite lattice as viewed from  $[011]$  zone axis, and (c) the corresponding SAED pattern.

The hollandite compositions for waste forms are typically designed in such a way that only a fraction of tunnel sites is occupied by Ba/Cs. It has been widely reported that the cations/vacancies adopt an ordered arrangement within the tunnels forming super lattice structures.<sup>52,54,55,65,70</sup> Along with this intratunnel ordering, intertunnel correlation also exists resulting in three-dimensional modulated structures in many cases. This has been demonstrated by comprehensive electron diffraction analysis as reported in several works.<sup>3,52,71</sup> While the Bragg spots can be indexed by integral multiples of reciprocal lattice vectors  $a^*$ ,  $b^*$  and  $c^*$ , satellite reflections are described by the nature of modulation.<sup>68,72</sup> In the SAED pattern shown in Figure III-5c, the satellite reflections and diffuse streaks run parallel to  $a^*$  as indicated and lie in the plane of  $a^*$  and  $b^*-c^*$ . Comparing it to the similar reported SAEDs,<sup>3,52</sup> it can be understood that there is compositional modulation in three-dimensions, i.e., ordering of cations along the tunnels together with intertunnel correlation in the hollandite lattice. Due to the limited degree of rotation of the FIB sample, SAED patterns along the principal axes could not be collected and hence, modulations or multiplicities along different directions could not be analyzed in detail. Nevertheless, our data suggests that the hollandite lattice in melt-processed multiphase waste form has three-dimensional ordering of Ba, Cs and/or vacancies. It is to be noted that the location of satellite reflections or the distribution of modulation vectors

is sensitive to the local composition. Different crystallites can have differing degrees of ordering of tunnel ions resulting in different multiplicities.<sup>73</sup>

It is also important to consider the implications on the performance of these materials as a waste form. Ba and Cs sites are typically enclosed in a box-shaped network of eight oxygen atoms. When Ba ions along the tunnels are replaced by larger Cs ions, local deformation occurs that has to be compensated by the surrounding tunnel sites to maintain lattice stability. Hence, Cs ions tend to occupy isolated sites rather than sites next to occupied Ba/Cs sites and adapt an ordered arrangement with Ba ions resulting in superstructures.<sup>48,53</sup> These superstructures can increase the activation barrier for Cs ions migrating to the adjacent tunnel sites.<sup>55</sup>

### **B.3. Conclusion**

Hollandite-rich waste forms prepared by melt-processing and SPS were observed to have similar phase assemblage containing hollandite, perovskite, pyrochlore-zirconolite phases, as supported by XRD and EBSD data. In SPS processed samples, small amounts of unreacted  $\text{CeO}_2$  was detected from EBSD phase maps. Cs partitioning into the hollandite phase, a primary focus of this study, was observed only for melt-processed sample. SPS processing resulted in separation of Cs-rich phases. Detailed electron diffraction patterns from melt-processed sample revealed super lattice reflections indicating an ordered arrangement of tunnel cations, Ba and Cs, and vacancies, resulting in a three-dimensional modulated structure. Our results suggest that melt-processing of waste forms can generate desirable microstructures and hence, can be considered as a potentially promising method for producing durable multiphase ceramic waste forms.

## **CRYSTALLIZATION BEHAVIOR DURING MELT-PROCESSING OF MULTIPHASE CERAMIC WASTE FORMS**

The crystallization of CAF-MP and the associated phase transformations during melt-processing is critical to implementing the melting process. The onset of melting/solidification of the material was studied using viscosity measurements. The crystallization process was studied using a set of complimentary techniques, e.g., standard thermal analysis techniques to determine the crystallization events followed by melt-quench studies. Further, in-situ high temperature XRD experiments were carried out to supplement the observations from thermal analyses. The results are summarized as follows.

### **A. Methodology**

#### **A.1. Viscosity measurements**

Viscosity, as a function of temperature, was measured in accordance with the American International C965 Procedure A<sup>74</sup> in which the viscosity was measured using a rotating spindle and a fixed crucible (both constructed of Pt-20%Rh alloy). A portion of melt-processed material was placed in the crucible and heated in a high temperature furnace. The temperature was initially set to achieve a condition (i.e. a melt or liquid-solid solution) in which the spindle could be lowered into the crucible. After steady-state conditions were obtained, the torque required to rotate the spindle at a constant speed was recorded using a Brookfield viscometer (Brookfield DV-II+, Brookfield Engineering Laboratories, USA). The temperature was then decreased incrementally and a series of such torque measurements at various temperatures was recorded until the viscosity increased beyond the instrument measurement capability. Subsequently, a duplicate measurement was taken near the initial temperature to confirm the reversibility of the viscosity behavior. Experimentally-derived instrument constants developed specifically for the SRNL system and verified with reference standards were used to calculate viscosity as a function of temperature from the recorded torque values.<sup>75</sup>

## A.2. Crystallization experiments

DSC data was used to investigate the crystallization behavior as a function of temperature. A SETSYS Evolution DSC instrument (SETARAM Inc., Hillsborough, NJ, USA) was used to measure the heat flow from the material during heating and cooling. Figure IV-1 summarizes the DSC heating and cooling cycles. The maximum temperature for DSC measurements is 1500°C, which was the melt-processing temperature used in this study. Heat cycles were chosen so that phase transformation behavior of CAF-MP, starting from unreacted stoichiometric mixture and as-formed compound, could be compared. 10 - 20 mg of starting material was heated under helium atmosphere in Pt crucibles. Two heating rates, 20 and 5 K/min, were used for this study.

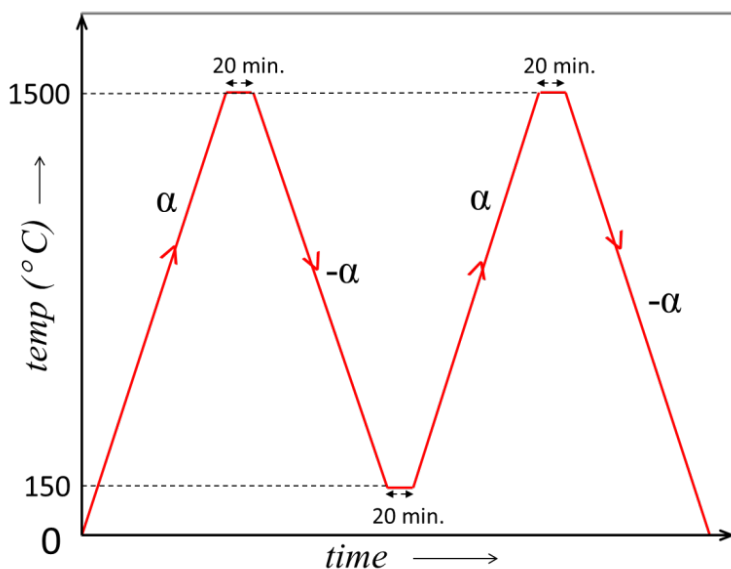


Figure IV-1. Temperature-time profile used for DSC experiments. ' $\alpha$ ' is the constant heating/cooling rate used.

Quenching experiments were performed to investigate the endothermic and exothermic events identified in the DSC data. Approximately, 4 - 5 g of the starting material was wrapped in a custom folded Pt foil and pinch sealed. These samples were heated to 1500°C ( $T_m$ ), held for 20 min, cooled to temperature ' $T$ ', equilibrated for time ' $t_{eq}$ ', and quenched in water by immersion. Temperature ' $T$ ' corresponded to exothermic peaks

identified in DSC data. Figure IV-2 summarizes the time-temperature cycles used for these experiments.

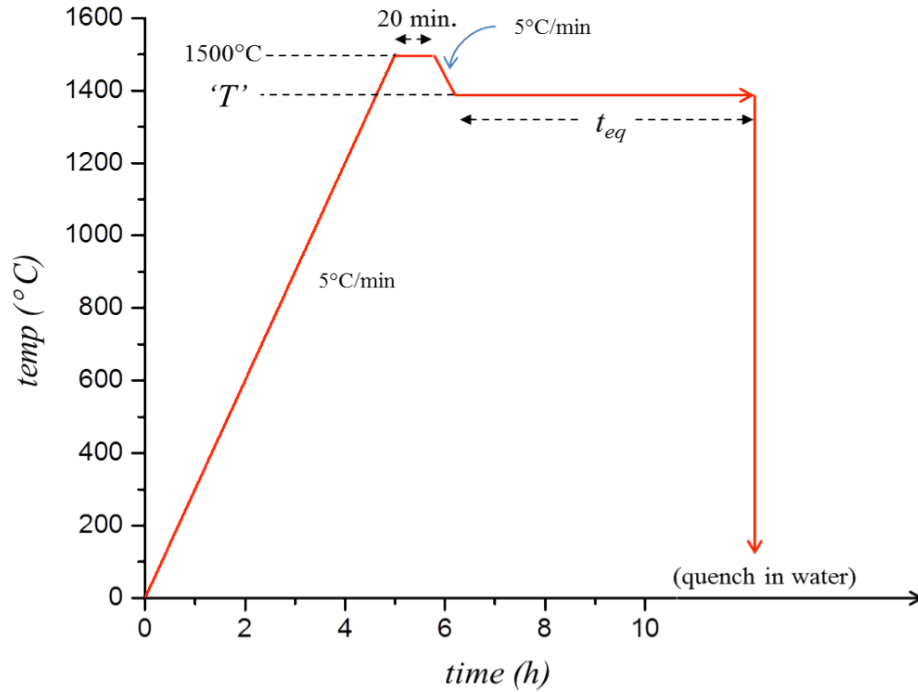


Figure IV-2. Heat cycle used for quenching experiments.

### A.3. Phase analysis

Quenched samples were crushed and characterized using XRD for phase identification. Diffraction patterns were collected from powder samples over  $10 - 70^\circ 2\theta$ , at a rate of  $0.02^\circ$  per second. Relative amounts of different phases were determined using quantitative analysis. For quantitative phase analysis, the TOPAS 4.2 (Bruker AXS, Karlsruhe, Germany) software package was used. The relative amounts of phases were determined by generating calculated XRD patterns using Rietveld quantitative phase analysis together with the PDF-4+ (2013) structural database for crystallographic information. To obtain the best-fit to the experimental pattern, appropriate Crystallographic Information Files (CIF) were taken from PDF-4+ database and Rietveld structural refinement of different corresponding phases was performed.

Quenched samples were also characterized using electron microscopy to complement the XRD results. The composition and phase assemblage was investigated using SEM-EDS/WDS.

#### **A.4. In-situ High Temperature XRD studies**

In-situ melting and solidification behavior of CAF-MP was studied using high-temperature XRD (HTXRD) measurements. In-situ HTXRD was carried out using a diffractometer (Siemens  $\theta$ - $\theta$  D5000) equipped with a custom built high-temperature furnace using  $\text{CoK}\alpha$  radiation. For the measurements, a thin, uniform layer of pre-reacted CAF-MP powder on a flat Pt disc was heated to 1500°C and cooled to room temperature. Diffraction patterns were collected at periodic isothermal temperature steps during the heating and cooling cycles, in the scan range 20-60° 2 $\theta$ , with step size 0.037° and a dwell time of 1s at each step.

## **B. Results and Discussions**

### **B.1. Viscosity measurements**

The behavior of the viscometer during the measurements was not consistent with a homogenous Newtonian liquid. The torque values increased and decreased sporadically and were accompanied by visible locking and slipping of the viscometer spindle. This effect was accentuated at lower temperatures and is indicative of a crystal phase coexisting in equilibrium with the melt at high temperatures. The effect of crystallization on the measured viscosity is difficult to predict but, it is not equal to the true viscosity of the melt. It depends on the crystallization process and the stoichiometry of the crystals.<sup>76</sup> However, once crystals impinge, the apparent viscosity will increase due to blocking or interlocking effects and eventually, flow will cease as the sample becomes fully crystalline. Indeed, this type of behavior was observed. Although the nature of the melt-crystal composition is unknown, the viscosity behavior appeared reversible in the time span of the measurement as evidenced by the data taken upon re-heating. Figure IV-3 shows viscosity (in Poise) versus 1/temperature (in K) for the CAF-MP composition. The plot shows a rapid increase in viscosity as a function of temperature at approximately

1480°C. It is unknown at what temperature the system is fully melted because the liquidus temperature of the system was not determined.

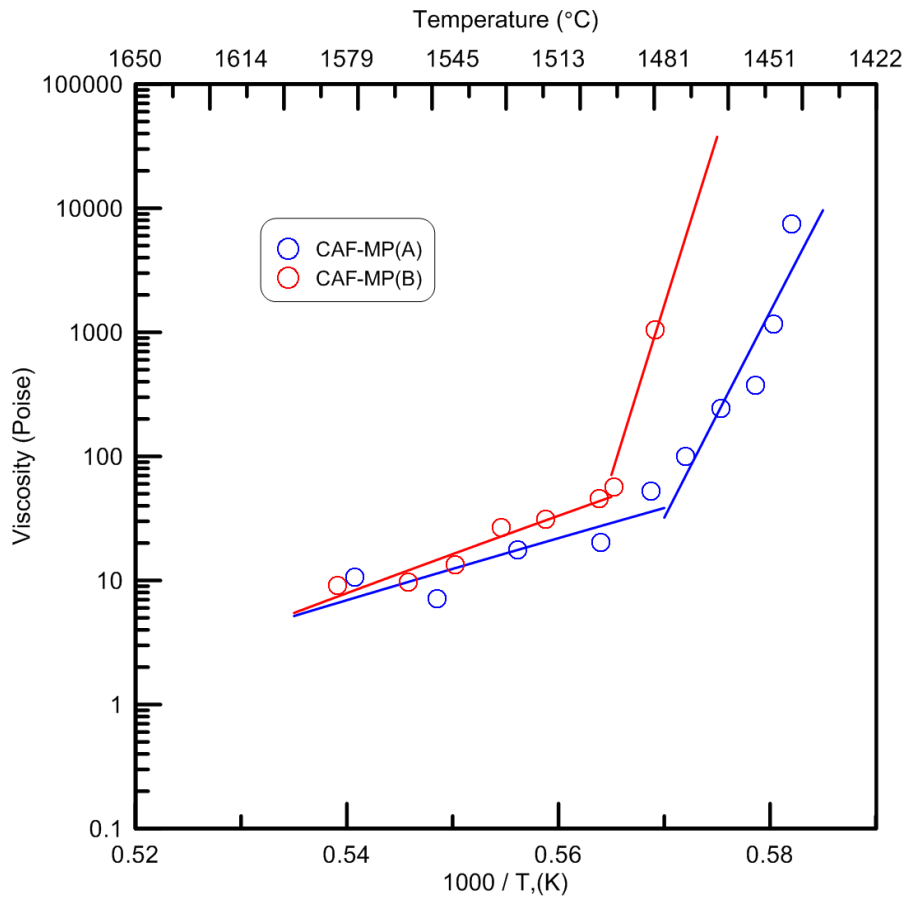


Figure IV-3. Viscosity as a function of temperature for CAF-MP. The accuracy of individual viscosity values is +/- 20% based on historical data for a reference material measured on the same instrument. The lines through the data are linear fits to aid the eye.

## B.2. DSC measurements and quenching experiments

Figure IV-4 shows the DSC curves corresponding to 20 K/min and 5 K/min heating/cooling rates. Exothermic peaks between 1280°C and 1330°C were consistently observed during cooling of raw material and pre-reacted material from the melt temperature. At higher cooling rates, a single broad peak was observed, as might be expected in case of rapidly cooled samples in which the DSC signal from individual phase evolution was convoluted into a single event. The DSC results are supporting evidence for the coexistence of crystalline phases within a melt of this system.

Quenching experiments were designed based on the exothermic peak temperatures from the DSC curves, believed to be related crystallization events. Varying heat treatment times ( $t_{eq}$ ) were investigated to understand phase evolution kinetics qualitatively. A baseline sample for comparison was heated to 1500°C, held for 4 h, and quenched. Table II-1 summarizes the temperatures ' $T$ ' and corresponding dwell times ' $t_{eq}$ ' used for quenching experiments.

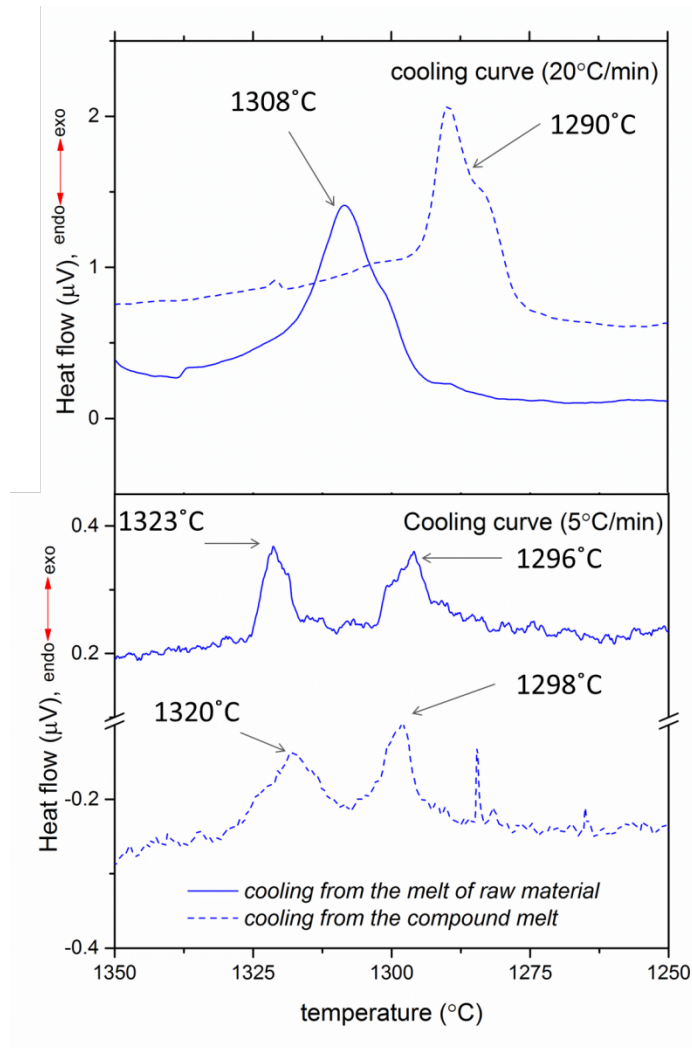


Figure IV-4. DSC curves showing exothermic peaks between 1280°C and 1330°C. The sharp peak on the dotted line (5 K/min) around 1287°C is an external fluctuation.

Table IV-1. Temperature Parameters Used for Quenching Experiments

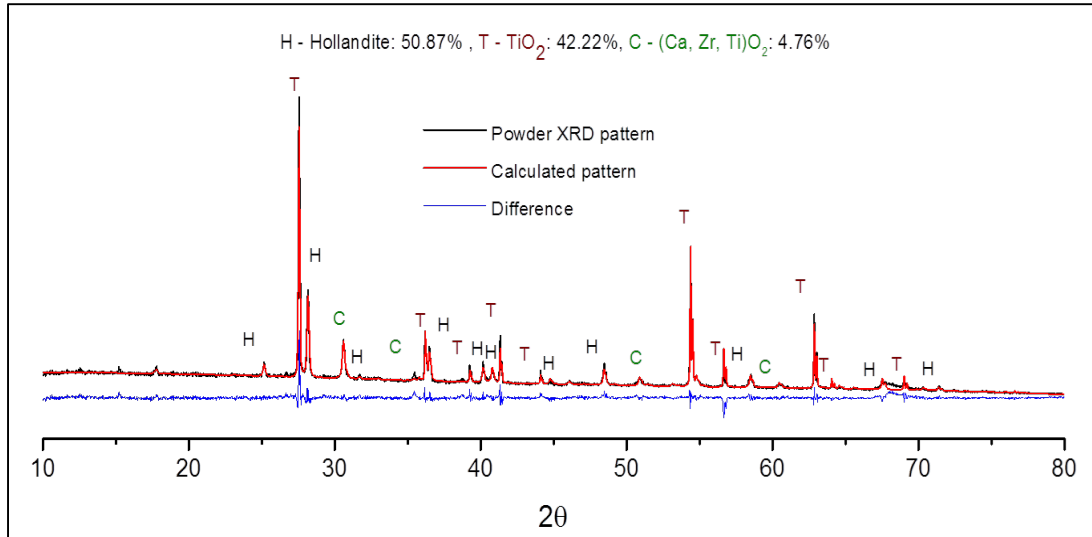
$T_m$	'T'	$t_{eq}$ (h)		
1500°C	1500°C	4		
1500°C	1325°C	1	12	24
1500°C	1285°C	1	12	24

### B.3. Phase analysis and microstructural characterization

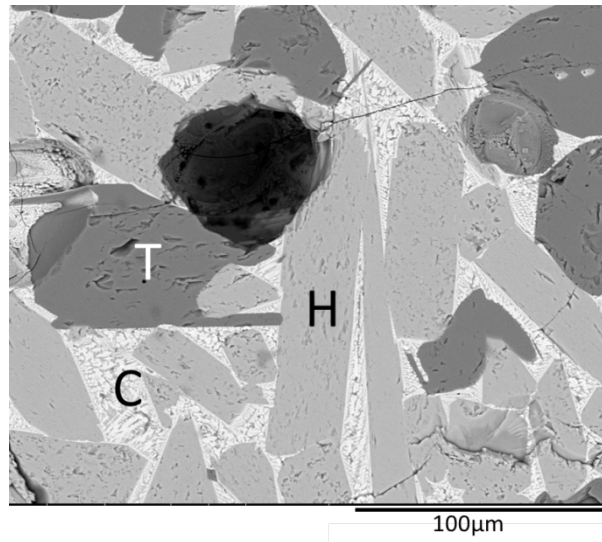
All quenched samples, after heat treatment, were found to wet the Pt foil, indicating that melting occurred during their respective thermal histories. The baseline sample quenched from 1500°C was fully crystalline, as confirmed by XRD. Figure IV-5a compares the baseline measured XRD pattern to a calculated pattern using Rietveld quantitative phase analyses based on the following phases: TiO<sub>2</sub> (PDF: 04-006-3570), hollandite (PDF: 04-013-6380), and tazheranite (PDF: 04-008-0260). During XRD phase analyses, it was observed that many phases in the CaO-ZrO<sub>2</sub>-TiO<sub>2</sub> system were close but not exact matches to the measured XRD patterns. Tazheranite ((Ca,Zr,Ti)O<sub>2</sub>) is a naturally occurring cubic ZrO<sub>2</sub> where Zr<sup>4+</sup> is partially substituted by Ca<sup>2+</sup> and Ti<sup>4+</sup> ions.<sup>77,78</sup> Pure ZrO<sub>2</sub>, naturally occurring as baddeleyite, has monoclinic symmetry but transforms to tetragonal symmetry at 1170°C and to cubic symmetry at 2370°C.<sup>78</sup> Cubic ZrO<sub>2</sub> with a fluorite-type structure can be stabilized at lower temperatures by the addition of tetravalent cations,<sup>79</sup> trivalent rare-earth oxides, or divalent cations like Ca<sup>2+</sup>.<sup>80</sup> In addition to these, a number of other phases with similar structural motifs – calzirtite (Ca<sub>2</sub>Zr<sub>5</sub>Ti<sub>2</sub>O<sub>16</sub>), zirconolite (CaZrTi<sub>2</sub>O<sub>7</sub>), perovskite (CaTiO<sub>3</sub>/CaZrO<sub>3</sub>) – that are stable at temperatures greater than 1200°C have been reported.<sup>33,81</sup> Precise identification of zirconolite or related structures becomes challenging during crystallization of multiphase melts given that a wide range of elements can form solid solutions with different phases in the CaO-ZrO<sub>2</sub>-TiO<sub>2</sub> system. Therefore, the chemistry of each phase in the X-ray Rietveld analysis was defined where possible using the elemental analysis results from

microscopy. The peaks indexed as tazheranite (Figure IV-5a) could correspond to several phase(s) in the  $\text{CaO-ZrO}_2\text{-TiO}_2$  system and hereafter is referred to as “Ca-Zr-Ti-O”.

Figure IV-5b shows a representative microstructure of the sample quenched from  $1500^\circ\text{C}$ . In that image, the darkest gray phase corresponds to rutile (R), the mid-tone gray phase corresponds to hollandite (H) and is characterized by its large aspect ratio, and the brightest color phase corresponds to Ca-Zr-Ti-O (C). WDS elemental mapping images for selected elements are shown in Figure IV-6. The elemental maps show distinct partitioning of hollandite specific elements (Ba, Cr, and Cs) and a Ti rich phase that was presumably  $\text{TiO}_2$ .



(a)



(b)

Figure IV-5. (a) Quantitative XRD analysis of CAF-MP quenched from 1500°C and held for 4h. Best fit for Rietveld pattern refinement was obtained with hollandite (H), TiO<sub>2</sub> (T) and tazheranite (C) (b) Corresponding back-scattered image.

A distinct feature observed in the hollandite phase was a compositional gradient of Cr and Fe across the grains, as can be seen by comparing Cr and Fe elemental maps in Figure IV-6. This phenomenon was observed in samples heat treated at 1325 and 1285°C as well and is believed to be indicative of a fractional crystallization process, which will be discussed later in Section A.4. Preferential partitioning of Nd, Zr, Ca, and Zr to the bright Ca-Zr-Ti-O phase was also observed in Figure IV-6. The corresponding diffraction peaks in Figure IV-5a match with multiple structures such as cubic ZrO<sub>2</sub>, ZrTiO<sub>4</sub>, zirconolite etc. in the CaO-ZrO<sub>2</sub>-TiO<sub>2</sub> system that can host any of the observed elements in their respective lattices.

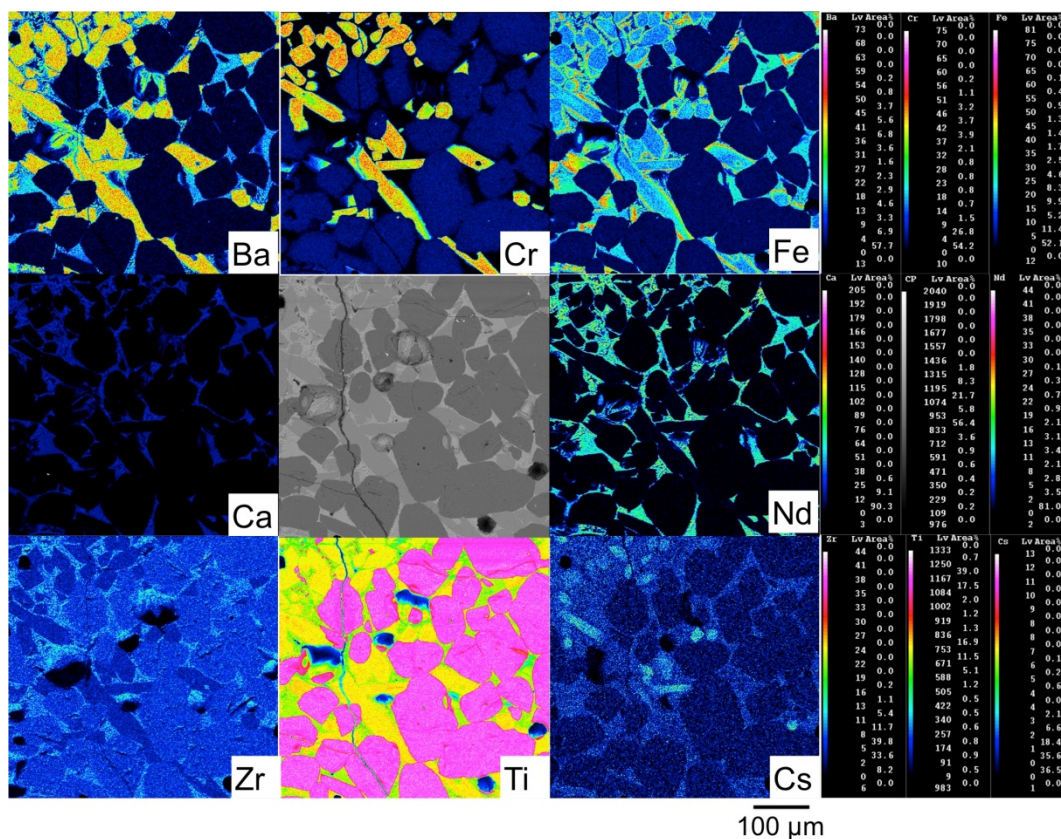


Figure IV-6. WDS maps of selected elements of CAF-MP at 1500°C annealed for 4 h. Different phases are labelled on the BSE graphic - hollandite (H) and TiO<sub>2</sub> (T). The brightest background phase is Ca-Zr-Ti-O.

Figure IV-7 summarizes the XRD and SEM results for the samples heat treated at 1325°C for 1h, 12h, and 24h. Figure IV-7a shows the quantitative Rietveld refinement results based on the following phases: TiO<sub>2</sub> (PDF: 04-006-3570), hollandite (PDF: 04-013-6380), tazheranite (PDF: 04-008-0260), perovskite (PDF: 04-014-7761), and zirconolite (PDF: 04-002-4312). The same phases (hollandite, rutile, and Ca-Zr-Ti-O) observed in the sample quenched directly from 1500°C were also observed in the sample annealed at 1325°C. In addition, a perovskite and a Zr-rich phase, separate from the Ca-Zr-Ti-O phase, were identified. The perovskite phase was identified in all samples whereas the Zr-rich phase was identified in samples annealed for longer times (12h and 24h) as evidenced by the best fit to the experimental pattern when both tazheranite and zirconolite were assumed to be in the system. This suggests zirconolite is the Zr-rich

phase evolving from Ca-Zr-Ti-O. However, the specific chemistry of these phases remains unknown.

BSE contrast images presented in Figure IV-7b support the XRD results and show at least 4 distinct phases in the sample annealed for 24h. WDS mapping images of selected elements in this sample are shown in Figure IV-8. Rutile (R) is indicated as the darkest gray phase in Figure IV-7b. The mid-tone gray phase in Figure IV-7b identified as hollandite (H) had the target chemistry (Ba, Cr, Fe, Ti and Cs) based on Figure IV-8. Importantly, Cs remained incorporated within the hollandite phase after annealing for 24h, indicating thermal stability of the hollandite phase with respect to Cs retention. Two distinct phases, apart from hollandite and  $\text{TiO}_2$ , could be observed in the BSE image of the sample corresponding to  $t_{\text{eq}} = 24\text{h}$ . WDS maps show that both these regions exhibited uniform Ti distribution, as would be expected in both perovskite and zirconolite structures. Ca is present in both phases, but more concentrated in the brightest phase, which is also consistent with perovskite and zirconolite structures. This is further supported by the elemental map showing Nd-rich areas in the brightest phase. The light gray phase is rich in Zr and Ca, which is consistent with a zirconolite phase.

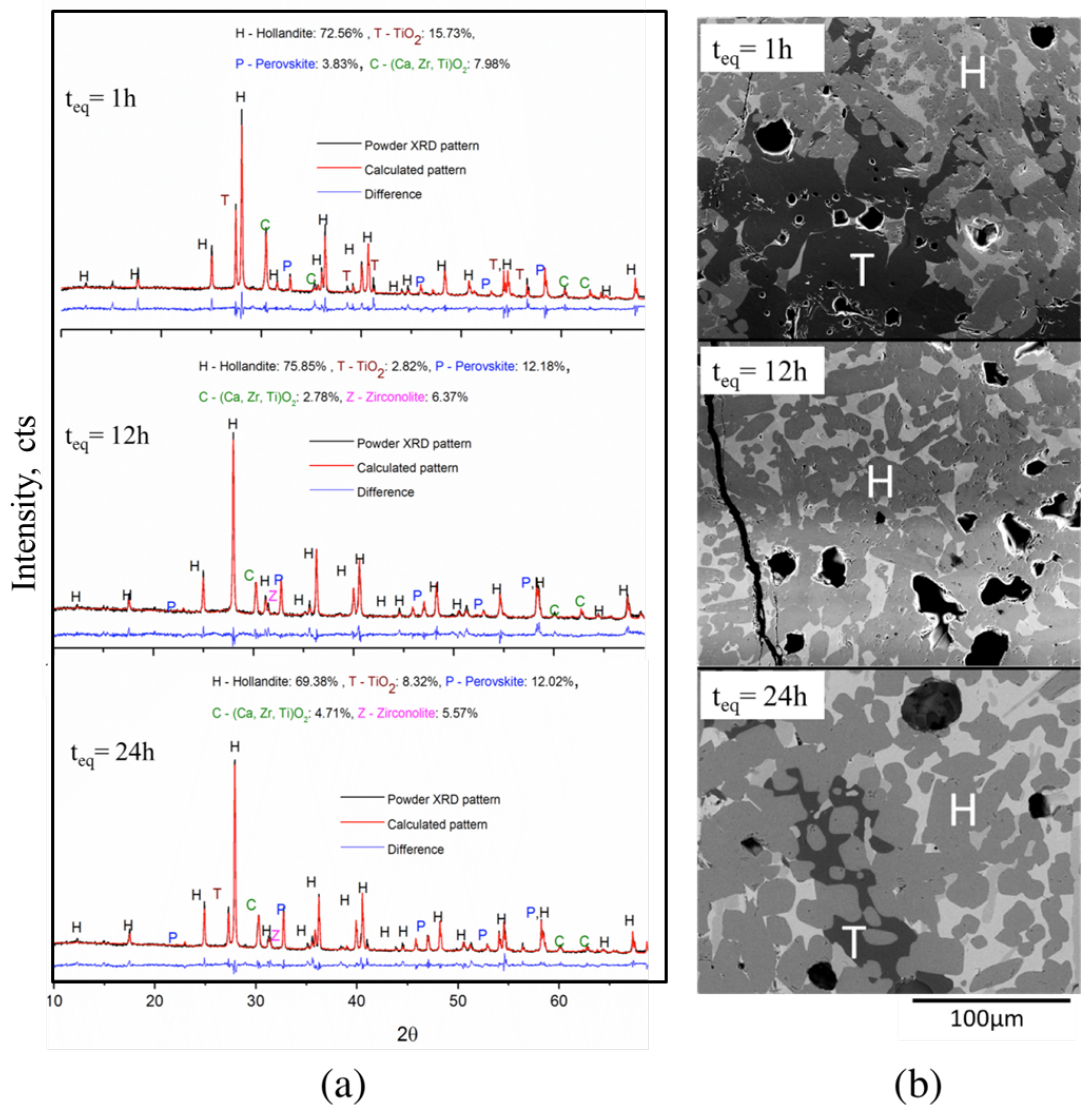


Figure IV-7. (a) Quantitative XRD analysis of CAF-MP quenched from 1325°C held for varying times. Best fit for Rietveld pattern refinement was obtained with hollandite (H), TiO<sub>2</sub> (T), tazheranite (C) and zirconolite (Z) (b) Corresponding back-scattered images.



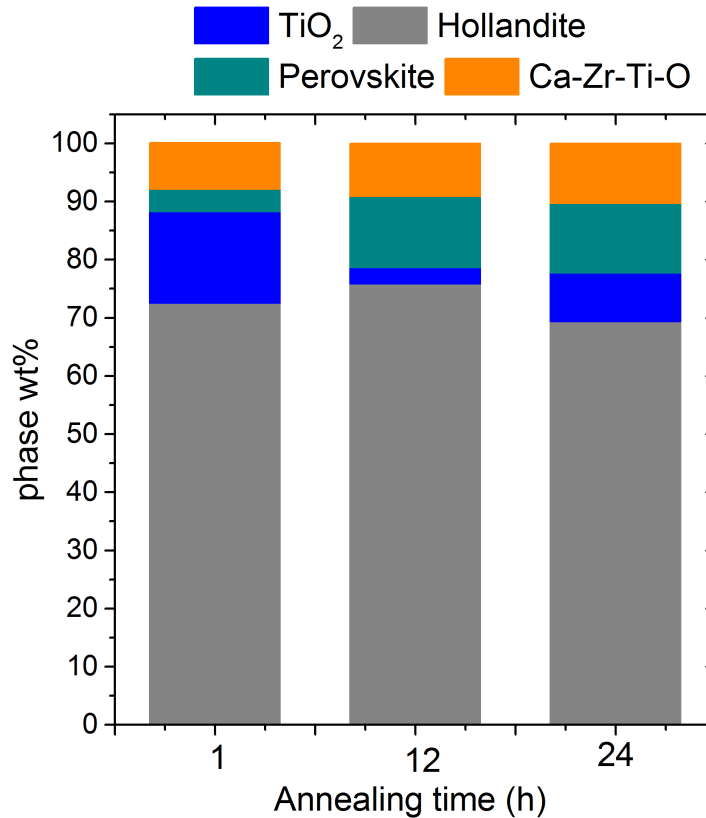


Figure IV-9. Quantitative phase distribution as a function of annealing time at 1325°C. Ca-Zr-Ti-O represents both tazheranite and zirconolite phases from Rietveld refinement.

Figure IV-10 summarizes the XRD and SEM results for the samples heat treated at 1285°C for 1h, 12h, and 24h. Figure IV-11 shows the elemental distribution in the sample treated for 24h at 1285°C. Figure IV-10a compares the measured XRD patterns to calculated patterns using Rietveld quantitative phase analyses based on the following phases: TiO<sub>2</sub> (PDF: 04-006-3570), hollandite (PDF: 04-013-6380), tazheranite (PDF: 04-008-0260), perovskite (PDF: 04-014-7761), and zirconolite (PDF: 04-002-4312). XRD phase analysis and BSE images (Figure IV-10) of different samples, annealed at 1285°C for different holding times and quenched, show similar phase assemblage and evolution as observed at 1325°C. Perovskite and Zr-rich phase were present in all samples that were annealed for varying times. The Zr-rich phase that was observed in the sample treated at 1325°C for longer times was seen at 1285°C even after 1h. A chart showing the percentage of each phase as a function of annealing time is shown in Figure IV-12.

Significant differences in phase abundance were measured in samples annealed for 1h compared to 12h or 24h indicating that at 1285°C, the kinetics of phase evolution and development was relatively slow as well, on the order of hours.

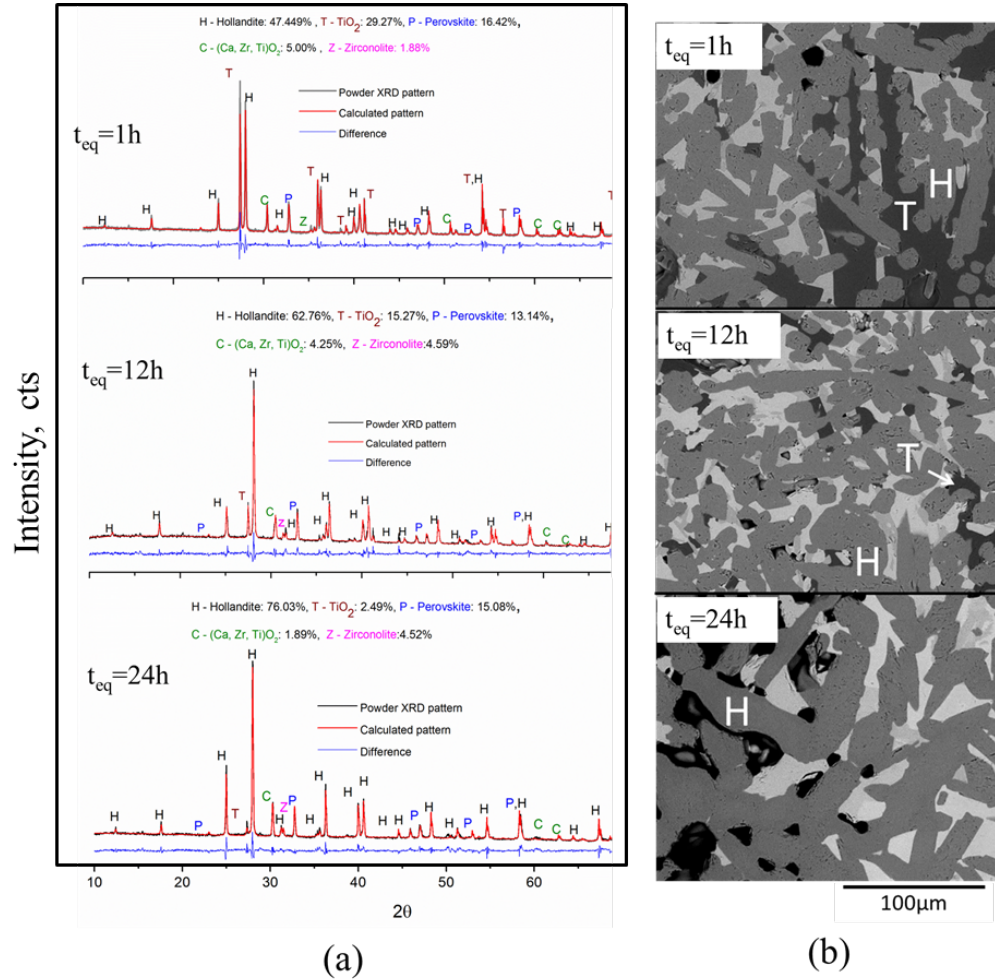


Figure IV-10. (a) Quantitative XRD analysis of CAF-MP quenched from 1285°C held for varying times. Best fit for Rietveld pattern refinement was obtained with hollandite (H),  $TiO_2$  (T), tazheranite (C) and zirconolite (Z) (b) Corresponding back-scattered images.

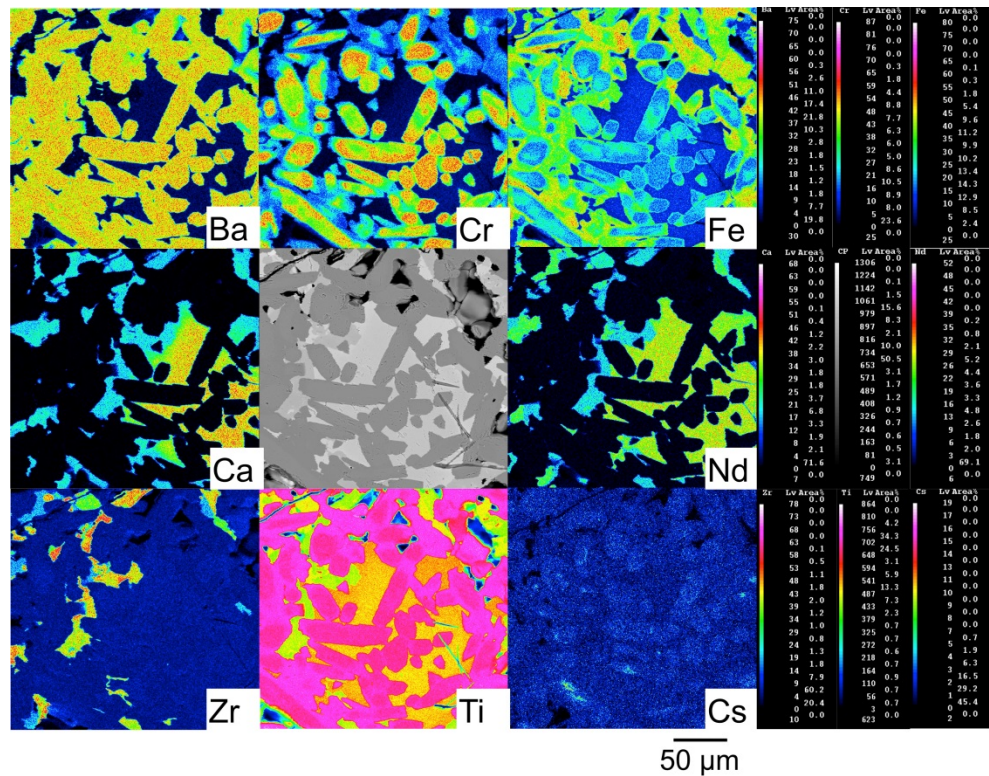


Figure IV-11. WDS maps of selected elements of CAF-MP at 1285°C annealed for 24 h. Multiple sweeps were run across the selected area to collect data for the maps. (Here also, a shift in the scanned area occurred between different sweeps, as observed through a few of the elemental maps).

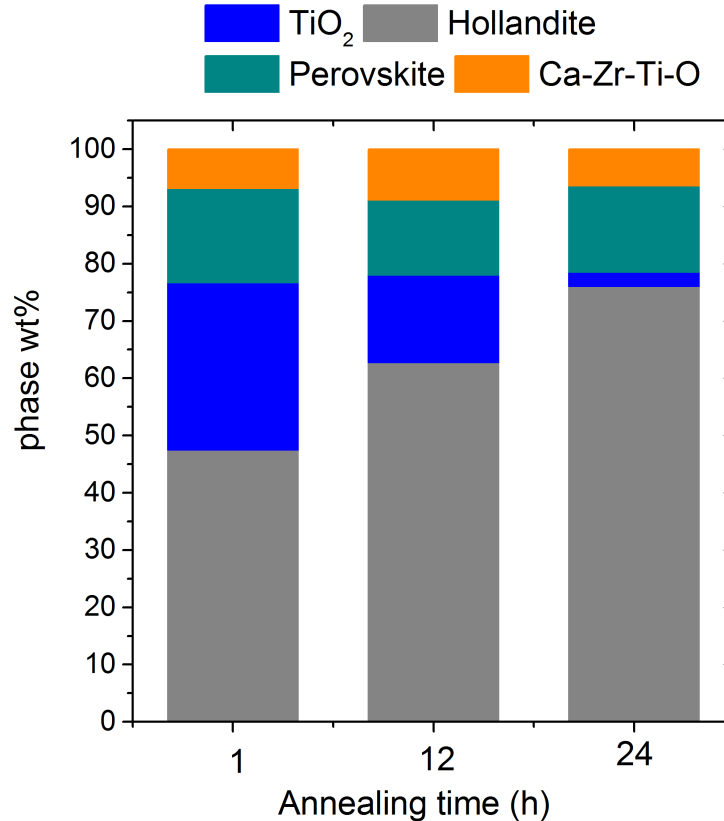


Figure IV-12. Quantitative phase distribution as a function of annealing time at 1285°C. Ca-Zr-Ti-O represents both tazheranite and zirconolite phases from Rietveld refinement.

Greater understanding of the crystallization behavior of melt processed Synroc-based ceramics can be made by comparing the phase and microstructural analysis of samples heat treated at 1285, 1325, and 1500°C. With respect to phase evolution, the kinetics was time dependent at both temperatures but the type was not. For samples heat treated at 1325°C, the hollandite phase concentration remained relatively constant over 24h, whereas the perovskite and Ca-Zr-Ti-O concentrations increased over time. An opposite trend was observed in samples heat treated at 1285°C; the perovskite and Ca-Zr-Ti-O concentrations remained relatively constant over 24h, whereas the hollandite concentration increased with time. In both cases, the amount of TiO<sub>2</sub> relative to the primary phases (hollandite, perovskite, and Ca-Zr-Ti-O) was greater at shorter times (1h) than longer times (24h). TiO<sub>2</sub> was the primary constituent of all the phases in the system and it follows that available TiO<sub>2</sub> would be used during crystal growth of all the primary

phases. However, the concentration of  $\text{TiO}_2$  with time was not consistent for both temperatures. Although  $\text{TiO}_2$  concentration decreased with time for samples cooled to  $1285^\circ\text{C}$ , that trend was not observed for samples cooled to  $1325^\circ\text{C}$ .

Distinct compositional gradients of Cr and Fe across the phases associated with hollandite are visually apparent in the elemental maps in Figure IV-6, Figure IV-8 and Figure IV-11. High concentration of Fe along the edges of hollandite grains, accompanied by a decrease in Cr intensity towards the edges, can be seen. This phenomenon was more pronounced in samples quenched from lower temperatures (i.e.  $1285^\circ\text{C} > 1325^\circ\text{C} > 1500^\circ\text{C}$ ). Collectively, these results indicate different crystal growth temperature regimes for the different phases, indicating that crystallization sequences (or growth regimes) are dependent on other factors such as the composition of any residual melt or heterogeneous nucleation sources.

In general, the observed behavior resembles fractional crystallization such as reported during the solidification of zirconolite melts.<sup>82</sup> In that research, the crystallization sequence for zirconolite ( $\text{CaZrTi}_2\text{O}_7$ ) was reportedly  $\text{Ti-bearing ZrO}_2 \rightarrow \text{ZrTiO}_4 \rightarrow \text{Zr-rich CaZrTi}_2\text{O}_7 \rightarrow \text{Zr-poor CaZrTi}_2\text{O}_7$ . The phases formed early at higher temperatures reacted with the residual melt to produce Zr- and Ti- rich phases surrounding each previously formed phase. The composition of the phases was correlated to the enrichment or depletion of Zr and Ti in the residual liquid phase expressed by peritectic/eutectic points in a pseudo-binary system.<sup>82</sup> Further explanation of the phase evolution behavior in the CAF-MP system is presented in the following section.

#### **B.4. High-Temperature X-Ray Diffraction**

In-situ XRD patterns collected during heating and cooling of CAF-MP are shown in Figure IV-13 Figure IV-14, respectively. A baseline diffraction pattern was taken at  $25^\circ\text{C}$ , before the start of the heating cycle, to confirm the phase composition of the starting material. As shown in Figure IV-13, the primary starting materials, (e.g.  $\text{TiO}_2$ ,  $\text{BaCO}_3$ ,  $\text{ZrO}_2$ ,  $\text{Cs}_2\text{O}_3$ , etc.) were identified. Initial indications of reaction observed in the  $800^\circ\text{C}$  XRD pattern could first be identified in the  $900^\circ\text{C}$  XRD patterns matching with hollandite and perovskite phases. The peak intensities associated with hollandite and perovskite phases grew with increasing temperature, accompanied by decreasing peak intensities of phases identified in the baseline pattern, which is typical of a solid-state

reaction process. Initial indications of a liquid phase were observed in the 1400°C XRD pattern as evidenced by an amorphous hump between 40 - 60° 2θ and a decrease in the peak intensities of the perovskite phase from lower temperatures. At 1500°C, the XRD pattern indicated an amorphous phase in combination with the hollandite phase and no indication of secondary crystalline phases. Taken together, the XRD scans from 700°C to 1500°C confirm the initial reaction of the pre-cursor powders, the subsequent formation and in-growth of crystalline phases (i.e. hollandite and perovskite), and eventual partial melting of the system by dissolution of the all crystalline phases except the hollandite phase, which remains in combination with a liquid phase at temperatures up to at least 1500°C, the highest temperature studied.

The XRD pattern at 1500°C shown in Figure IV-13 is the baseline pattern for the subsequent cooling cycle. That pattern is reproduced again in Figure IV-14, in which hollandite and an amorphous (liquid) phase are evident. Upon cooling, hollandite in-grew and remained the only crystalline phase as evidenced by the 1500 – 1400°C XRD patterns. Peaks identified as belonging to perovskite and Ca-Zr-Ti-O phases appeared in the 1350°C XRD pattern. No measureable amorphous (liquid) phase was identified in the 1350°C XRD pattern indicating the crystalline phases that appeared at 1350°C precipitated from the liquid. A set of minor peaks was observed in the XRD patterns at temperatures less than 1350°C, which are attributed to TiO<sub>2</sub>. This result indicates that TiO<sub>2</sub> identified in fully cooled samples precipitated upon cooling, which is known to occur in zirconolite systems.<sup>80</sup> A comparison of the HTXRD scans from 1500°C to that from 1100°C confirms that at 1500°C the system consists of a partial melt with a hollandite phase, and that upon cooling, hollandite continues to in-grow followed by the eventual formation of perovskite and Ca-Zr-Ti-O phases (accompanied by disappearance of the liquid phase) at ~1350°C. Minor amounts of TiO<sub>2</sub> precipitate at ~ 1300°C and further cooling does not result in any significant phase evolution observable by the XRD patterns, indicating complete crystallization.

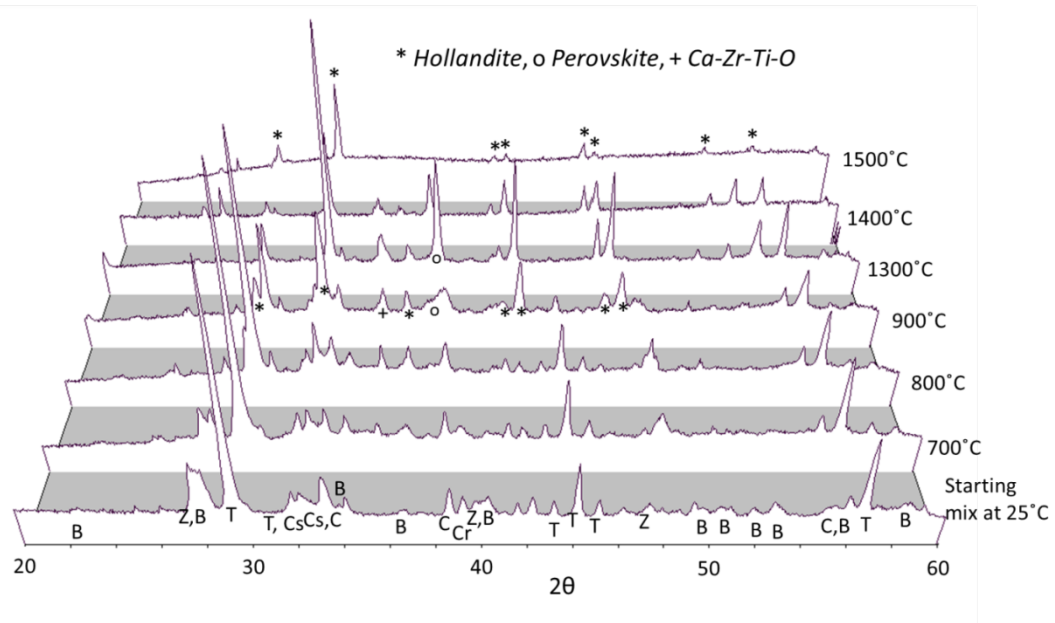


Figure IV-13. In-situ XRD patterns collected at different temperatures during heating from 25°C to 1500°C. Different phases in the starting material are B-BaCO<sub>3</sub>, Z-ZrO<sub>2</sub>, T-TiO<sub>2</sub> (anatase), Cs-Cs<sub>2</sub>CO<sub>3</sub>, C-CeO<sub>2</sub>, Cr-Cr<sub>2</sub>O<sub>3</sub>.

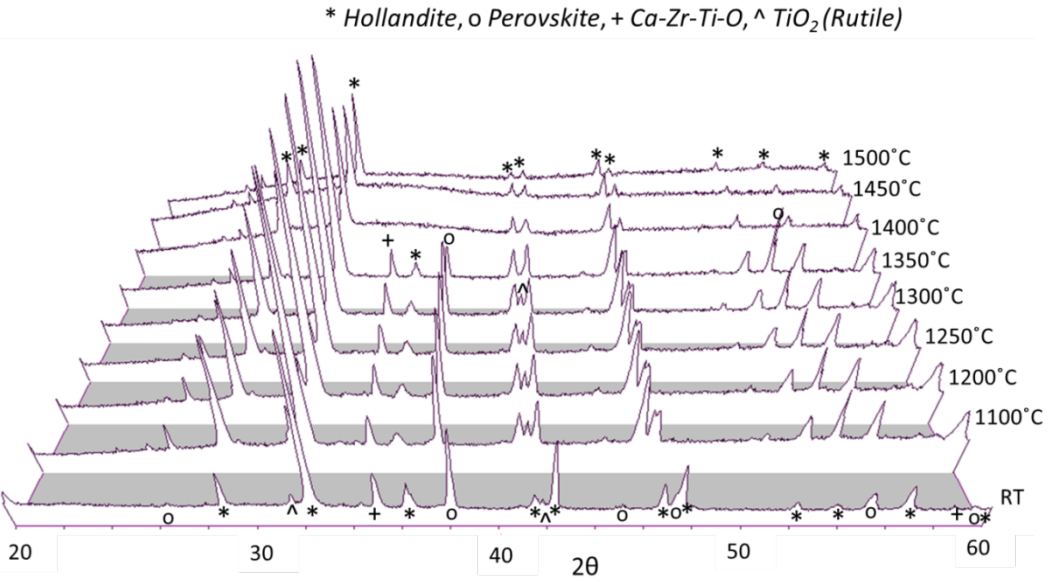


Figure IV-14. In-situ XRD patterns collected during cooling from 1500°C to room temperature (RT).

Phase evolution behavior identified from HTXRD further advances our understanding of the trend of relative phase amounts shown in Figure IV-9 and Figure IV-12. At 1325°C after 1h, the sample quenched was crystallized to be predominantly hollandite and the other phases being perovskite, Ca-Zr-Ti-O and TiO<sub>2</sub>. The relatively high amount of TiO<sub>2</sub> observed in the sample quenched from 1285°C after 1h as compared to 1325°C after 1h can be attributed to the precipitation of TiO<sub>2</sub> at lower temperatures (~1300°C). Upon annealing, the system progresses towards equilibrium resulting in relative growth or reduction of different phases as discussed earlier.

### **C. Conclusion**

Our results demonstrate that the multiphase ceramic system is not a homogeneous melt at 1500°C but instead consists of nominally stoichiometric hollandite with a melt comprised of the remaining constituents. As the material is cooled, a Zr-rich phase that evolves further into zirconolite and a mixed Ca-lanthanide series perovskite phase forms. XRD and microstructural analysis of quenched samples suggest that the identified DSC peaks correspond to crystallization of perovskite (~1325°C) and zirconolite (~1285°C). Both zirconolite and perovskite phases are observed in samples quenched from either 1285 and 1325°C after holding for >12h. However, zirconolite has not been observed in the sample quenched from 1325°C after 1h, suggesting perovskite precedes zirconolite crystallization upon cooling. Collectively, the data indicates the order of phase evolution upon cooling in this system is hollandite → perovskite → zirconolite → TiO<sub>2</sub>. A wide range of substitutions is possible (and expected) in both phases and was observed in the WDS maps. Parasitic phases incorporating other elements were not identified. An observed partitioning of Cr and Fe species within the hollandite phase needs to be further examined.

## PHASE EVOLUTION STUDIES OF $\text{Ba}_{1.0}\text{Cs}_{0.3}\text{M}_{2.3}\text{Ti}_{5.7}\text{O}_{16}$ ( $M = \text{Al}, \text{Cr}, \text{Fe}$ ) HOLLANDITES

Based on the general formulation of hollandite  $[\text{Ba}_x\text{Cs}_y][\text{M}^{3+}_{2x+y}\text{Ti}^{4+}_{8-2x-y}\text{O}_{16}]$  (Section II) and the single-phase domain for phase-purity of hollandites (Table II-2), the composition  $\text{Ba}_{1.15}\text{Cs}_{0.3}\text{M}^{3+}_{2.3}\text{Ti}_{5.7}\text{O}_{16}$  was selected. A series of hollandites with differing chemistries,  $M = \text{Al}, \text{Cr}$  and  $\text{Fe}$ , were prepared by melt-processing, as mentioned in Section I.B.1, and compared for the ease of hollandite phase formation. The purpose of the study is to evaluate the effects of different trivalent cations ( $\text{M}^{3+}$ ) on hollandite phase formation during melt-processing. In-situ XRD measurements were collected during a simulated melt-processing heat cycle and phase evolution as a function of temperature was studied for each of the compositions.

### A. Experimental

Phase evolution of hollandite was studied using high-temperature XRD. The starting material – stoichiometric mixture of corresponding oxides/carbonates – was heated at the rate of 5K/min, to simulate the conditions used for melt-processing, and the diffraction data was collected at an interval of 50°C, over a temperature range of 800 – 1350°C.

### B. Phase Analysis

XRD data of different single-phase hollandites is shown in Figure V-1.  $\text{Ba}_{1.15}\text{Cs}_{0.3}\text{M}^{3+}_{2.3}\text{Ti}_{5.7}\text{O}_{16}$  hollandites with  $M = \text{Al}, \text{Cr}$  and  $\text{Fe}$  are further represented in this section as Al-SP, Cr-SP and Fe-SP respectively. Pure hollandite is formed with no secondary phases in Fe-SP and Cr-SP. However, multiple trials of melting Al-SP showed that a secondary phase,  $\text{Al}_2\text{TiO}_5$  was always retained in the final reacted material.

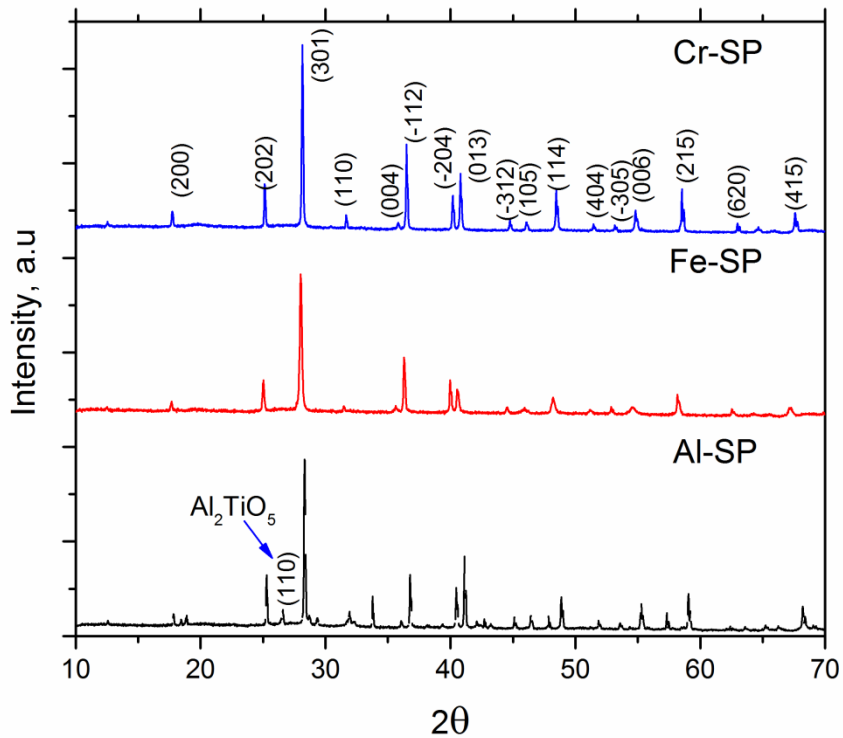


Figure V-1. XRD patterns of different single-phase hollandites.

### C. Visual Examination and Microstructure

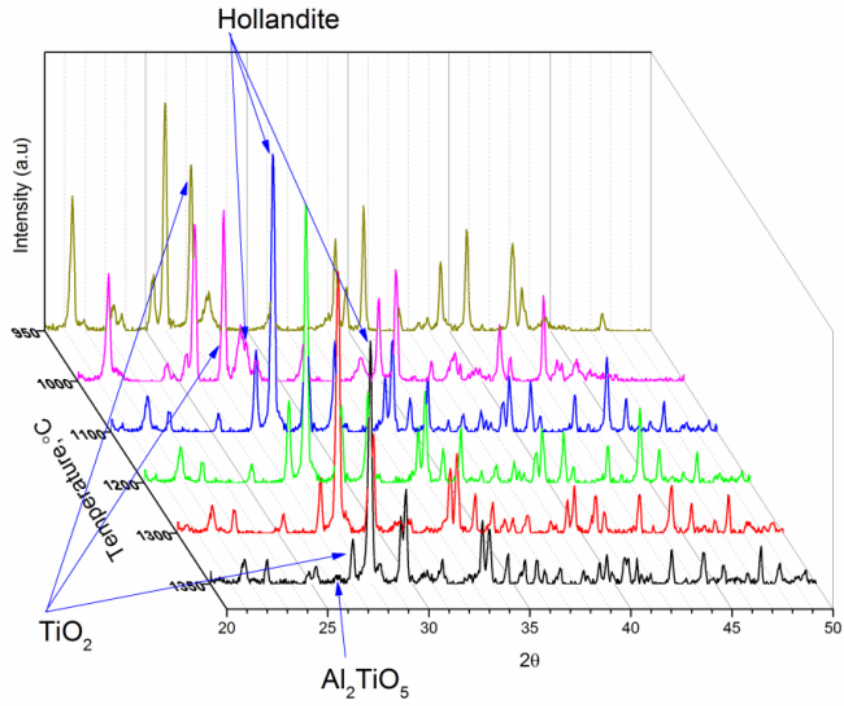
Visual examination of the reacted materials shows that the Cr-SP did not fully melt, although the reaction was complete. Since  $\text{Cr}_2\text{O}_3$  is a highly refractory material, melting is expected to occur at relatively higher temperatures and at the same time is expected to assist in the formation of hollandite.<sup>3</sup> Visual examination of Fe-SP revealed that it melted fully. Fe-SP melt reacted with  $\text{Al}_2\text{O}_3$  crucible and could not be separated from the crucible, whereas there was little reaction between Cr-SP and the crucible, and it could be separated from the crucible surface. Figure V-2 compares the images of these two hollandites formed.



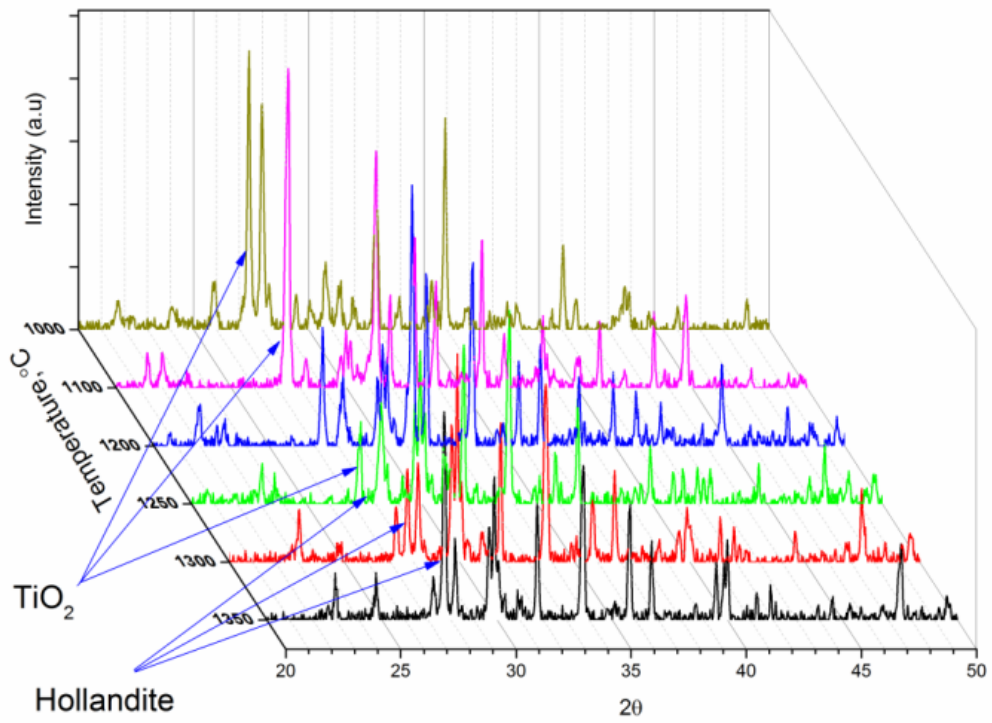
Figure V-2. As-melt samples of Fe-SP and Cr-SP.

#### D. Hollandite Phase Evolution

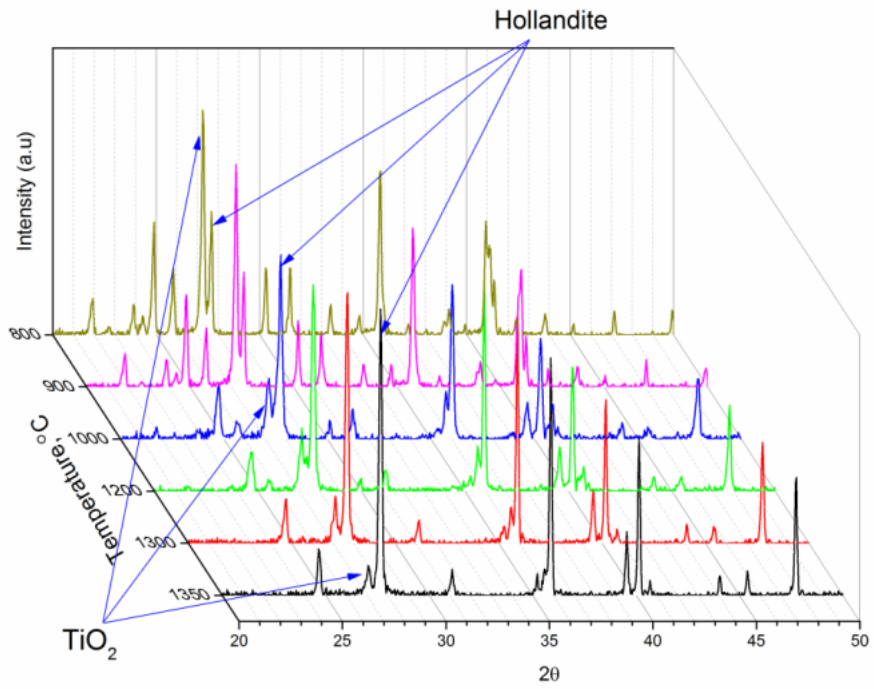
HTXRD data was collected on single-phase hollandites over the temperature range 800 - 1350°C to understand the effects of different trivalent cations on the evolution of hollandite phase. Figure V-3 shows representative datasets for the phase changes in different systems. In Al-SP, Fig. V-3(a), initial formation of the hollandite phase was observed at 1000°C with the intensity of the major hollandite spectral line increased with temperature.  $\text{Al}_2\text{TiO}_5$ , the secondary phase in all melt trials, appeared at 1350°C, suggesting that it was stable at high temperature. In Fe-SP, hollandite was not observed until 1250°C, as indicated in Figure V-3b. HTXRD of Cr-SP has interesting features. Hollandite peaks were observed on all plots, starting from 800°C. The final diffraction peaks at 1350°C primarily correspond to hollandite and some unreacted  $\text{TiO}_2$ , indicating that the reaction was almost complete within the used heating cycle. Studying the plots at intermediate temperatures (1000 - 1200°C) indicates that barium titanates formed initially, as indicated in Figure V-4, which reacted at temperatures above 1200°C to form hollandites.



(a)



(b)



(c)

Figure V-3. HTXRD plots for (a) Al-SP (b) Fe-SP and (c) Cr-SP.

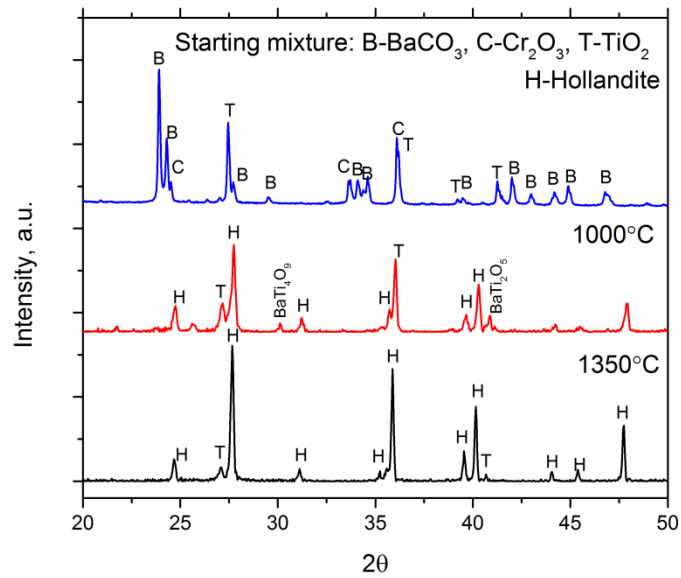


Figure V-4. Phase evolution in Cr-SP.

## **E. Conclusion**

Melt-processing and HTXRD studies of different single-phase hollandites show that  $\text{Cr}^{3+}$  stabilizes hollandite at lower temperatures and expedites its formation during melting. Cr-SP hollandite is highly refractory in nature and exhibited minimum bulk melting during the ‘melt-processing’ heat cycle used. This also explains the observation from Section IV that hollandite exists in crystalline state even at  $1500^\circ\text{C}$  – the temperature used for the melt-processing of multiphase compositions.

## STRUCTURAL CHARACTERISTICS OF PHASE-PURE $\text{Ba}_{1.15-x}\text{Cs}_{2x}\text{Cr}_{2.3}\text{Ti}_{5.7}\text{O}_{16}$ HOLLANDITES FOR Cs IMMOBILIZATION

The collective findings from Section V, along with the findings from a recent efforts at SRNL,<sup>50</sup> strongly indicate barium hollandites with  $\text{Cr}^{3+}$  as a promising lattice for effective Cs retention. This chapter focusses on the research related to the further analysis and validation of the selected composition  $\text{Ba}_x\text{Cr}^{3+}_{2x}\text{Ti}^{4+}_{8-2x}\text{O}_{16}$  as a suitable host lattice for effective Cs immobilization. For this study, we selected the composition,  $\text{Ba}_{1.15}\text{Cr}_{2.3}\text{Ti}_{5.7}\text{O}_{16}$ , within the domain of  $x$ : 1.12–1.34 that forms phase-pure hollandites (Table II-2), as the base composition. Series of compositions  $\text{Ba}_{1.15-x}\text{Cs}_{2x}\text{Cr}_{2.3}\text{Ti}_{5.7}\text{O}_{16}$  ( $0 \leq x \leq 1.15$ ) were prepared to determine the solubility of Cs and the effects of Cs substitution on Ba sites were examined. We present the structural analysis of Cs-substituted phase-pure hollandites including the modifications induced by Cs addition on octahedral framework and the characteristics of tunnel cations in this chapter.

### A. Characterization

Sintered pellets were crushed and ground using an agate mortar and pestle, and sieved (-200 mesh) for powder XRD measurements using a D8 Advance diffractometer (Bruker AXS, USA) equipped with  $\text{CuK}\alpha$  radiation (40kV, 40mA). Diffraction patterns were collected over the range  $10 - 140^\circ 2\theta$  using a Lynxeye linear position-sensitive detector. Structural analysis of phase-pure samples was also carried out using neutron diffraction measurements. Time-of-flight (TOF) neutron powder diffraction (NPD) experiments were performed at Oak Ridge National Laboratory (ORNL) using the POWGEN powder diffractometer at the Spallation Neutron Source (SNS). Powder samples were placed in vanadium cans of 6 mm diameter and TOF diffraction patterns were collected at 300 K with neutron center-wavelength,  $\lambda = 1.066 \text{ \AA}$  that covers reflections from the planes with d-spacing in the range  $0.28 - 5.26 \text{ \AA}$ .

Microstructures of the polished surfaces of sintered pellets were observed using a FEI™ Quanta 200 F SEM (FEI, Oregon, USA). The compositions of the powder samples

used for diffraction studies were measured using X-ray fluorescence (XRF) method using a S4 PIONEER - XRF Spectrometer (Bruker AXS, Karlsruhe, Germany). Electron-transparent samples for TEM analysis were prepared by crushing and suspending the sol-gel samples in ethanol. The suspension was dried on a Cu grid and SAED patterns were collected using F20 Tecnai (FEI, Hillsboro, USA) field emission TEM at an operating voltage of 200 kV.

To extract the structural features, Rietveld refinement of XRD and NPD data were carried out using TOPAS 4.2 (Bruker AXS, Karlsruhe, Germany) software package. Starting with the monoclinic (I2/m) structural model of  $\text{Ba}_{0.32}\text{Ti}_{1.36}\text{Fe}_{0.64}\text{O}_4$  (PDF: 04-010-2859),<sup>49</sup> powder XRD data was refined using TOPAS in GUI mode. Figure VI-1 shows a standard I2/m hollandite unit cell with one tunnel site for Ba/Cs (*A* site), two distinct crystallographic octahedral sites for Cr/Ti (M1 and M2) and four distinct oxygen sites (O1, O2, O3 and O4). Figure VI-2 shows the oxygen coordination of different cations. Typical XRD refinement procedures were performed as follows. A Chebyshev polynomial with 7 coefficients was used to describe the background and the peak profiles were described using a pseudo-Voigt function. Oxygen sites were assumed to have full occupancy and their atomic positions were not refined. The occupancies and positions of tunnel cation sites were refined first followed by octahedral sites. The sum of occupancies of Cr and Ti on each of the sites M1 and M2 (Figure VI-1) were constrained to unity. Finally, isotropic displacement parameters were refined for all cation sites.

For NPD refinement, appropriate executable input files that were run by TOPAS were created. The I2/m structural models generated from the XRD refinement were used as starting models. The background was described using a Chebyshev polynomial with 10 coefficients and the peak profiles using a pseudo-Voigt function. Occupancies/atomic positions were refined starting from strongest neutron scatterer to the weakest one. All oxygen sites were assumed to have full occupancy and are only refined for positions. Occupancies and positions of all cations were refined in a similar fashion to that of XRD refinement. While isotropic displacement parameters were used for Cr, Ti and O sites, anisotropic displacement parameters (ADPs) were used for the tunnel cations to account for any disorder in their locations since they are located along one-dimensional tunnels in the structure.

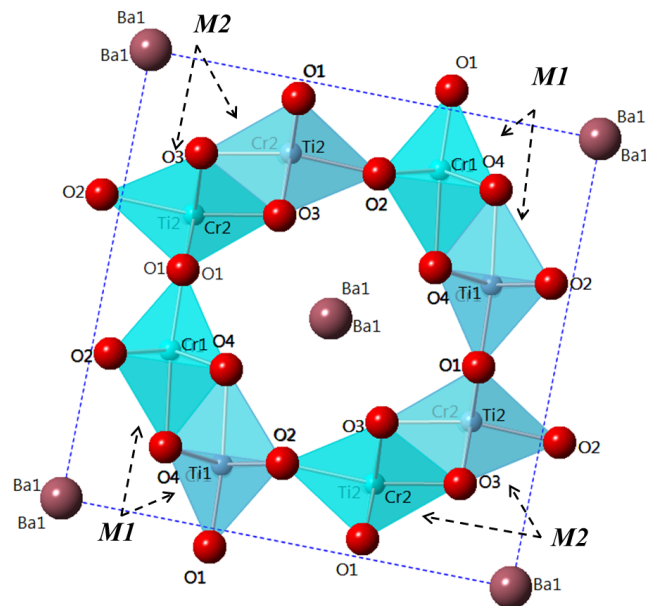


Figure VI-1. Hollandite unit cell with  $I2/m$  symmetry with all crystallographic sites labeled. M1 and M2 are the only two distinct crystallographic sites for octahedral cations (Cr and Ti).

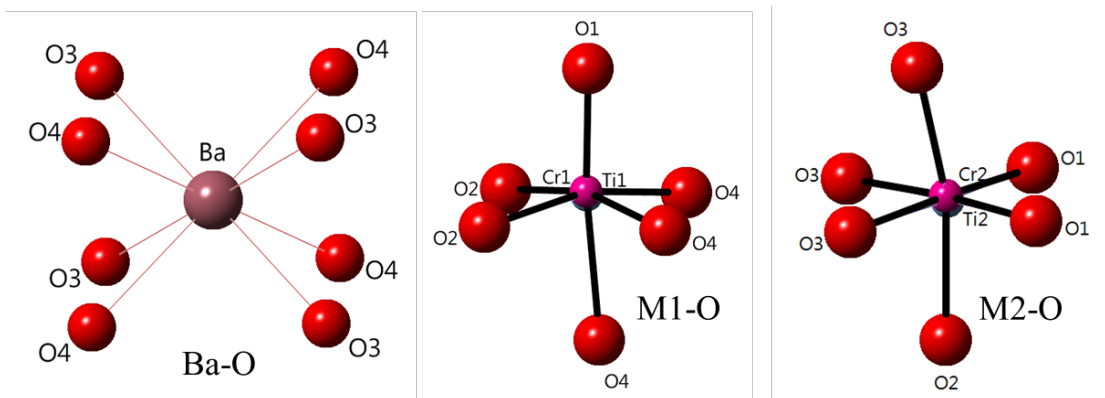


Figure VI-2. Illustrations of oxygen environments surrounding each cation site.

## B. Results and Discussion

### B.1. Solubility of Cs

Phase-pure hollandite samples were obtained for the compositions only in the range  $0 \leq x \leq 0.4$  as observed from powder XRD data (Figure VI-3). For compositions with higher Cs loadings,  $x > 0.4$ , secondary phases appeared that could be indexed to  $\text{BaCrO}_4/\text{Cs}_2\text{CrO}_4$ . The formula unit of  $A_xB_8O_{16}$  hollandite can accommodate a maximum of two tunnel cations. This limits the theoretical Cs solubility in  $\text{Ba}_{1.15-x}\text{Cs}_{2x}\text{Cr}_{2.3}\text{Ti}_{5.7}\text{O}_{16}$  to  $x = 0.85$ . The observed lower Cs solubility indicates partial occupancy of tunnel sites. Extended sintering times to increase Cs uptake were not attempted due to the risk of Cs volatilization.

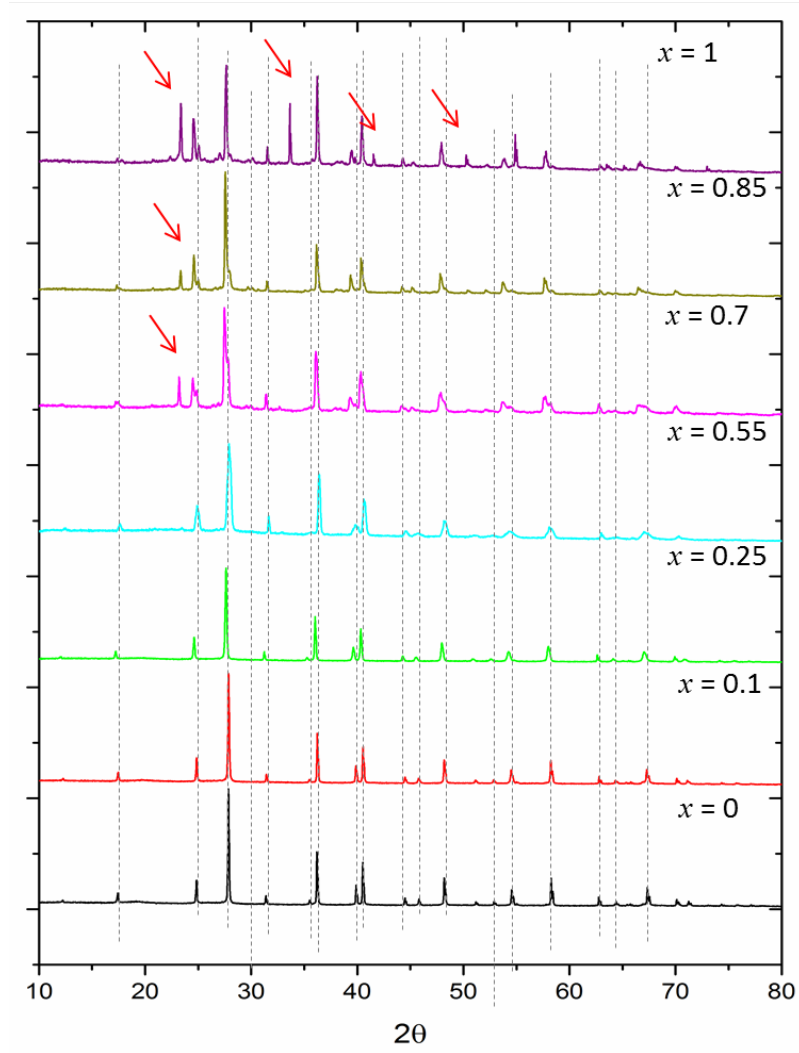


Figure VI-3. Powder XRD patterns of  $\text{Ba}_{1.15-x}\text{Cs}_{2x}\text{Cr}_{2.3}\text{Ti}_{5.7}\text{O}_{16}$ . Red arrows indicate secondary phase(s),  $\text{BaCrO}_4/\text{Cs}_2\text{CrO}_4$  and dotted-vertical lines are hollandite reflections.

Figure VI-4 shows the SEM backscattered electron images of phase-pure hollandites. As is typical of Cs-doped hollandites,<sup>50,56</sup> rod-like morphology was observed in all compositions except for  $x = 0$ .

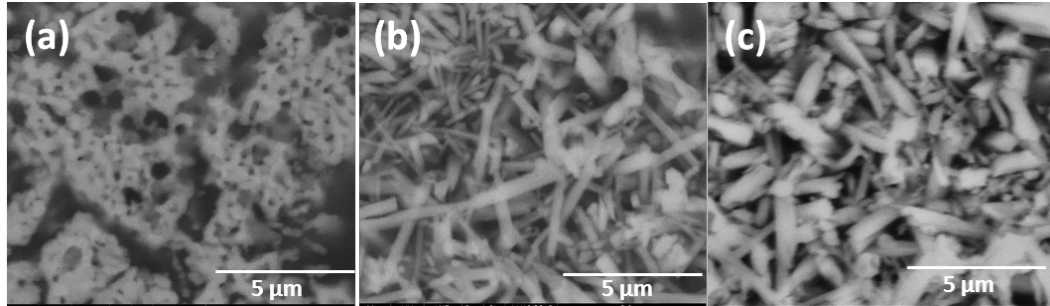


Figure VI-4. BSE images of the polished surfaces of hollandites (a)  $x = 0$  (b)  $x = 0.15$  and (c)  $x = 0.25$ .

## B.2. Rietveld Analysis

Among different tetragonal ( $I4/m$ ) and monoclinic ( $I2/m$ ) models used for Rietveld refinement of powder XRD data,  $I2/m$  symmetry yielded the best fit for all three compositions. Figure VI-5 shows a representative XRD refinement comparing the measured and calculated patterns. The refinements converged with all peak positions accounted for and the generated bond-lengths of reasonable values. However, there is a slight mismatch (weighted Rietveld parameter,  $R_{wp} \sim 9\%$ ) in some of the higher  $2\theta$  peaks' intensities. This could be due to the relative insensitivity of X-ray scattering to oxygen atoms compared to that of heavy atoms Ba, Cs, Cr and Ti. As neutron scattering is more sensitive to the oxygen sub-lattice than X-rays, NPD data can help extract further structural information, with the scattering lengths for O, Ba, and Cs being all similar.

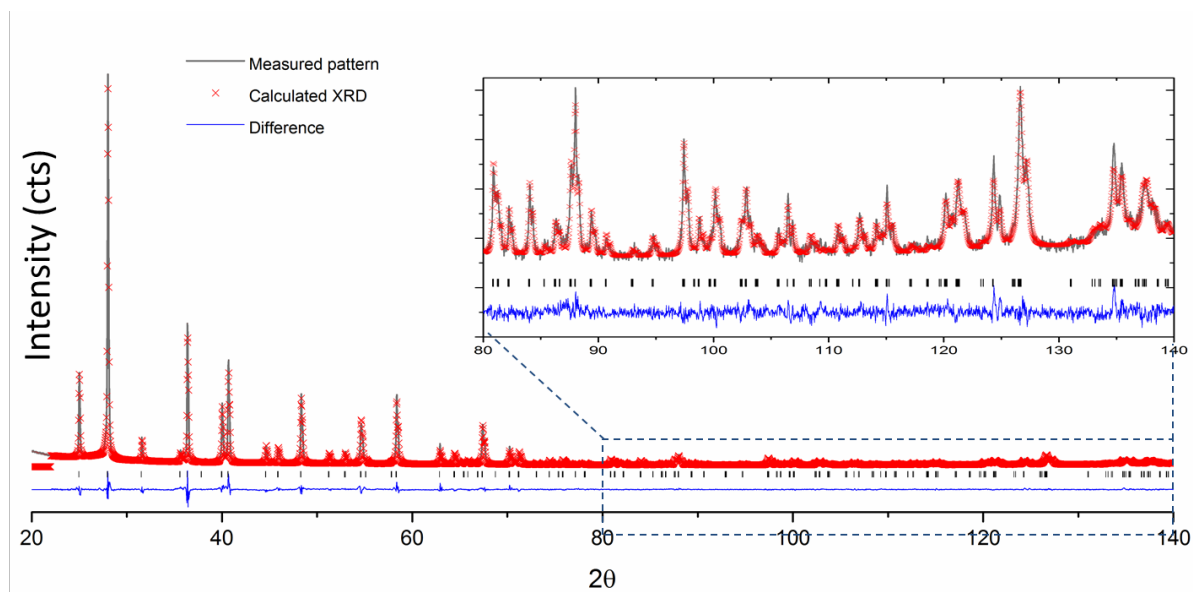


Figure VI-5. Rietveld refinement of powder XRD pattern for the composition



Refinement of NPD data for the composition with no Cs was straightforward and appropriate structural data (Table VI-1 and Table VI-2) were obtained. The refined occupancies were close to the target chemistry and different bond lengths close to those of the starting I2/m model.<sup>49</sup> However, the initial refinement trials of Cs-substituted hollandites ( $x = 0.15$  and  $0.25$ ) converged with unreasonably large ESD values (estimated standard deviations) for tunnel cations' occupancies and ADPs. In order to obtain sensible models, the structure model was simplified to account for the similar scattering lengths of Ba (5.1 fm) and Cs (5.4 fm) by placing only Ba in the tunnel, thus accounting for the Ba and Cs scattering but reducing the number of refined parameters. The resulting models are presented in

Table VI-3, and are primarily intended to show the increasing occupancy of the tunnels with  $x$  to further confirm that Cs is indeed located in the tunnel site. Once this trend was established, refinements were performed for Cs-containing compositions by constraining the Ba and Cs occupancies to the values measured using XRF (

Table VI-4).

Table VI-1. Refined Lattice Parameters for the Composition  $\text{Ba}_{1.15}\text{Cr}_{2.3}\text{Ti}_{5.7}\text{O}_{16}$

		<b>x</b>	<b>y</b>	<b>z</b>	<b>Occupancy</b>	<b>U<sub>iso</sub></b>
	Ba <sup>2+</sup>	0.0	0.0	0.0	0.56(2)	-
M1	Ti <sup>4+</sup>	0.329(2)	0.0	0.140(1)	0.75(1)	0.08(3)
	Cr <sup>3+</sup>	0.330(6)	0.0	0.135(5)	0.25 (1)	
M2	Ti <sup>4+</sup>	0.844(2)	0.0	0.337(1)	0.69(2)	0.03(5)
	Cr <sup>3+</sup>	0.836(3)	0.0	0.335(2)	0.31(2)	
	O <sup>2-</sup>	0.6625(2)	0.0	0.0410(2)	1	0.072(3)
	O <sup>2-</sup>	0.0421(2)	0.0	0.3312(2)	1	0.077(5)
	O <sup>2-</sup>	0.6533(2)	0.0	0.2995(2)	1	0.067(4)
	O <sup>2-</sup>	0.2988(2)	0.0	0.3462(2)	1	0.074(6)

Table VI-2. Selected Bond Lengths Obtained for the Structure of  $\text{Ba}_{1.15}\text{Cr}_{2.3}\text{Ti}_{5.7}\text{O}_{16}$  -  
Different Bond Lengths Listed Below can be Visualized from Figure VI-2

Ba-O			M1-O		M2-O	
Ba-O3	2.943	Equatorial	Cr-O2/Ti-O2	1.991/1.989	Cr-O3/Ti-O3	2.011/2.025
			Cr-O4/Ti-O4	1.979/1.967	Cr-O1/Ti-O1	1.934/1.920
Ba-O4	2.950	Axial	Cr-O4/Ti-O4	2.153/2.095	Cr-O2/Ti-O2	2.074/1.999
			Cr-O1/Ti-O1	1.773/1.831	Cr-O3/Ti-O3	1.882/1.961

Table VI-3. Comparison of Target vs. Refined Compositions of  $\text{Ba}_{1.15-x}\text{Cs}_{2x}\text{Cr}_{2.3}\text{Ti}_{5.7}\text{O}_{16}$  Hollandites ( $x = 0, 0.15$  and  $0.25$ ) when only Ba was used as Tunnel Cation

$x$	Target composition	Refined composition
0.0	$\text{Ba}_{1.15}\text{Cr}_{2.3}\text{Ti}_{5.7}\text{O}_{16}$	$\text{Ba}_{1.12}\text{Cr}_{2.2}\text{Ti}_{5.8}\text{O}_{16}$
0.15	$\text{Ba}_{1.0}\text{Cs}_{0.3}\text{Cr}_{2.3}\text{Ti}_{5.7}\text{O}_{16}$	$\text{Ba}_{1.18}\text{Cr}_{2.14}\text{Ti}_{5.86}\text{O}_{16}$
0.25	$\text{Ba}_{0.9}\text{Cs}_{0.5}\text{Cr}_{2.3}\text{Ti}_{5.7}\text{O}_{16}$	$\text{Ba}_{1.225}\text{Cr}_{2.08}\text{Ti}_{5.92}\text{O}_{16}$

Table VI-4. XRF Measured Compositions of  $\text{Ba}_{1.15-x}\text{Cs}_{2x}\text{Cr}_{2.3}\text{Ti}_{5.7}\text{O}_{16}$  Hollandites ( $x = 0, 0.15$  and  $0.25$ ) - As Compared, Measured Values are Close to the Target Values

$x$	Target composition	XRF measured composition
0.0	$\text{Ba}_{1.15}\text{Cr}_{2.3}\text{Ti}_{5.7}\text{O}_{16}$	$\text{Ba}_{1.15}\text{Cr}_{2.28}\text{Ti}_{5.68}\text{O}_{16}$
0.15	$\text{Ba}_{1.0}\text{Cs}_{0.3}\text{Cr}_{2.3}\text{Ti}_{5.7}\text{O}_{16}$	$\text{Ba}_{0.99}\text{Cs}_{0.3}\text{Cr}_{2.29}\text{Ti}_{5.76}\text{O}_{16}$
0.25	$\text{Ba}_{0.9}\text{Cs}_{0.5}\text{Cr}_{2.3}\text{Ti}_{5.7}\text{O}_{16}$	$\text{Ba}_{0.89}\text{Cs}_{0.49}\text{Cr}_{2.27}\text{Ti}_{5.63}\text{O}_{16}$

Next, the tunnel cations Ba and Cs were fixed at the initial ‘A’ site coordinates,  $(\mathbf{x}, \mathbf{y}, \mathbf{z}) = (0, 0, 0)$ . Since ADPs were used for tunnel cations, any disorder relative to the origin is manifested in those values. Further remarks on this topic are discussed in Section I.B.3.2. A typical NPD refinement with these considerations is shown in Figure VI-6.

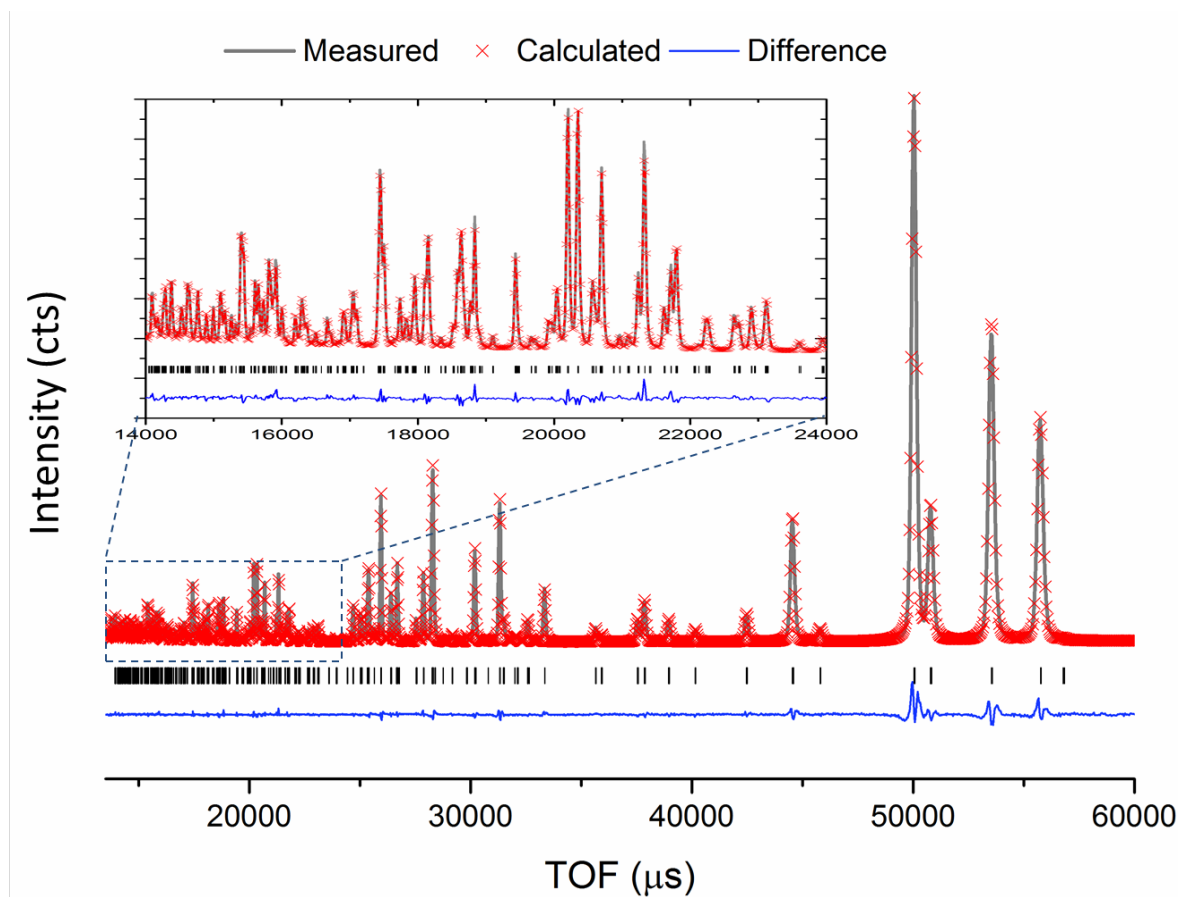


Figure VI-6. Rietveld refinement of NPD data for the composition  $\text{Ba}_{1.0}\text{Cs}_{0.3}\text{Cr}_{2.3}\text{Ti}_{5.7}\text{O}_{16}$ .

### B.3. Structure of $\text{Ba}_{1.15-x}\text{Cs}_{2x}\text{Cr}_{2.3}\text{Ti}_{5.7}\text{O}_{16}$

The lattice parameters and fit parameters generated from the NPD refinements are listed in Table VI-5. Except for the slight increase in the monoclinic nature ( $\beta$ ),  $\sim 0.1^\circ$  from  $x = 0$  to  $x = 0.25$ , no specific trend was observed from the unit cell dimensions,  $a$ ,  $b$  and  $c$ . In addition, the mean diagonal length of tunnel cross-section ( $d$ ) was about the same for  $x = 0$  and  $0.15$ , but increased by  $\sim 0.1\text{\AA}$  for the  $x = 0.25$  sample. The observed changes in lattice parameters are counter intuitive to the idea that the tunnel/lattice parameters increase with the average size of the tunnel cations, and do not corroborate other studies.<sup>22,56,83</sup> Cheary et al. examined the structural effects of Cs substitution in tetragonal hollandites and reported a near-linear increase of lateral dimensions of unit cell ( $a$ ,  $b$ ) in  $\text{Ba}_{1.14}\text{Ti}_8\text{O}_{16}$ <sup>83</sup> as well as  $\text{Ba}_{1.14}\text{Al}_{2.29}\text{Ti}_{5.71}\text{O}_{16}$ <sup>22</sup> systems. Another recent study by Yun Xu et al,<sup>56</sup> showed that for similar tunnel occupancies, lateral dimensions increased in a linear fashion by 2% from  $\text{Ba}_{1.33}\text{Ga}_{2.66}\text{Ti}_{5.34}\text{O}_{16}$  to  $\text{Cs}_{1.33}\text{Ga}_{1.33}\text{Ti}_{6.67}\text{O}_{16}$ . The observed

changes in lattice parameters from  $x = 0$  to  $x = 0.15$  can be attributed primarily to partial occupancy of tunnel sites. The fraction of vacant tunnel sites for compositions  $x = 0$  and  $0.15$  are 42.5% and 35%, respectively. When Cs is introduced into the tunnel, the local expansion of the tunnel cavity is compensated by adjacent vacancies. Furthermore, the electrostatic attraction of Cs towards the oxygen ions surrounding the vacant sites should intensify, resulting in decreased lattice parameters.

The octahedral structural framework for all compositions was typical of the monoclinic hollandite system, where only slight distortions from tetragonal symmetry should be observed. Using the structure of  $x = 0$  composition in Table VI-1 and Table VI-2 as the ‘parent’ structure, the variations that reflect the effects of Cs loading in other compositions are discussed.

Table VI-5. Unit Cell Dimensions and Fit Parameters from Rietveld Refinement of  $\text{Ba}_{1.15-x}\text{Cs}_{2x}\text{Cr}_{2.3}\text{Ti}_{5.7}\text{O}_{16}$  - ‘ $d$ ’ is Average of the Diagonals  $d_1$  and  $d_2$  of the Tunnel Cross-Section and ‘ $R_{wp}$ ’ is the Weighted Rietveld Parameter

Composition	$x = 0$	$x = 0.15$	$x = 0.25$	
<i>Space group</i>	I2/m	I2/m	I2/m	
<i>Unit cell parameters</i>	$a, \text{Å}$	10.0847(3)	10.0244(6)	10.192(1)
	$b, \text{Å}$	2.9590(1)	2.9333(2)	2.977(0)
	$c, \text{Å}$	10.0746(3)	10.0075(6)	10.159 (1)
	$\beta$	90.032 (2)	90.058(2)	90.126(3)
	<i>Volume, <math>V, \text{Å}^3</math></i>	300.63(2)	298.95(3)	303.34(7)
	$d = (d_1 + d_2)/2, \text{Å}$	5.0965	5.0865	5.1790
<i>Refinement parameters</i>	$R_{wp}, \%$	3.14	3.68	4.83

### B.3.1. Framework changes

Incorporation of Cs into the lattice occurs by redistribution of Ti and Cr on the M1 and M2 sites, causing corresponding octahedral distortions. For the composition  $x = 0$ , the ratio of Ti/Cr on the M1 site is clearly higher compared to that of M2 (Table VI-1). On addition of Cs, the ratio decreases on the M1 site and increases on the M2 site

i.e., some Ti ions on the M1 site are substituted by Cr from the M2 site and vice-versa. Table VI-6 shows this trend – Ti/Cr occupancy reduced from 0.75/0.25 ( $x = 0$ ) to 0.71/0.29 ( $x = 0.25$ ) on M1 site and from 0.69/0.31 ( $x = 0$ ) to 0.75/0.25 ( $x = 0.25$ ) on M2 site. There is slight deviation in the refined total occupancy ratio Ti/Cr from the target values which is within the range of observed ESDs in all cases. All oxygen octahedra,  $(\text{Cr/Ti})\text{O}_6$ , are moderately distorted, as seen from different Cr/Ti-O bond lengths listed in Table VI-2. The effects of addition of Cs into the lattice are particularly observed through the octahedral axial bonds located at the corner-shared octahedra. These bonds are illustrated in Figure VI-7. When viewed down the  $b$ -axis, the tunnels are surrounded by four walls, each consisting of two edge-shared octahedra, interconnected by sharing an oxygen at the corner (Figure VI-7a). The strain induced by Cs addition is predominant in the octahedra that contain the corner-shared oxygen as axial bonds: M1-O1 and M2-O2. No significant trend was observed in the deformation of other bonds in the octahedra. Further, it was observed that these bonds lie perpendicular to the tunnel direction ( $b$ -axis) indicating that the addition of Cs in the lattice introduces lateral deformation of the tunnels, facilitated by elongation of M1-O1 and M2-O2 bonds. Both the M1 and M2 sites host both Cr and Ti, and Figure VI-8 shows that the elongations of the individual bonds Cr-O and Ti-O on M1 and M2 sites. The significantly high distortion of Cr-O1 (M1 site) and Cr-O2 (M2 site) bonds compared to the respective Ti-O1 and Ti-O2 bonds is evident. One of the characteristics of transition metal-oxygen octahedra is the Jahn-Teller (JT) effect that may be linked to the overall octahedral distortion. To verify that the higher deformation of  $\text{CrO}_6$  octahedra in our case is not due to JT effects, high-resolution X-ray photoelectron spectroscopy (XPS) experiments were performed on the powder samples. The XPS data confirmed the oxidation state of Cr as +3 in all compositions with electronic configuration being uncondusive for JT effects. The refinements indicate that the addition of larger Cs ions preferentially stretches the Cr-O bond in the surrounding octahedra. This is further linked to the redistribution of Cr/Ti on the M1 and M2 sites observed from the refined occupancies in Table VI-6.

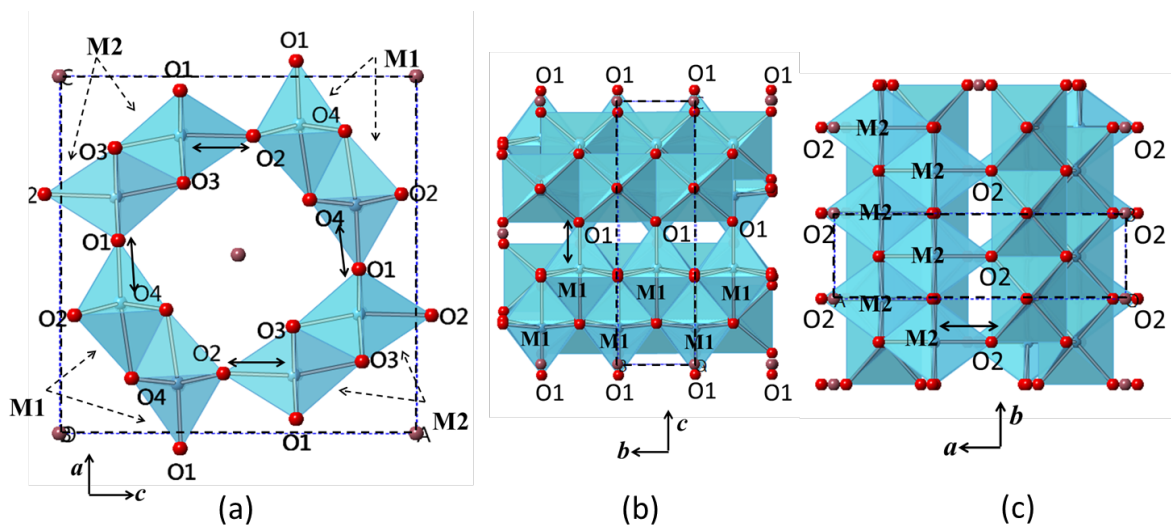


Figure VI-7. Unit-cell (black dotted-line) along different crystallographic directions, showing the elongated bonds (black double-arrows) and corresponding (M1/M2)O<sub>6</sub> octahedra. (a) View along tunnel direction (*b*-axis) shows M1-O1 and M2-O2 bonds at corner-shared oxygen sites, (b) and (c) shows M1-O1 and M2-O2 bonds respectively that lie normal to the *b*-axis.

Table VI-6. Occupancies of the *M*<sub>1</sub> and *M*<sub>2</sub> sites Showing the Redistribution of Cr and Ti ions - Occupancies of Ba and Cs ions are Constrained to the Highlighted Values

<i>x</i>		<i>x</i>	<i>y</i>	<i>z</i>	Occupancy	<i>U</i> <sub>iso</sub>
	<b>Ba<sup>2+</sup>/Cs<sup>+</sup></b>	0.0	0.0	0.0	<b>0.50/0.15</b>	-
0.15	M1 <b>Ti<sup>4+</sup>/Cr<sup>3+</sup></b>	0.33 (0)/0.34(0)	0.0	0.14(0)/0.14(1)	0.74/0.26 (1)	0.005(2)
	M2 <b>Ti<sup>4+</sup>/Cr<sup>3+</sup></b>	0.84(0)/0.83(0)	0.0	0.34(0)/0.33(0)	0.73/0.27 (1)	0.000(3)
	<b>Ba<sup>2+</sup>/Cs<sup>+</sup></b>	0.0	0.0	0.0	<b>0.40/0.25</b>	-
0.25	M1 <b>Ti<sup>4+</sup>/Cr<sup>3+</sup></b>	0.33(2)/0.33(5)	0.0	0.15(2)/0.15(5)	0.71/0.29(1)	0.003(2)
	M2 <b>Ti<sup>4+</sup>/Cr<sup>3+</sup></b>	0.83(0)/0.84 (0)	0.0	0.33(0)/0.33(0)	0.75/0.25 (2)	0.004(4)

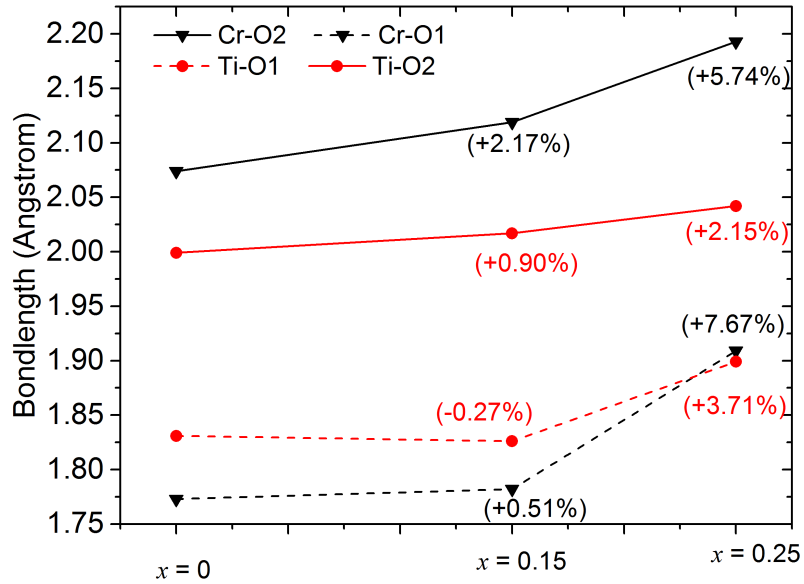


Figure VI-8. Variation of Cr-O and Ti-O bond lengths on the  $M_1$ (dotted line) and  $M_2$  (solid line) sites. Error bars are smaller than the data markers.

### B.3.2. Tunnel ion order/disorder

Table VI-7 shows the ADPs ( $\beta_{ij}$  -  $i, j = 1, 2, 3$ ) obtained from the refinements. Compared to other the components,  $\beta_{22}$  is significantly higher for all compositions. Large  $\beta_{22}$  denotes the uncertainty or disorder associated with the location of the tunnel cation along the tunnel direction. This is illustrated in Figure VI-9, where the oblong ellipsoids represent the tunnel cation disorder. Similar anisotropic parameters for tunnel cations have been reported for various hollandite ordered superstructures.<sup>48,83-85</sup> The presence of partially occupied tunnels giving rise to supercell structures has been mentioned in Section I.B. A schematic of hollandite supercells is shown in Figure I-4. The ordered configuration adopted by the cations and vacancies in a supercell is translated across the lattice as illustrated in the Figure I-4. In such cases, depending upon the neighboring sites in the supercell, a small displacement ( $\pm\delta y$ ) from the original tunnel site,  $(x, y, z) = (0, 0, 0)$ , occurs in individual unit cells resulting in a positional disorder of tunnel cations,  $(x, y, z) = (0, \pm\delta y, 0)$ .<sup>84</sup> For example, tunnel cations having a vacancy and another cation as immediate neighbors along the tunnel direction might displace

towards vacant site. Hence, there can be an overall disorder introduced for the tunnel sites along the tunnel direction within each supercell that is represented by the high value of the  $\beta_{22}$  component.

Table VI-7. Refined ADPs of Tunnel Cations of  $\text{Ba}_{1.15-x}\text{Cs}_{2x}\text{Cr}_{2.3}\text{Ti}_{5.7}\text{O}_{16}$  Compositions,  $\beta_{12}=\beta_{23}=0$  (by I2/m symmetry)

Composition	$\beta_{11}$	$\beta_{22}$	$\beta_{33}$	$\beta_{13}$
$x = 0$	0.012(3)	<b>0.162(11)</b>	0.023(1)	-0.015(4)
$x = 0.15$	0.018(3)	<b>0.175(11)</b>	0.041(5)	-0.028(4)
$x = 0.25$	0.079(11)	<b>0.168(17)</b>	0.037(7)	0.052(7)

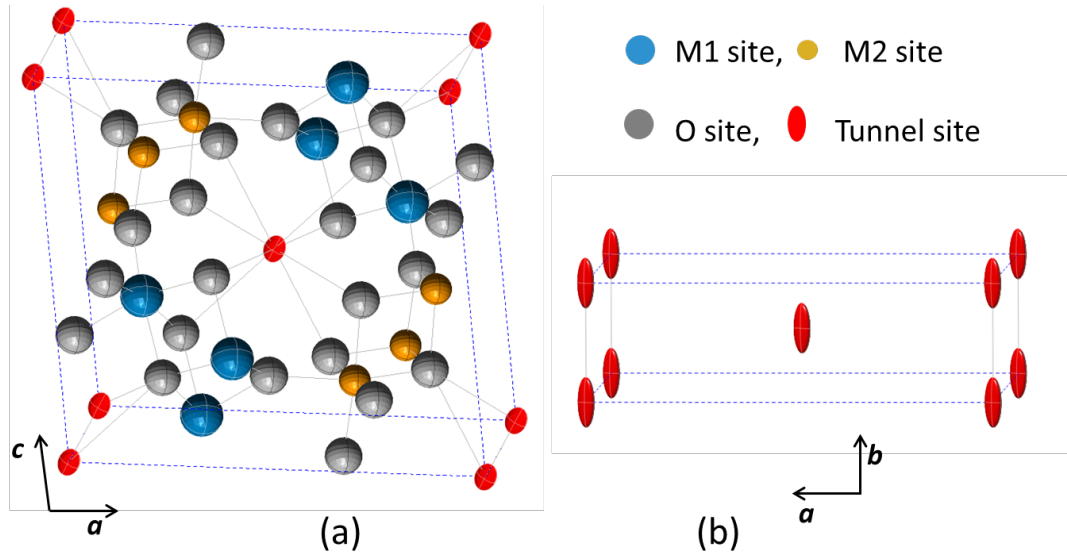


Figure VI-9. (a) Thermal ellipsoids of of different sites in  $\text{Ba}_{1.15}\text{Cr}_{2.3}\text{Ti}_{5.7}\text{O}_{16}$  unit cell. (b) View of the same along [001] illustrating the oblong ellipsoids of tunnel sites that represent the large  $\beta_{22}$  displacement parameter.

The formation of superstructures in Ba-hollandites is often supported by the presence of satellite reflections in XRD and electron diffraction patterns.<sup>48,52-55</sup> Figure VI-10 shows the SAED pattern along [101] zone axis of the sample  $\text{Ba}_{1.15}\text{Cr}_{2.3}\text{Ti}_{5.7}\text{O}_{16}$ . All Bragg

reflections could be indexed by the monoclinic model generated for XRD and NPD refinements. In addition, the diffraction pattern displays lines of sharp satellite reflections that are normal to the reciprocal lattice vector  $\mathbf{b}^*$  indicating modulation along  $b$ -axis. Once all Bragg reflections were indexed accordingly, the modulation vector ( $\mathbf{q}^*$ ) was identified as  $\mathbf{q}^* \sim 0.46\mathbf{b}^*$ . In hollandites, tunnel-ion ordering resulting in compositionally-modulated superstructures typically produces similar satellite reflections.<sup>3,52,54</sup> This is further supported by XRD data. A closer examination of the powder XRD patterns (Figure VI-11) reveals small diffuse satellite peaks at  $2\theta \sim 19.5^\circ$ . Domains within the hollandite structure containing ordered tunnel cations/vacancies contribute to the diffuse reflections in XRD patterns.<sup>3,52</sup> In order to verify the proposition of superstructures, the  $d$ -spacings corresponding to the satellite reflections in TEM and XRD data were compared. It was observed that the SAED modulation vector  $\mathbf{q}^* \sim 0.46\mathbf{b}^*$  and the XRD reflection,  $2\theta \sim 19.5^\circ$ , both are equivalent to  $d \sim 4.5 \text{ \AA}$ . Hence the observations from electron diffraction and XRD are consistent with the tunnel-ion ordered hollandite superstructures. TEM data was not collected other samples ( $x = 0.15$  and  $0.25$ ), however, the XRD patterns hint at similar structural features as those of  $x = 0$  sample. XRD satellite reflections are present at  $2\theta \sim 19.5^\circ$ , but with increasing Cs content, the reflections become less intense (Figure VI-11). The lower intensity can be due to the lack of long-range ordering of tunnel cations. The higher the degree of ordering, or the larger the domain size of the superstructures, the sharper are the satellite reflections. In the case of Cs-containing hollandites, substitution of one smaller  $\text{Ba}^{2+}$  ( $r_{\text{Ba}^{2+}} \sim 1.5 \text{ \AA}$ ) with two  $\text{Cs}^+$  ( $r_{\text{Cs}^+} \sim 1.8 \text{ \AA}$ ) cations may slow down the diffusion kinetics of Cs the tunnels, resulting in a lower degree of ordering. Collectively, our SAED and XRD observations suggest superstructures in  $\text{Ba}_{1.15-x}\text{Cs}_{2x}\text{Cr}_{2.3}\text{Ti}_{5.7}\text{O}_{16}$  ( $x = 0, 0.15$  and  $0.25$ ) hollandites and ADPs generated from NPD refinement indicate the positional disorder of Ba/Cs tunnel cations within a supercell.

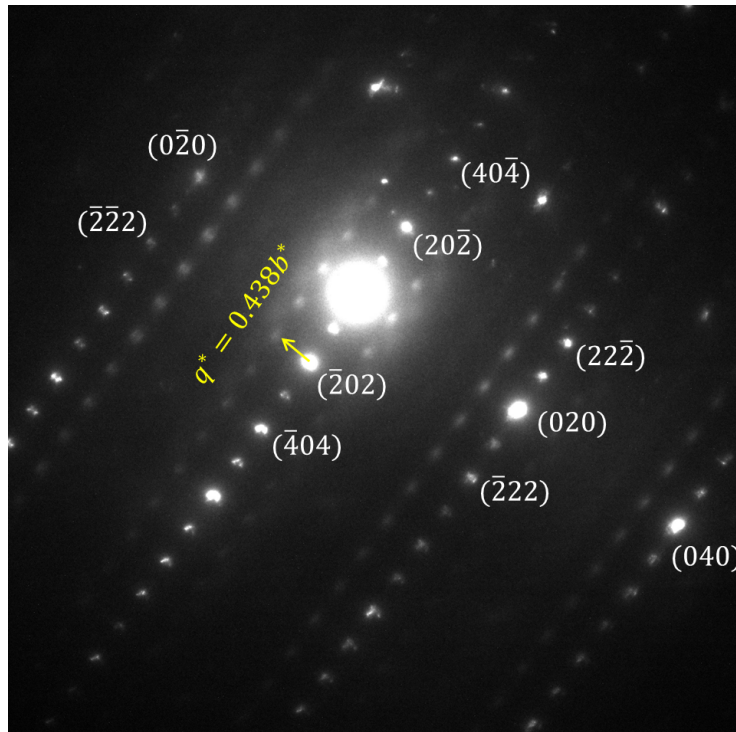


Figure VI-10. SAED pattern along [101] zone axis for the composition  $x = 0$ .

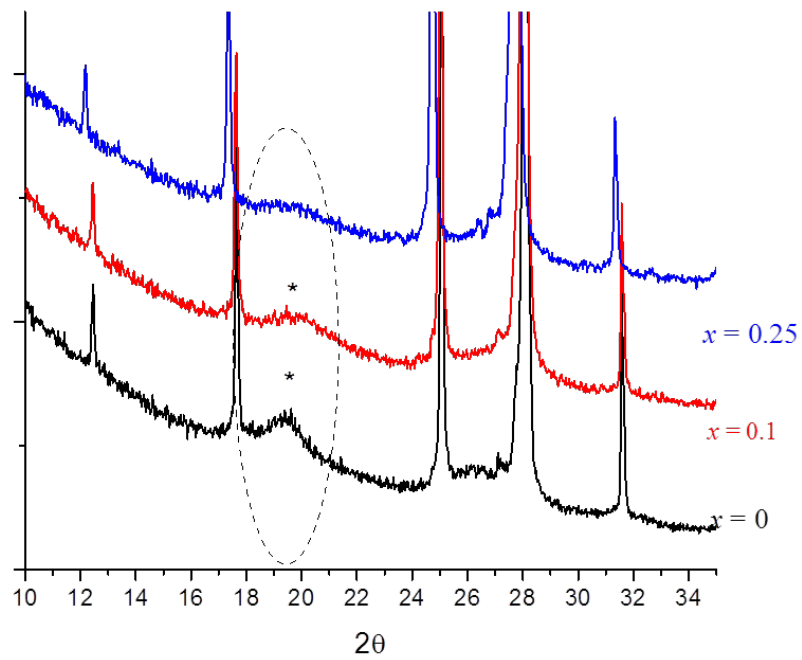


Figure VI-11. Powder XRD patterns showing the satellite reflections at low  $2\theta$  as indicated.

### C. Conclusion

The present study shows that in the hollandite system  $\text{Ba}_{1.15}\text{Cr}_{2.3}\text{Ti}_{5.7}\text{O}_{16}$ , approximately ~35% of the Ba can be replaced by Cs, beyond which secondary phases are observed. Rietveld refinement of XRD and NPD data of the phase-pure hollandites,  $\text{Ba}_{1.15-x}\text{Cs}_{2x}\text{Cr}_{2.3}\text{Ti}_{5.7}\text{O}_{16}$  ( $x = 0, 0.15$  and  $0.25$ ), confirm the monoclinic  $I2/m$  symmetry of the lattice with  $b$ -axis tunnels, hosting Ba and Cs ions, surrounded by  $\text{CrO}_6$  and  $\text{TiO}_6$  octahedra. The accommodation of larger Cs ions in the parent structure  $\text{Ba}_{1.15}\text{Cr}_{2.3}\text{Ti}_{5.7}\text{O}_{16}$  is attained by deformation of surrounding oxygen octahedra. Cr-O1 and Cr-O2 bonds, on M1 and M2 sites respectively, normal to the tunnel direction are observed to have the highest strain (Figure VI-8) compared to other bonds suggesting that Cs sites are surrounded locally by distorted  $\text{CrO}_6$  octahedra. The presence of tunnel-ion ordered superstructures is evident from satellite reflections in XRD and electron diffraction data. Further, the degree of ordering is reduced with increasing Cs content/tunnel occupancy. On the other hand, large APDs along the tunnel-direction,  $\beta_{22}$ , are attained from NPD refinements which are attributed to the local disorder within a supercell. This was observed for all three compositions.

## PERFORMANCE TESTING OF PHASE-PURE HOLLANDITES

Chemical durability and resistance to irradiation damage are two important criteria commonly used to validate a material's applicability as a waste form. The compositions,  $\text{Ba}_{1.15-x}\text{Cs}_{2x}\text{Cr}_{2.3}\text{Ti}_{5.7}\text{O}_{16}$ , yielding phase-pure hollandites were evaluated for their performance as waste form materials. In this study, relevant experiments were performed in an attempt to identify qualitatively the effectiveness of the selected compositions in Cs immobilization.

### A. Chemical Durability

Typically, the waste form materials are tested for chemical durability by various types of leaching tests performed in different environmental conditions.<sup>62,86-89</sup> The leaching tests are designed to simulate the geological conditions waste forms are exposed to, and to determine kinetics of release rates of different hazardous elements into the biosphere. Many studies reported the mechanism/kinetics of leaching behavior of different waste forms. In this study, Cs leaching from  $\text{Ba}_{1.15-x}\text{Cs}_{2x}\text{Cr}_{2.3}\text{Ti}_{5.7}\text{O}_{16}$  hollandites was measured using an ASTM standard testing method, Product Consistency Test (PCT).<sup>88</sup> PCT tests have been traditionally used for glass waste forms. There has not been a standardized durability testing method for ceramic waste forms, but PCT test can still be used to determine the key issues relating the behavior of waste form dissolution in aqueous environments. PCT tests used in this study were performed at SRNL.

#### A.1. Experimental

##### A.1.1. Material Processing

Single-phase hollandites,  $\text{Ba}_{1.15-x}\text{Cs}_{2x}\text{Cr}_{2.3}\text{Ti}_{5.7}\text{O}_{16}$  ( $0 \leq x \leq 0.4$ ), prepared by sol-gel synthesis had been observed to have very fine grain size,  $\sim 2\text{-}5 \mu\text{m}$  (Figure VI-4). For the durability testing method used, as discussed in Section I.A.1.2, this grain size was deemed undesirable. Hence, hollandites prepared using conventional sintering process were used for durability testing as well as for irradiation experiments.

### **A.1.2. Leaching test**

The standard PCT test is a static leaching test performed at a fixed temperature of 90°C for 7 days.<sup>88</sup> Hollandite pellets were ground to produce ~5 g of crushed sample (-100, +200 mesh) which was further washed off repeatedly with ASTM Type-I water to get rid of any fines. Triplicate batches of dried sample, each of 1.5 g, were then taken in stainless steel containers and 15 ml of ASTM Type-I water was added to each of them. The containers were then tightly sealed, placed in an oven at 90°C for the duration of the test. The specifics of sample preparation, experimental set up and relevant calculations are explained in detail in the ASTM standard.<sup>88</sup>

The leaching behavior of the test samples was studied by analyzing the chemical composition of the sample prior to the test and leachant composition after the test. It is essential to measure the composition of the crushed and washed sample before the leaching test to account for any loss of water-soluble phases during washing. The compositional analysis of the leachant compares the relative amounts of different elements leached during the test.

### **A.1.3. Chemical composition**

Initial chemical compositions of the samples prepared for leach tests were measured by preparing a fusion mixture of sample and a standard compound, dissolving the mixture in ASTM Type-I water that was further analyzed for elemental concentrations. Inductively Coupled Plasma – Atomic Emission Spectroscopy (ICP-AES) was used to measure elemental concentrations except Cs which, was measured using Inductively Coupled Plasma-Mass Spectroscopy (ICP-MS). A representative amount from each sample (~0.15 g) was prepared via a sodium peroxide fusion (PF) method and dissolved in 250 ml water. These samples were analyzed for each element of interest by ICP-AES and Cs by ICP-MS. The instrumentation was re-calibrated between the analyses and standards were intermittently measured to ensure the performance of the ICP instruments over the course of the analyses. The measured cation concentrations were converted to their respective oxide to obtain a wt.% of each component oxide.

#### **A.1.4. Leachant analysis**

The leachants after the PCT tests were generally diluted to different levels depending on the concentrations of different elements in the leachant solution. The idea was to prepare sufficiently dilute solution for ICP measurements. The measured concentrations were normalized for comparison.

#### **A.1.5. Phase analysis**

In addition to the compositional analysis, the phase purity and/or phase changes (if any) were observed using XRD and SEM techniques.

### **A.2. Results and Discussions**

#### **A.2.1. Chemical Composition**

The measured compositions of the hollandite samples prepared for PCT testing are presented in Table VII-1. To have a better comparison of the measured and target compositions, the measured cation concentrations were converted to their respective oxide contents and the resultant compositions were normalized to 16 oxygen atoms per unit formula. The loss of Cs, as evident from the measured compositions, could be due to multiple factors. Volatilization of Cs during sintering could be a key factor. A closer look at the micrographs of the polished samples (Figure VII-1) indicates the presence of Cs-rich phases in all Cs containing hollandites. These Cs-rich phases – possibly water-soluble – could have been washed away during PCT sample preparation resulting in Cs losses as observed. Sol-gel samples (Figure VI-4), on other hand, prepared from highly homogeneous and reactive precursors has no Cs segregation and thereby little to no Cs loss.

Table VII-1. Compositions of Hollandite Series  $\text{Ba}_{1.15-x}\text{Cs}_{2x}\text{Cr}_{2.3}\text{Ti}_{5.7}\text{O}_{16}$  Measured by ICP

Compositions of $\text{Ba}_{1.15-x}\text{Cs}_{2x}\text{Cr}_{2.3}\text{Ti}_{5.7}\text{O}_{16}$ used	Target composition	Measured composition
$x = 0$	$\text{Ba}_{1.15}\text{Cr}_{2.30}\text{Ti}_{5.70}\text{O}_{16}$	$\text{Ba}_{1.25}\text{Cr}_{2.31}\text{Ti}_{5.64}\text{O}_{16}$
$x = 0.15$	$\text{Ba}_{1.00}\text{Cs}_{0.30}\text{Cr}_{2.30}\text{Ti}_{5.70}\text{O}_{16}$	$\text{Ba}_{1.03}\text{Cs}_{0.16}\text{Cr}_{2.25}\text{Ti}_{5.76}\text{O}_{16}$
$x = 0.25$	$\text{Ba}_{0.90}\text{Cs}_{0.50}\text{Cr}_{2.30}\text{Ti}_{5.70}\text{O}_{16}$	$\text{Ba}_{0.94}\text{Cs}_{0.26}\text{Cr}_{2.20}\text{Ti}_{5.81}\text{O}_{16}$
$x = 0.4$	$\text{Ba}_{0.75}\text{Cs}_{0.80}\text{Cr}_{2.30}\text{Ti}_{5.70}\text{O}_{16}$	$\text{Ba}_{0.79}\text{Cs}_{0.40}\text{Cr}_{2.32}\text{Ti}_{5.76}\text{O}_{16}$

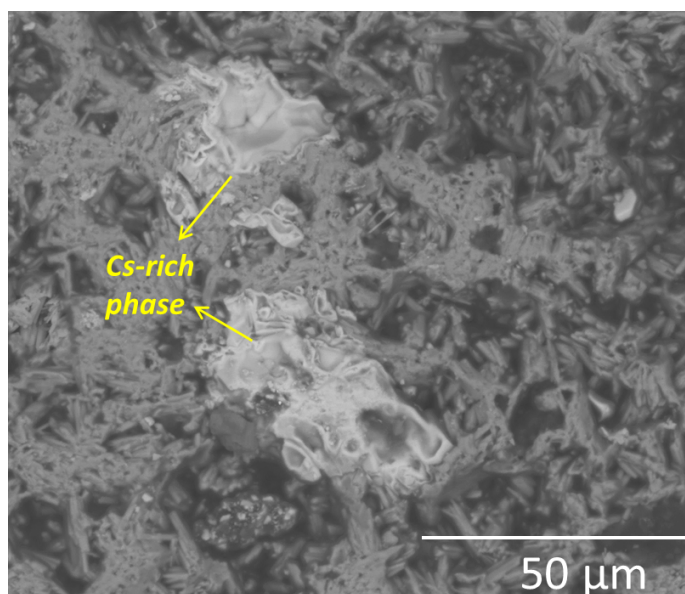


Figure VII-1. SEM-BSE micrograph of  $\text{Ba}_{1.0}\text{Cs}_{0.3}\text{Cr}_{2.3}\text{Ti}_{5.7}\text{O}_{16}$  showing bright phases rich in Cs. Similar Cs-rich areas were found in other Cs-containing compositions.

### A.2.2. PCT Testing and Leachant Analysis

Hollandite composition without Cs could not be tested using PCT since the observed grain size was too small to obtain sufficient sample with -100 to +200 US mesh size range. The following section hence presents the leaching rates of different elements in other compositions ( $x = 0.15, 0.25$  and  $0.4$ ). The concentrations of different elements in the leachants after 7 days of PCT testing were measured by ICP-AES and ICP-MS (for Cs). The leachant concentrations determined from ICP are then normalized by respective elemental weight percentages in each of the compositions. Figure VII-2 presents the leachant concentrations (mg/L) for Cs and Cr elements. Ti levels were observed to be below the instrument sensitivity and Ba was observed to have very low levels ( $< 5$  mg/L) for all three compositions. In addition to leachant analysis, the material after PCT testing was dried and characterized for any phase transformations. Figure VII-3 shows the powder XRD patterns of the PCT-tested samples. It can be seen that hollandite crystalline structure was retained after the leach tests for all compositions.

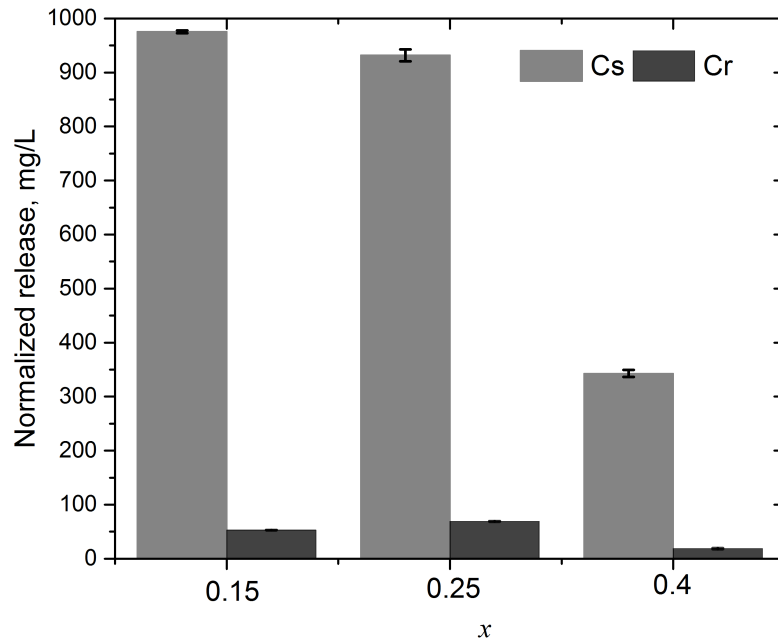


Figure VII-2. Leach rates of Cs and Cr from different hollandites  $Ba_{1.15-x}Cs_{2x}Cr_{2.3}Ti_{5.7}O_{16}$  measured by ICP. The concentrations (mg/L) presented are normalized by the weight percentages of respective elements in the composition.

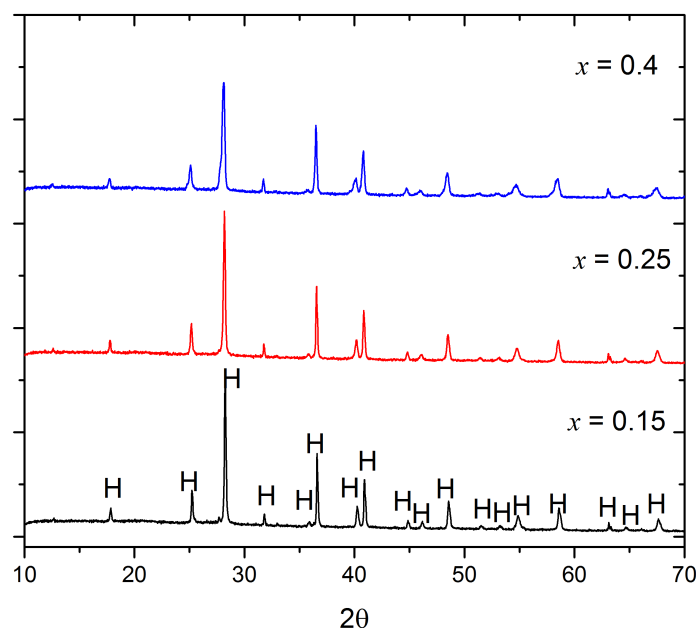


Figure VII-3. XRD patterns of hollandite samples after PCT testing. All crystalline peaks observed indicate that the hollandite (H) structure is preserved after 7 days of PCT leach testing without addition of secondary crystalline phases.

The leaching behavior of hollandites has been a subject of many studies.<sup>90-93</sup> A majority of these studies deal with the microstructural/morphological factors affecting the leaching behavior. For example, in the case of hollandites with  $\text{Al}^{3+}$  as trivalent cation, a passivation layer of  $\text{Al}(\text{OH})_3$  formed on the grain surface after an initial release of Ba/Cs would restrict further losses from centers of the grains<sup>91</sup> over the period of time. Hollandites with  $\text{Ti}^{3+}$  cation, in oxidizing conditions, lose Cs from the grain surface due to redox reactions involving oxidation of  $\text{Ti}^{3+}$  to  $\text{Ti}^{4+}$ . The surface hollandite layer eventually dissolves forming  $\text{TiO}_2$  which reduces the tunnel ion leach rate over the course of time.<sup>93</sup> Xu et. al.<sup>56</sup> have examined both microstructural and structural (lattice parameters) effects on ionic mobility of tunnel cations at different Cs loadings. At similar levels of Ba or Cs in the tunnels, the measured overall tunnel ion mobility remains unaffected. Microstructural factors such as crystallite size and grain boundaries have been reported to be more influential in determining the effectiveness of tunnel ion retention.

The durability data presented here shows that although there was no observable phase change(s), Cs was released from the hollandite lattice. Cs extraction was accompanied particularly by Cr. From our structural analysis (Section VI), Cs prefers to be accommodated between the  $\text{CrO}_6$  octahedral networks in  $\text{Ba}_{1.15-x}\text{Cs}_{2x}\text{Cr}_{2.3}\text{Ti}_{5.7}\text{O}_{16}$  hollandites. Hence it is likely that when water molecules preferentially attack  $\text{CrO}_6$  sites, Cs is eventually released from the lattice. Investigation of this hypothesis can be accomplished through in-situ observations of interface reaction between water and hollandite lattice.

Further, the relative amount of leached Cs reduced with increasing Cs content of hollandite. No direct correlation between the structural parameters and Cs leach rates is observed from the data. The Cs release was suppressed as the tunnels are populated with Cs ions. The superstructures of hollandites, as discussed in Section I.B.2, tend to have different-sized tunnel cations,  $\text{Ba}^{2+}$  ( $r_{\text{Ba}^{2+}} \sim 1.5 \text{ \AA}$ ) and  $\text{Cs}^+$  ( $r_{\text{Cs}^+} \sim 1.8 \text{ \AA}$ ), and vacancies in an ordered fashion creating ‘bottlenecks’ that hinder the migration of the ions. Phase-pure compositions of  $\text{Ba}_{1.15-x}\text{Cs}_{2x}\text{Cr}_{2.3}\text{Ti}_{5.7}\text{O}_{16}$  used in this study have been observed to have superstructures (Section VI). Hence increased tunnel occupancy in these ordered superstructures could result in increased retention of Cs in the tunnels. In summary, this work provides preliminary insights into leach behavior of phase-pure hollandites of interest, however, the underlying mechanism of Cs extraction and its kinetics still needs to be studied in detail in the future.

## **B. Irradiation Resistance**

A majority of the radiation events during the storage of waste forms occur from  $\beta$ -decay of the fission products and  $\alpha$ -decay of the actinide elements. As briefly mentioned in Section I.A.1.1, these two events interact with the waste forms in different ways. This study is primarily interested in effects of  $\alpha$ -decay events on hollandites since the associated damage – cascading effects leading to atomic displacements – is of a major concern. Actinides and their daughter products have long half-lives and therefore  $\alpha$ -decay becomes dominant over long time scales. An  $\alpha$ -decay event consists of the release of an  $\alpha$ -particle ( $\text{He}^{2+}$ ) and an  $\alpha$ -recoil nucleus (heavy particle). The  $\alpha$ -particles transfer their energy to electrons through ionization and electronic excitations and deposit their

remaining energy through engage in ballistic processes at the end of their track (16 to 22  $\mu\text{m}$ ). In contrast,  $\alpha$ -recoil nuclei lose nearly all of their energy in ballistic processes over a considerably shorter range of 30 to 40 nm. The  $\alpha$ -recoils produce several thousand displacements in a localized area while  $\alpha$ -particles generate several hundred displacements during their longer travel.<sup>94-96</sup> In summary, the energies of  $\alpha$ -radiation and recoil nuclei can cause atomic-scale rearrangements, which lead to both physical and chemical property alteration, making the analysis of these events of critical importance. This necessitates the use of ion implantation techniques to study the effects of  $\alpha$ -decay on the laboratory time scale to simulate the irradiation conditions during the storage in a repository. In the following sections, the response of selected phase-pure hollandites during ion implantation experiments is discussed. The primary goal of this part of the study is to qualitatively analyze the type of damage induced as a function of the ion irradiation dosage.

## **B.1. Experimental**

### **B.1.1. Sample Preparation**

For ion-irradiation, selected phase-pure hollandites  $\text{Ba}_{1.15-x}\text{Cs}_{2x}\text{Cr}_{2.3}\text{Ti}_{5.7}\text{O}_{16}$  ( $x = 0, 0.15$  and  $0.4$ ) were prepared in a similar fashion as mentioned in Section I.A.1.2. The sintered pellets were polished using  $1\mu\text{m}$  diamond suspension and the polished surfaces were used for irradiation studies.

### **B.1.2. Ion-irradiation experiments**

Simulated ion-irradiation experiments on phase-pure  $\text{Ba}_{1.15-x}\text{Cs}_{2x}\text{Cr}_{2.3}\text{Ti}_{5.7}\text{O}_{16}$  hollandites ( $x = 0, 0.15$  and  $0.25$ ) were conducted at Ion Beam Laboratory at State University of New York (SUNY), Albany, NY. Two types of irradiation were used – 380 keV  $\text{He}^{2+}$  ions to simulate  $\alpha$ -radiation and 3 MeV  $\text{Kr}^{3+}$  ions to simulate heavy nuclei recoil during  $\alpha$ -decay. The fluences used were  $2.8 \times 10^{16} \text{He}^{2+}/\text{cm}^2$  and  $2 \times 10^{16} \text{Kr}^{3+}/\text{cm}^2$ .

### **B.1.3. Irradiated Surface Analysis**

The changes induced by ion-irradiation were examined by comparing the surface features before and after irradiation. Grazing incidence XRD (GIXRD) patterns

(angle of incidence – 2°) from the polished surfaces were collected (D8 Phases, Bruker, USA) in the range 2θ: 10 - 60°, with a step size of 0.04° and dwell time of 40s. For better comparison of the surface before and after irradiation, similar scanning parameters were used for data collection. SEM microstructures were also examined to detect any microstructural effects upon irradiation.

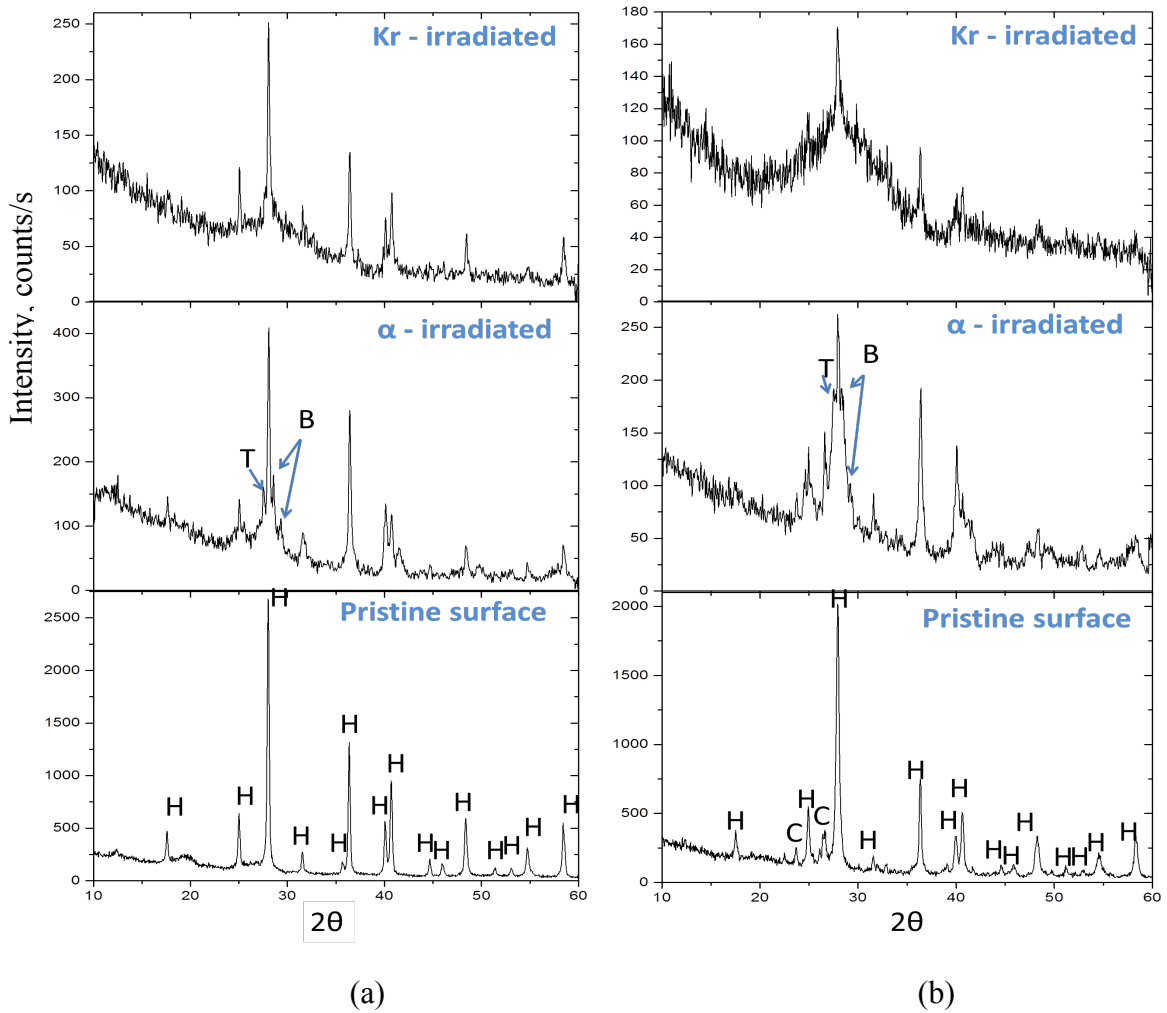
## **B.2. Results and Discussions**

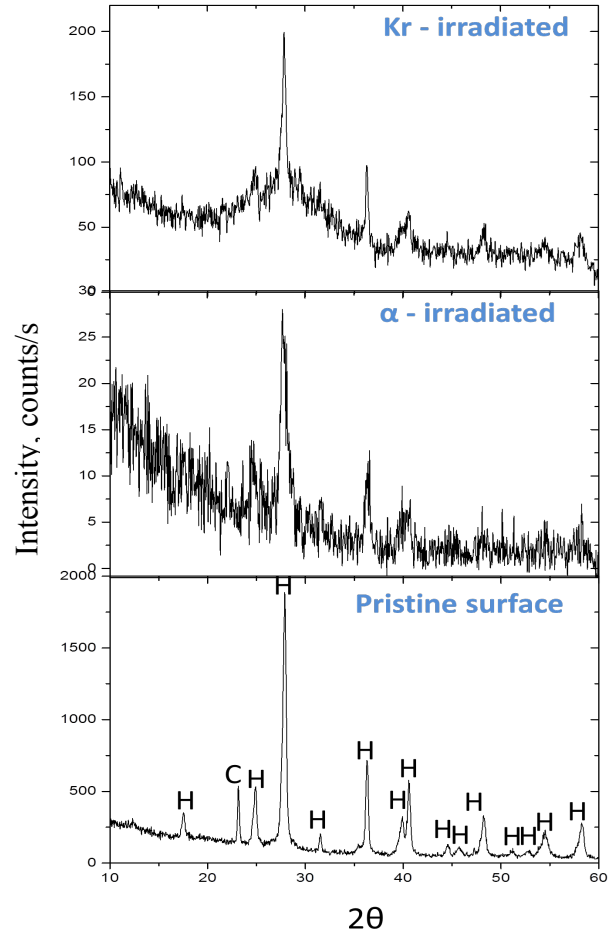
### **B.2.1. Irradiation-induced Changes**

Figure VII-4 compares the surface changes induced by He<sup>2+</sup> and Kr<sup>3+</sup> irradiation. Before the surface effects of irradiation are discussed, it has to be pointed out that the GIXRD of pristine surfaces of Cs-containing samples,  $x = 0.15$  and  $0.4$ , show the presence of secondary phases as indicated (Figure VII-4(b) and (c)). At higher Cs levels, Cs-rich secondary phase Cs<sub>2</sub>CrO<sub>4</sub> was observed (same as the one shown in Figure VII-1). However, these secondary phases were not observed in the corresponding powder XRD patterns but only in the extended GIXRD scans.

The GIXRD data from Figure VII-4 suggests that irrespective of the amount of Cs, α- and Kr-radiation induced similar changes on hollandite samples. He<sup>2+</sup>/α-radiation is known to produce ionizing effects that might result in the breakage of the bonds or the crystal structure.<sup>95,96</sup> GIXRD phase analysis of the α-irradiated surfaces shows evidence of these effects. Small peaks corresponding to the phases TiO<sub>2</sub> and BaTi<sub>2</sub>O<sub>5</sub> are seen along with noticeable amounts of amorphization. The drop in the relative intensity counts of crystalline peaks suggests amorphization. It is to be noted that GIXRD of α-irradiated surface for  $x = 0.4$  composition has significant noise in the data, and hence does not convey as much information as the rest of the compositions. The overall data suggests that the hollandite structure breaks down at a certain dosage of He<sup>2+</sup> irradiation forming secondary phases initially such as TiO<sub>2</sub> and BaTi<sub>2</sub>O<sub>5</sub>, which eventually loses crystallinity to form amorphous layer. In the case of Kr<sup>3+</sup>-radiation, by visual observation, higher amount of an amorphization occurred relative to that of α-radiation. Crystalline peaks observed in each of the samples correspond to the phases that were present in the pristine sample. As reported in several works<sup>95-97</sup>, heavy ion irradiations produce cascading effects and atomic displacements resulting in amorphization.

Comparing these effects as a function of the Cs content, it can be observed that addition of Cs into the hollandite lattice intensified the radiation effects. Examination of number of crystalline peaks or amount of crystallinity presented in Figure VII-4 (a), (b) and (c) suggests this. The drop in the total number of sharp reflections as well as the intensities of corresponding reflections with increasing Cs content is evidently seen from Figure VII-4. This trend hints at the relatively higher mobility of Cs ions in the structure. However, the exact mechanism of the observed phase transformations needs further in-depth investigation in the future. Additional work is necessary to determine the critical dosage of  $\text{He}^{2+}$  or  $\text{Kr}^{3+}$  to induce hollandite structure break down for each of the compositions.





(c)

Figure VII-4. GIXRD patterns showing the radiation-induced surface transformations on  $\text{Ba}_{1.15-x}\text{Cs}_{2x}\text{Cr}_{2.3}\text{Ti}_{5.7}\text{O}_{16}$  hollandites (a)  $x = 0$  (b)  $x = 0.15$  and (c)  $x = 0.4$ . Different  $2\theta$  peaks are labeled on pristine surface plots and the new phases appeared upon radiation are labeled in corresponding patterns: H – hollandite, T –  $\text{TiO}_2$ , B –  $\text{BaTi}_2\text{O}_5$  and C –  $\text{Cs}_2\text{CrO}_4$ .

## CONCLUSION

The overall work described in this thesis contributes to the development of ceramic waste forms from two perspectives – processing technology and fundamental science. The multiphase studies, as outlined in Sections III and IV, demonstrated the feasibility of melt-processing as a one-step process to incorporate all HLW elements into crystalline lattices of a multiphase ceramic system. The single-phase studies on hollandite systems, Sections V and VI, provide basic understanding of the structural chemistry of Cs-substituted hollandites. In addition, the effects of Cs content on the performance of selected phase-pure hollandites was analyzed qualitatively by chemical durability and radiation resistance testing. The major achievements from these studies can be summarized as follows:

### A. Processing of Multiphase Waste Forms

Simulated HLW compositions developed by SRNL were processed by melt-processing and SPS routes and characterized by multiple complimentary techniques such as XRD, SEM and TEM. Melt-processed samples had the desired phase and elemental distribution – hollandite phase with Ba, Cs, Cr, Ti and Fe, perovskite phase with Ca, Nd, Sr and Ti, pyrochlore/zirconolite phase with Ca, Zr and Ti as major elements, and TiO<sub>2</sub> phase. SPS processed samples, in addition to the desired phases, had minor amounts of unreacted phases such as CeO<sub>2</sub>. More importantly, Cs-rich phases were observed in the SPS processed samples indicating Cs did not partition into hollandite phase. The partitioning of Cs into the hollandite lattice during melt-processing was confirmed by WDS elemental maps and in addition, TEM-SAED analysis suggested a three-dimensional ordering of tunnel cations and vacancies in hollandite lattice. These results favour melt-processing over SPS for multiphase waste form processing.

In a typical melt-processing, the solidification of multiphase compositions occurs by fractional crystallization producing different phases at different stages. This knowledge can be used to modify temperature-time parameters of melt-processing cycle to obtain the intended phase assemblage based on the waste stream composition. The

melt-solidification process in our case was studied by in-situ XRD and heating/quenching methods. The combined data confirm the order of phase transformations during heating and crystallization events during cooling. Hollandite rich in Ba, Cr, Ti and Cs formed at  $\sim 900^\circ\text{C}$ , along with perovskite and Ca-Zr-Ti-O phases during the heating cycle. All crystalline phases except hollandite were dissolved on further heating to  $1500^\circ\text{C}$  indicating only partial melting of the system at  $1500^\circ\text{C}$ . On cooling, the remaining phases crystallized in the order – perovskite and Ca-Zr-Ti-O at  $\sim 1300^\circ\text{C}$  and rutile at  $\sim 1280^\circ\text{C}$ . Zirconolite evolution from the liquid was complex involving a series of intermediate products represented as Ca-Zr-Ti-O. Overall, this study provided valuable information on the sequence of phase evolution but also indicated that the selected temperature  $1500^\circ\text{C}$  was below the liquidus of the selected HLW composition. This, along with the rapid solidification kinetics of the system, pose a critical challenge while pouring the waste form into canisters. This problem can be addressed by (i) increasing the melting temperature which in turn enhances Cs volatilization or (ii) modifying the target hollandite chemical composition to reduce the melting point. However, such is beyond the scope of this study.

## **B. Structural Chemistry of $\text{Ba}_{1.15-x}\text{Cs}_{2x}\text{Cr}_{2.3}\text{Ti}_{5.7}\text{O}_{16}$ Hollandites**

The second half of this work focused on incorporation of Cs in a stable hollandite lattice and the evaluation of the induced structural effects. The choice of hollandite composition  $\text{Ba}_{1.15-x}\text{Cs}_{2x}\text{Cr}_{2.3}\text{Ti}_{5.7}\text{O}_{16}$  was made on the basis of two factors: (i) The findings from multiphase studies (Sections III and IV) clearly suggest that Cr containing hollandite forms during heating cycle during melt-processing and is the major hollandite phase (ii) A comparison of the phase evolution behavior of the selected compositions  $\text{Ba}_{1.0}\text{Cs}_{0.3}\text{M}^{3+}_{2.3}\text{Ti}_{5.7}\text{O}_{16}$  (M = Al, Fe, Cr) further support the low-temperature formation of Cr-hollandite.

Sol-gel synthesis and the subsequent phase analysis of series of hollandites  $\text{Ba}_{1.15-x}\text{Cs}_{2x}\text{Cr}_{2.3}\text{Ti}_{5.7}\text{O}_{16}$  ( $0 \leq x \leq 1.15$ ) determined the maximum solubility of Cs as  $x = 0.4$ . Powder XRD, NPD and TEM experiments were carried out on phase-pure compositions  $\text{Ba}_{1.15-x}\text{Cs}_{2x}\text{Cr}_{2.3}\text{Ti}_{5.7}\text{O}_{16}$  ( $x = 0, 0.15$  and  $0.25$ ) to have a comprehensive understanding of the structures. Rietveld refinement of XRD and NPD patterns confirm the monoclinic

(12/m) symmetry of all compositions. Two main criteria – octahedral framework variations and tunnel ion order/disorder – were compared and characterized from the structural models generated from refinements. Substitution of smaller Ba with larger Cs preferentially elongated Cr-O bonds at corner-sharing sites between oxygen octahedral which shows that Cs favors tunnel sites surrounded by  $\text{CrO}_6$  octahedra. Tunnel ions in all compositions had significantly high ADPs along tunnel direction ( $\beta_{22}$ ). In addition, SAED and powder XRD patterns confirm the ordering of tunnel cations along the  $b$ -axis resulting in ordered superstructures. Hence, the disorder denoted by  $\beta_{22}$  implies positional disorder of tunnel cations within a supercell. The refined structural models were consistent with several reported structures confirming that the phase-pure hollandites of  $\text{Ba}_{1.15-x}\text{Cs}_{2x}\text{Cr}_{2.3}\text{Ti}_{5.7}\text{O}_{16}$  system adapted monoclinic superstructure with ordered tunnel cations and vacancies.

### C. Performance Testing

The performance of the phase-pure hollandites evaluated by chemical durability and radiation resistance testing in this study have been intended to determine qualitatively the effects of Cs loading. Cs elemental release during PCT leach testing was found to be accompanied with Cr and the relative amount of Cs extracted out of the lattice reduced with increasing Cs composition. The trend in PCT data suggests that the release of Cs is inhibited by dense packing of tunnels. However, this theory can only be verified with a detailed understanding of the actual leaching mechanism.

The nature of irradiation-induced changes on the selected phase-pure hollandite compositions was studied by GIXRD.  $\text{He}^{2+}$  and  $\text{Kr}^{3+}$  ion-irradiation experiments, to  $\alpha$ -decay events, show that the hollandite surface amorphizes in either case. The data (Section VII.2) suggest that the ionizing  $\alpha$ -radiation breaks down and amorphizes the hollandite structure by forming intermediate crystalline phases such as  $\text{BaTi}_2\text{O}_5$  and  $\text{TiO}_2$ . Heavy ion-radiation ( $\text{Kr}^{3+}$ ) was observed to induce amorphization in all samples but no information on the interaction of lattice and radiation were obtained from this study. Further, based on the comparison of GIXRD of compositions with different Cs levels, it can be said qualitatively that the presence of Cs in the structure enhances the degree of damage (amorphization) in  $\text{Ba}_{1.15-x}\text{Cs}_{2x}\text{Cr}_{2.3}\text{Ti}_{5.7}\text{O}_{16}$  hollandites.

## **FUTURE WORK**

As evident from this thesis work on the multiphase waste forms, a complete understanding and the kinetics of elemental segregation in different phases remains unclear and is extremely challenging to pursue. It might therefore be advantageous to continue to study and develop a database on individual phases and the effects on elemental substitutions on them. Hence, the later part of this thesis was designed to contribute to the studies on hollandites for Cs incorporation. Structural models were developed accordingly for different levels of Cs. But our leach testing and analysis was limited. A detailed leach testing will reveal the underlying mechanism of Cs release in hollandites.

Advancing this work, in-situ experimental studies such as TEM observation of interfacial reaction between hollandite lattice and water may be necessary to understand the leaching process. Detailed quantum mechanical, molecular dynamics (MD), and phase field modeling and simulation experiments to study the crystal surface interaction with specific environment of interest to nuclear waste disposal will be valuable. Structural parameters from in situ XRD and in operando Raman can be particularly useful in these simulation studies. Combining simulation results with experimental observations can help evaluate and further validate the selected hollandite compositions as a waste form material. Such an approach can be extended to other phases of interest in waste forms such as perovskite, zirconolite and pyrochlore.

## REFERENCES

1. "Nuclear Power in the World Today". Accessed on 12/13/16: Available at <<http://www.world-nuclear.org/information-library/current-and-future-generation/nuclear-power-in-the-world-today.aspx>>
2. D. Caurant, P. Loiseau, O. Majerus, V. Aubin-Chevaldonnet, I. Bardez, and A. Quintas, *Glasses, Glass-Ceramics and Ceramics for Immobilization of Highly Radioactive Nuclear Wastes*. Nova Science Publishers New York, 2009.
3. V. Aubin-Chevaldonnet, D. Caurant, A. Dannoux, D. Gourier, T. Charpentier, L. Mazerolles, and T. Advocat, "Preparation and Characterization of (Ba,Cs)(M,Ti)<sub>8</sub>O<sub>16</sub> (M = Al<sup>3+</sup>, Fe<sup>3+</sup>, Ga<sup>3+</sup>, Cr<sup>3+</sup>, Sc<sup>3+</sup>, Mg<sup>2+</sup>) Hollandite Ceramics Developed for Radioactive Cesium Immobilization," *J. Nucl. Mater.*, **366** [1] 137-60 (2007).
4. S. V. Stefanovsky, S. V. Yudintsev, R. Gieré, and G. R. Lumpkin, "Nuclear Waste Forms," *Geological Society, London, Special Publications*, **236** [1] 37-63 (2004).
5. I. W. Donald, B. L. Metcalfe, and R. N. J. Taylor, "The Immobilization of High Level Radioactive Wastes Using Ceramics and Glasses," *J. Mater. Sci.*, **32** [22] 5851-87 (1997).
6. W. J. Weber, R. C. Ewing, C. A. Angell, G. W. Arnold, A. N. Cormack, J. M. Delaye, D. L. Griscom, L. W. Hobbs, A. Navrotsky, and D. L. Price, "Radiation Effects in Glasses Used for Immobilization of High-Level Waste and Plutonium Disposition," *J. Mater. Res.*, **12** [08] 1948-78 (1997).
7. B. Veal, J. Mundy, and D. Lam, "Actinides in Silicate Glasses", pp. 271-309 in *Handbook on the Physics and Chemistry of the Actinides. Vol. 5*. 1987.
8. G. J. McCarthy, W. B. White, R. Roy, B. E. Scheetz, S. Komarneni, D. K. Smith, and D. M. Roy, "Interactions between Nuclear Waste and Surrounding Rock," *Nature*, **273** [5659] 216-17 (1978).
9. M. S. Whittingham, "Inorganic phosphate materials", in *Materials Science Monographs # 52*. Edited by T. Kanazawa, Elsevier Science Publishers, Amsterdam, 1989.
10. W. Ramsey, N. Bibler, and T. Meaker, "Compositions and Durabilities of Glasses for Immobilization of Plutonium and Uranium," Westinghouse Savannah River Co., Aiken, SC, 1995.
11. E. R. Vance, S. Urquhart, D. Anderson, and I. George, "Immobilization of Uranium-Rich High-Level Nuclear Waste", pp. 249-258 in *Nuclear Waste Management II*. 1986.

12. L. Bunnell, G. Maupin, and K. Oma, "High-Temperature Glasses for Nuclear Waste Isolation," PNL-SA-13606, Pacific Northwest Laboratory, Richland, WA, 1986.
13. W. Gong, W. Lutze, A. Abdelouas, and R. Ewing, "Vitrification of Radioactive Waste by Reaction Sintering under Pressure," *J. Nucl. Mater.*, **265** [1] 12-21 (1999).
14. G. J. McCarthy, "Ceramics and Glass Ceramics as High Level Waste Forms", pp. 83-99 in *Ceramics and Glass Radioactive Waste Forms*, Edited by C. R. Cooley, and D.W.Readey, 1977.
15. G. J. McCarthy, "High-Level Waste Ceramics: Materials Considerations, Process Simulation, and Product Characterization," *Nucl. Technol.*, **32** [1] 92-105 (1977).
16. M. I. Ojovan and W. E. Lee, "New Immobilising Hosts and Technologies", pp. 251-67 in *An Introduction to Nuclear Waste Immobilisation*, Edited by M. I. Ojovan and W. E. Lee, Elsevier , 2005.
17. G. R. Lumpkin, "Ceramic Waste Forms for Actinides," *Elements*, **2** [6] 365-72 (2006).
18. A. E. Ringwood, S. E. Kesson, N. G. Ware, W. Hibberson, and A. Major, "Immobilisation of High Level Nuclear Reactor Wastes in Synroc," *Nature*, **278** [5701] 219-23 (1979).
19. A. Ringwood, S. Kesson, N. Ware, W. Hibberson, and A. Major, "The Synroc Process: A Geochemical Approach to Nuclear Waste Immobilization," *Geochem. J.*, **13** [4] 141-65 (1979).
20. W. Sinclair, G. McLaughlin, and A. Ringwood, "The Structure and Chemistry of a Barium Titanate Hollandite-Type Phase," *Acta Crystallogr. Sect. B: Struct. Sci.*, **36** [12] 2913-18 (1980).
21. D. C. V. Aubin, D. Gourier, N. Baffier, T. Advocat, F. Bart, G. Leturcg, J. M. Constantini "Synthesis, Characterisation and Study of the Radiation Effects on Hollandite Ceramics Developed for Caesium Immobilization," *Mat. Res. Soc. Symp. Proc.*, **807** 315-20 (2003).
22. R. W. Cheary and J. Kwiatkowska, "An X-Ray Structural Analysis of Cesium Substitution in the Barium Hollandite Phase of Synroc," *J. Nucl. Mater.*, **125** [2] 236-43 (1984).
23. M. Pena and J. Fierro, "Chemical Structures and Performance of Perovskite Oxides," *Chem. Rev.*, **101** [7] 1981-2018 (2001).
24. E. Vance, M. Carter, B. Begg, R. Day, and S. Leung, "Solid Solubilities of Pu, U, Hf and Gd in Candidate Ceramic Phases for Actinide Waste Immobilization," *MRS Symp. Proc.*, **608** [6] (1999).

25. A. Ringwood, S. Kesson, K. Reeve, D. Levins, and E. Ramm, "Synroc", pp. 233-334 in *Radioactive Waste Forms for the Future*, Edited by W. Lutze and RC Ewing, 1988.
26. K. L. Smith, N. J. Zaluzec, and G. R. Lumpkin, "The Relative Radiation Resistance of Zirconolite, Pyrochlore, and Perovskite to 1.5 MeV Kr<sup>+</sup> Ions," *MRS Symp. Proc.*, **506** [2] (1997).
27. J. Sloan and R. Tilley, "Phase Formation in the Nd<sub>2</sub>Ti<sub>2</sub>O<sub>7</sub>– SrTiO<sub>3</sub> System at 1350°C in the Presence of V<sub>2</sub>O<sub>5</sub>, CuV<sub>2</sub>O<sub>6</sub> or SrCuO<sub>2</sub>," *J. Solid State Chem.*, **121** [2] 324-31 (1996).
28. K. Sickafus, L. Minervini, R. Grimes, J. Valdez, M. Ishimaru, F. Li, K. McClellan, and T. Hartmann, "Radiation Tolerance of Complex Oxides," *Science*, **289** [5480] 748-51 (2000).
29. J. Lian, S. Yudinsev, S. Stefanovsky, L. Wang, and R. Ewing, "Ion Beam Irradiation of U-, Th- and Ce-Doped Pyrochlores," *J. Alloys Compd.*, **444** 429-33 (2007).
30. B. Mandal and A. Tyagi, "Pyrochlores: Potential Multifunctional Materials," *Barc Newslett.*, **313** 6 (2010).
31. H. Rossell, "Solid Solution of Metal Oxides in the Zirconolite Phase CaZrTi<sub>2</sub>O<sub>7</sub>. II: The Ternary Phase CaZr<sub>x</sub>Ti<sub>3-x</sub>O<sub>7</sub>," *J. Solid State Chem.*, **99** [1] 52-57 (1992).
32. A. Coelho, R. Cheary, and K. Smith, "Analysis and Structural Determination of Nd-Substituted Zirconolite-4M," *J. Solid State Chem.*, **129** [2] 346-59 (1997).
33. W. Gong, W. Lutze, and R. Ewing, "Zirconia Ceramics for Excess Weapons Plutonium Waste," *J. Nucl. Mater.*, **277** [2] 239-49 (2000).
34. S. Kessoft, W. Sinclair, and A. Ringwood, "Solid Solution Limits in Synroc Zirconolite," *Nucl. Chem. Waste Manage.*, **4** [3] 259-65 (1983).
35. E. Vance, C. Ball, R. Day, K. Smith, M. Blackford, B. Begg, and P. Angel, "Actinide and Rare Earth Incorporation into Zirconolite," *J. Alloys Compd.*, **213** 406-09 (1994).
36. S. Roberts, W. Bourcier, and H. Shaw, "Aqueous Dissolution Kinetics of Pyrochlore, Zirconolite and Brannerite at 25, 50, and 75°C," *Radiochim. Acta*, **88** [9-11] 539 (2000).
37. R. C. Ewing, W. J. Weber, and J. Lian, "Nuclear Waste Disposal - Pyrochlore (A<sub>2</sub>B<sub>2</sub>O<sub>7</sub>): Nuclear Waste Form for the Immobilization of Plutonium and "Minor" Actinides," *J. Appl. Phys.*, **95** [11] 5949-71 (2004).
38. D. M. Strachan, R. D. Scheele, E. C. Buck, A. E. Kozelisky, R. L. Sell, R. J. Elovich, and W. C. Buchmiller, "Radiation Damage Effects in Candidate Titanates for Pu Disposition: Zirconolite," *J. Nucl. Mater.*, **372** [1] 16-31 (2008).

39. F. Clinard Jr, E. Foltyn, and R. Ewing, "Stored Energy in Natural Zirconolite and Its Synthetic Counterpart after Alpha Recoil Self-Irradiation Damage," *J. Nucl. Mater.*, **185** [2] 202-07 (1991).
40. F. Clinard Jr, D. Rohr, and R. Roof, "Structural Damage in a Self-Irradiated Zirconolite-Based Ceramic," *Nucl. Instrum. Methods Phys. Res., Sect. B*, **1** [2] 581-86 (1984).
41. A. Byström and A. M. Byström, "The Crystal Structure of Hollandite, the Related Manganese Oxide Minerals, and  $\alpha$ -MnO<sub>2</sub>," *Acta Crystallogr.*, **3** [2] 146-54 (1950).
42. B. Das, M. Reddy, G. S. Rao, and B. Chowdari, "Nano-Phase Tin Hollandites, K<sub>2</sub>(M<sub>2</sub>Sn<sub>6</sub>)O<sub>16</sub> (M = Co, in) as Anodes for Li-Ion Batteries," *J. Mater. Chem.*, **21** [4] 1171-80 (2011).
43. N. Sharma, J. Plevart, G. Subba Rao, B. Chowdari, and T. White, "Tin Oxides with Hollandite Structure as Anodes for Lithium Ion Batteries," *Chem. Mater.*, **17** [18] 4700-10 (2005).
44. S. Liu, A. R. Akbashev, X. Yang, X. Liu, W. Li, L. Zhao, X. Li, A. Couzis, M.-G. Han, and Y. Zhu, "Hollandites as a New Class of Multiferroics," *Sci. Rep.*, **4** (2014).
45. A. M. Larson, P. Moetakef, K. Gaskell, C. M. Brown, G. King, and E. E. Rodriguez, "Inducing Ferrimagnetism in Insulating Hollandite Ba<sub>1.2</sub>Mn<sub>8</sub>O<sub>16</sub>," *Chem. Mater.*, **27** [2] 515-25 (2015).
46. R. C. Ewing, "The Design and Evaluation of Nuclear-Waste Forms: Clues from Mineralogy," *Can. Mineral.*, **39** [3] 697-715 (2001).
47. J. E. Post, R. Von Dreele, and P. Buseck, "Symmetry and Cation Displacements in Hollandites: Structure Refinements of Hollandite, Cryptomelane and Priderite," *Acta Crystallogr. Sect. B: Struct. Sci.*, **38** [4] 1056-65 (1982).
48. R. Cheary, "A Structural Analysis of Potassium, Rubidium and Caesium Substitution in Barium Hollandite," *Acta Crystallogr. Sect. B: Struct. Sci.*, **43** [1] 28-34 (1987).
49. R. W. Cheary, "An Analysis of the Structural Characteristics of Hollandite Compounds," *Acta Crystallogr. Sect. B: Struct. Sci.*, **42** [3] 229-36 (1986).
50. J. Amoroso, J. Marra, S. D. Conradson, M. Tang, and K. Brinkman, "Melt Processed Single Phase Hollandite Waste Forms for Nuclear Waste Immobilization: Ba<sub>1.0</sub> Cs<sub>0.3</sub> A<sub>2.3</sub>Ti<sub>5.7</sub>O<sub>16</sub>; A = Cr, Fe, Al," *J. Alloys Compd.*, **584** 590-99 (2014).
51. S. E. Kesson and T. J. White, "[Ba<sub>x</sub>Cs<sub>y</sub>][(Ti,Al)<sup>3+</sup><sub>2x+y</sub>Ti<sup>4+</sup><sub>8-2x-y</sub>]O<sub>16</sub> Synroc-Type Hollandites. I. Phase Chemistry," *Proc. R. Soc. London, Ser. A*, **405** [1828] 73-101 (1986).

52. S. E. Kesson and T. J. White, "[Ba<sub>x</sub>Cs<sub>y</sub>][(Ti,Al)<sup>3+</sup><sub>2x+y</sub>Ti<sup>4+</sup><sub>8-2x-y</sub>]O<sub>16</sub> Synroc-Type Hollandites II. Structural Chemistry," *Proc. R. Soc. London, Ser. A*, **408** [1835] 295-319 (1986).
53. R. W. Cheary, "The Immobilisation of Cesium in Synroc," *Mater. Sci. Forum*, **27** 397-406 (1988).
54. M. L. Carter and R. L. Withers, "A Universally Applicable Composite Modulated Structure Approach to Ordered Ba<sub>x</sub>M<sub>y</sub>Ti<sub>8-y</sub>O<sub>16</sub> Hollandite-Type Solid Solutions," *J. Solid State Chem.*, **178** [6] 1903-14 (2005).
55. L. Bursill and G. Grzanic, "Incommensurate Superlattice Ordering in the Hollandites Ba<sub>x</sub>Ti<sub>8-x</sub>Mg<sub>x</sub>O<sub>16</sub> and Ba<sub>x</sub>Ti<sub>8-2x</sub>Ga<sub>2x</sub>O<sub>16</sub>," *Acta Crystallogr. Sect. B: Struct. Sci.*, **36** [12] 2902-13 (1980).
56. Y. Xu, Y. Wen, R. Grote, J. Amoroso, L. S. Nickles, and K. S. Brinkman, "A-Site Compositional Effects in Ga-Doped Hollandite Materials of the Form Ba<sub>x</sub>Cs<sub>y</sub>Ga<sub>2x+y</sub>Ti<sub>8-2x-y</sub>O<sub>16</sub> : Implications for Cs Immobilization in Crystalline Ceramic Waste Forms," *Sci. Rep.*, **6** 27412 (2016).
57. H. Xu, L. Wu, J. Zhu, and A. Navrotsky, "Synthesis, Characterization and Thermochemistry of Cs-, Rb- and Sr-Substituted Barium Aluminium Titanate Hollandites," *J. Nucl. Mater.*, **459** 70-76 (2015).
58. H. Xu, G. C. Costa, C. R. Stanek, and A. Navrotsky, "Structural Behavior of Ba<sub>1.24</sub>Al<sub>2.48</sub>Ti<sub>5.52</sub>O<sub>16</sub> Hollandite at High Temperature: An in Situ Neutron Diffraction Study," *J. Am. Ceram. Soc.*, **98** [1] 255-62 (2015).
59. P. Tumorugoti, S. Sundaram, K. Brinkman, J. Amoroso, and K. Fox, "Melt-Processed Multiphasic Ceramic Waste Forms," *Ceram. Trans.*, **250** 205-12 (2014).
60. P. Tumorugoti, S. Sundaram, S. T. Misture, J. C. Marra, and J. Amoroso, "Crystallization Behavior During Melt-Processing of Ceramic Waste Forms," *J. Nucl. Mater.*, **473** 178-88 (2016).
61. P. Tumorugoti, B. Clark, D. Edwards, J. Amoroso, and S. Sundaram, "Cesium Incorporation in Hollandite-Rich Multiphasic Ceramic Waste Forms," *J. Solid State Chem.*, **246** 107-112 (2016).
62. "Standard Test Methods for Determining Chemical Durability of Nuclear, Hazardous, and Mixed Waste Glasses and Multiphase Glass Ceramics: The Product Consistency Test (PCT)," ASTM Standard C1285-02, ASTM International, West Conshohocken, PA, 2002.

63. J. Amoroso, J. C. Marra, M. Tang, Y. Lin, F. Chen, D. Su, and K. S. Brinkman, "Melt Processed Multiphase Ceramic Waste Forms for Nuclear Waste Immobilization," *J. Nucl. Mater.*, **454** [1] 12-21 (2014).
64. H. Zandbergen, P. Everstijn, F. Mijlhoff, G. Renes, and D. Ijdo, "Composition, Constitution and Stability of the Synthetic Hollandites  $A_xM_{4-2x}N_{2x}O_8$ , M = Ti, Ge, Ru, Zr, Sn and N = Al, Sc, Cr, Ga, Ru, in and the System  $(A,Ba)_xTi_yAl_zO_8$  with a = Rb, Cs, Sr," *Mater. Res. Bull.*, **22** [4] 431-38 (1987).
65. F. Mijlhoff, D. Ijdo, and H. Zandbergen, "Constitution and Structure of Synthetic Hollandites, an Electron and X-Ray Diffraction Study," *Acta Crystallogr. Sect. B: Struct. Sci.*, **41** [2] 98-101 (1985).
66. M. Carter, "Tetragonal to Monoclinic Phase Transformation at Room Temperature in  $Ba_xFe_{2x}Ti_{8-2x}O_{16}$  Hollandite Due to Increased Ba Occupancy," *Mater. Res. Bull.*, **39** [7] 1075-81 (2004).
67. B. Clark, P. Tumurugoti, S. Sundaram, J. Amoroso, J. Marra, and K. Brinkman, "Microstructures of Melt-Processed and Spark Plasma Sintered Ceramic Waste Forms," *Metall. Mater. Trans. E*, **1** [4] 341-48 (2014).
68. M. De Graef, *Introduction to Conventional Transmission Electron Microscopy*. Cambridge University Press, 2003.
69. J. Van Landuyt, G. Van Tendeloo, and S. Amelinckx, "Electron Microscopy and Diffraction of Modulated Structures," *Pure Appl. Chem.*, **57** [10] 1373-82 (1985).
70. L. Bursill and J. Kwiatkowska, "Location of Cs Ions in a Hollandite-Related Superstructure," *J. Solid State Chem.*, **52** [1] 45-52 (1984).
71. E. Fanchon, J. Hodeau, J. Vicat, and J. Watts, "Three-Dimensional/One-Dimensional Transition in the  $Cs^+$  Sublattice of the Mixed Valence  $CsTi_8O_{16}$  Hollandite: Structures at 297 and 673 K," *J. Solid State Chem.*, **92** [1] 88-100 (1991).
72. U. Kolb, K. Shankland, L. Meshi, A. Avilov, and W. I. David, *Uniting Electron Crystallography and Powder Diffraction*. Springer, 2012.
73. A. Leinekugel-le-Cocq-Errien, P. Deniard, S. Jobic, E. Gautier, M. Evain, V. Aubin, and F. Bart, "Structural Characterization of the Hollandite Host Lattice for the Confinement of Radioactive Cesium: Quantification of the Amorphous Phase Taking into Account the Incommensurate Modulated Character of the Crystallized Part," *J. Solid State Chem.*, **180** [1] 322-30 (2007).
74. K.M. Fox, ITS-0058, SRNL L29 Manual, Savannah River National Laboratory, Aiken, SC, 2010.

75. R. F. Schumacher, R. J. Workman, T. B. Edwards, "Establishment of Harrop, High-Temperature Viscometer," WSRC-RP-98-00737, Savannah River National Laboratory, Aiken, SC, 1998.
76. J. E. Shelby, *Introduction to Glass Science and Technology*. Royal Society of Chemistry, 2005.
77. A.A. Kashaev, Z.F. Ushchapovskaia, "Tazheranite – a Mineral with  $\text{CaF}_2$  – Type Structure " *Sov. Phys. Cryst.*, **14** 1064 - 65 (1969).
78. M. Yoshimura, "Phase Stability of Zirconia," *Am. Ceram. Soc. Bull.*, **67** [12] (1988).
79. P. Li, I. W. Chen, and J. E. Penner-Hahn, "Effect of Dopants on Zirconia Stabilization - an X-Ray Absorption Study: III, Charge-Compensating Dopants," *J. Am. Ceram. Soc.*, **77** [5] 1289-95 (1994).
80. P. Li, I. W. Chen, and J. E. Penner-Hahn, "Effect of Dopants on Zirconia Stabilization - an X-Ray Absorption Study: I, Trivalent Dopants," *J. Am. Ceram. Soc.*, **77** [1] 118-28 (1994).
81. D. Swenson, T.-G. Nieh, and J. H. Fournelle, "Solid-State Phase Relationships in the Calcia-Titania-Zirconia System at 1200°C," *J. Am. Ceram. Soc.*, **81** [12] 3249-52 (1998).
82. H. Xu and Y. Wang, "Crystallization Sequence and Microstructure Evolution of Synroc Samples Crystallized from  $\text{CaZrTi}_2\text{O}_7$  Melts," *J. Nucl. Mater.*, **279** [1] 100-06 (2000).
83. R. W. Cheary, "Caesium Substitution in the Titanate Hollandites  $\text{Ba}_x\text{Cs}_y(\text{Ti}^{3+}_{y+2x}\text{Ti}^{4+}_{8-2x-y})\text{O}_{16}$  from 5 to 400 K," *Acta Crystallogr. Sect. B: Struct. Sci.*, **47** [3] 325-33 (1991).
84. E. Fanchon, J. Vicat, J.-L. Hodeau, P. Wolfers, D. Tran Qui, and P. Strobel, "Commensurate Ordering and Domains in the  $\text{Ba}_{1.2}\text{Ti}_{6.8}\text{Mg}_{1.2}\text{O}_{16}$  Hollandite," *Acta Crystallogr. Sect. B: Struct. Sci.*, **43** [5] 440-48 (1987).
85. V. Aubin-Chevaldonnet, P. Deniard, M. Evain, A. Y. Leinekugel-Le-Cocq-Errien, S. Jobic, D. Caurant, V. Petricek, and T. Advocat, "Incommensurate Modulations in a Hollandite Phase  $\text{Ba}_x(\text{Al,Fe})_{2x}\text{Ti}_{8-2x}\text{O}_{16}$  Intended for the Storage of Radioactive Wastes: A (3+1)-Dimension Structure Determination," *Z. Kristallogr.*, **222** [8] 383-90 (2007).
86. K. Harvey and C. Jensen, "An Intercomparison of Leach-Testing Methods and the Effects of Waste-Form Composition on Test Type and Duration," *Nucl. Chem. Waste Manage.*, **3** [1] 43-50 (1982).
87. D. Strachan, R. Turcotte, and B. Barnes, "MCC-1: A Standard Leach Test for Nuclear Waste Forms," *Nucl. Technol.*, **56** [2] 306-09 (1982).

88. "Standard Test Methods for Determining Chemical Durability of Nuclear, Hazardous, and Mixed Waste Glasses and Multiphase Glass Ceramics: The Product Consistency Test (PCT)", ASTM Standard C1285-14, ASTM International, West Conshohocken, PA, 2014.
89. "Standard Test Method for Measuring Waste Glass or Glass Ceramic Durability by Vapor Hydration Test", ASTM Standard C1663-09, ASTM International, West Conshohocken, PA, 2009.
90. M. L. Carter, A. L. Gillen, K. Olufson, and E. R. Vance, "Hiper Tailored Hollandite Waste Forms for the Immobilization of Radioactive Cs and Sr," *J. Am. Ceram. Soc.*, **92** [5] 1112-17 (2009).
91. D. Pham, S. Myhra, and P. Turner, "The Surface Reactivity of Hollandite in Aqueous Solution," *J. Mater. Res.*, **9** [12] 3174-82 (1994).
92. F. Angeli, P. McGlenn, and P. Frugier, "Chemical Durability of Hollandite Ceramic for Conditioning Cesium," *J. Nucl. Mater.*, **380** [1] 59-69 (2008).
93. V. Luca, D. Cassidy, E. Drabarek, K. Murray, and B. Moubaraki, "Cesium Extraction from  $\text{Cs}_{0.8}\text{Ba}_{0.4}\text{Ti}_8\text{O}_{16}$  Hollandite Nuclear Waste Form Ceramics in Nitric Acid Solutions," *J. Mater. Res.*, **20** [06] 1436-46 (2005).
94. W. J. Weber, R. C. Ewing, C. Catlow, T. D. d. I. Rubia, L. Hobbs, C. Kinoshita, H. Matzke, A. Motta, M. Nastasi, and E. Salje, "Radiation Effects in Crystalline Ceramics for the Immobilization of High-Level Nuclear Waste and Plutonium," *J. Mater. Res.*, **13** [6] 1434-84 (1998).
95. R. Ewing, W. Weber, and F. Clinard, "Radiation Effects in Nuclear Waste Forms for High-Level Radioactive Waste," *Prog. Nucl. Energ.*, **29** [2] 63-127 (1995).
96. W. Weber, "Effects of Alpha Irradiation on Barium Hollandite and Nickel-Iron Spinel," *MRS Symp. Proc.*, **44** 9 (1984).
97. M. Tang, P. Tumurugoti, B. Clark, S. Sundaram, J. Amoroso, J. Marra, C. Sun, P. Lu, Y. Wang, and Y.-B. Jiang, "Heavy Ion Irradiations on Synthetic Hollandite-Type Materials:  $\text{Ba}_{1.0}\text{Cs}_{0.3}\text{A}_{2.3}\text{Ti}_{5.7}\text{O}_{16}$  (A = Cr, Fe, Al)," *J. Solid State Chem.*, **239** 58-63 (2016).

## APPENDIX

### A. Structural Parameters of Phase-pure Hollandites $\text{Ba}_{1.15-x}\text{Cs}_{2x}\text{Cr}_{2.3}\text{Ti}_{5.7}\text{O}_{16}$

The Crystallographic Information Files (CIFs) of phase-pure compositions  $\text{Ba}_{1.15-x}\text{Cs}_{2x}\text{Cr}_{2.3}\text{Ti}_{5.7}\text{O}_{16}$  ( $x = 0, 0.15$  and  $0.25$ ) generated from Rietveld refinement of XRD and NPD data are listed below.

#### A.1. Structure file for $\text{Ba}_{1.15}\text{Cr}_{2.3}\text{Ti}_{5.7}\text{O}_{16}$

```
_cell_length_a      10.0847(3)
_cell_length_b      2.9590(1)
_cell_length_c      10.0746(3)
_cell_angle_alpha   90.0000(0)
_cell_angle_beta    90.0321(16)
_cell_angle_gamma   90.0000(0)

_symmetry_space_group_name_H-M  'I 2/m'
_symmetry_Int_Tables_number     12
_symmetry_cell_setting          monoclinic
loop_
_symmetry_equiv_pos_as_xyz
'1/2+x,1/2+y,1/2+z'
'1/2-x,1/2+y,1/2-z'
'1/2-x,1/2-y,1/2-z'
'1/2+x,1/2-y,1/2+z'

loop_
_atom_site_label
_atom_site_type_symbol
_atom_site_occupancy
```

```

_atom_site_fract_x
_atom_site_fract_y
_atom_site_fract_z
_atom_site_U_iso_or_equiv
Ba1 Ba 0.5630 0.0000 0.0000 0.0000
Fe3 Cr 0.2450 0.3302 0.0000 0.1348 0.1050
Fe5 Cr 0.3050 0.8365 0.0000 0.3353 0.0560
O1 O 1.0000 0.6625 0.0000 0.0410 0.0787
O4 O 1.0000 0.0421 0.0000 0.3312 0.0818
O6 O 1.0000 0.6533 0.0000 0.2995 0.0789
O9 O 1.0000 0.2988 0.0000 0.3462 0.0751
Ti2 Ti 0.7550 0.3291 0.0000 0.1405 0.1050
Ti8 Ti 0.6950 0.8440 0.0000 0.3377 0.0560

```

loop\_

```

_atom_site_aniso_label
_atom_site_aniso_U_11
_atom_site_aniso_U_22
_atom_site_aniso_U_33
_atom_site_aniso_U_23
_atom_site_aniso_U_13
_atom_site_aniso_U_12
Ba1 0.0179 0.1600 0.0100 0.0000 -0.0110 0.0000
Fe3 .....
Fe5 .....
O1 .....
O4 .....
O6 .....
O9 .....
Ti2 .....
Ti8 .....

```

## A.2. Structure file for $\text{Ba}_{1.0}\text{Cs}_{0.3}\text{Cr}_{2.3}\text{Ti}_{5.7}\text{O}_{16}$

\_cell\_length\_a            10.0244(6)  
\_cell\_length\_b            2.9333(2)  
\_cell\_length\_c            10.0076(6)  
\_cell\_angle\_alpha        90.0000(0)  
\_cell\_angle\_beta         90.0581(19)  
\_cell\_angle\_gamma        90.0000(0)

loop\_

\_symmetry\_equiv\_pos\_as\_xyz

'+x,+y,+z'

'+x,-y,+z'

'-x,+y,-z'

'-x,-y,-z'

'1/2+x,1/2+y,1/2+z'

'1/2+x,1/2-y,1/2+z'

'1/2-x,1/2+y,1/2-z'

'1/2-x,1/2-y,1/2-z'

loop\_

\_atom\_site\_label

\_atom\_site\_type\_symbol

\_atom\_site\_occupancy

\_atom\_site\_fract\_x

\_atom\_site\_fract\_y

\_atom\_site\_fract\_z

\_atom\_site\_U\_iso\_or\_equiv

Ba1 Ba 0.5000 0.0000 0.0000 0.0000 .

Ba1 Cs 0.1500 0.0000 0.0000 0.0000 .

Fe3	Cr	0.2630	0.3359	0.0000	0.1374	0.0717
Fe5	Cr	0.2700	0.8302	0.0000	0.3344	0.0590
O1	O	1.0000	0.6631	0.0000	0.0407	0.0768
O4	O	1.0000	0.0416	0.0000	0.3317	0.0795
O6	O	1.0000	0.6539	0.0000	0.2988	0.0724
O9	O	1.0000	0.2974	0.0000	0.3460	0.0750
Ti2	Ti	0.7370	0.3316	0.0000	0.1416	0.0717
Ti8	Ti	0.7300	0.8405	0.0000	0.3369	0.0590

loop\_

\_atom\_site\_aniso\_label

\_atom\_site\_aniso\_U\_11

\_atom\_site\_aniso\_U\_22

\_atom\_site\_aniso\_U\_33

\_atom\_site\_aniso\_U\_23

\_atom\_site\_aniso\_U\_13

\_atom\_site\_aniso\_U\_12

Ba1	0.0180	0.1725	0.0410	0.0000	-0.0284	0.0000
-----	--------	--------	--------	--------	---------	--------

Fe3 .....

Fe5 .....

O1 .....

O4 .....

O6 .....

O9 .....

Ti2 .....

Ti8 .....

### A.3. Structure file for $\text{Ba}_{0.9}\text{Cs}_{0.5}\text{Cr}_{2.3}\text{Ti}_{5.7}\text{O}_{16}$

\_cell\_length\_a            10.1917(13)

\_cell\_length\_b            2.9776(4)

\_cell\_length\_c            10.1590(13)

\_cell\_angle\_alpha        90.0000(0)  
 \_cell\_angle\_beta        90.1261(26)  
 \_cell\_angle\_gamma       90.0000(0)

loop\_

\_symmetry\_equiv\_pos\_as\_xyz

'+x,+y,+z'

'+x,-y,+z'

'-x,+y,-z'

'-x,-y,-z'

'1/2+x,1/2+y,1/2+z'

'1/2+x,1/2-y,1/2+z'

'1/2-x,1/2+y,1/2-z'

'1/2-x,1/2-y,1/2-z'

loop\_

\_atom\_site\_label

\_atom\_site\_type\_symbol

\_atom\_site\_occupancy

\_atom\_site\_fract\_x

\_atom\_site\_fract\_y

\_atom\_site\_fract\_z

\_atom\_site\_U\_iso\_or\_equiv

Ba	Ba	0.4500	0.0000	0.0000	0.0000	.
Cs	Cs	0.2500	0.0000	0.0000	0.0000	.
Cr1	Cr	0.2860	0.3320	0.0000	0.1480	0.0950
Cr2	Cr	0.2490	0.8264	0.0000	0.3293	0.0637
O1	O	1.0000	0.6637	0.0000	0.0399	0.0824
O2	O	1.0000	0.0416	0.0000	0.3325	0.0789
O3	O	1.0000	0.6548	0.0000	0.2981	0.0708

O4	O	1.0000	0.2967	0.0000	0.3468	0.0878
Ti1	Ti	0.7140	0.3320	0.0000	0.1470	0.0950
Ti2	Ti	0.7510	0.8412	0.0000	0.3329	0.0637

loop\_

\_atom\_site\_aniso\_label

\_atom\_site\_aniso\_U\_11

\_atom\_site\_aniso\_U\_22

\_atom\_site\_aniso\_U\_33

\_atom\_site\_aniso\_U\_23

\_atom\_site\_aniso\_U\_13

\_atom\_site\_aniso\_U\_12

Ba1	0.0791	0.1680	0.0370	0.0000	0.0527	0.0000
-----	--------	--------	--------	--------	--------	--------

Fe3 .....

Fe5 .....

O1 .....

O4 .....

O6 .....

O9 .....

Ti2 .....

Ti8 .....